



Stabilization of Ferroelectricity in Hafnia, Zirconia and their Mixtures by Dopants and Interface Energy: First Principles Calculations and a Phenomenological Model

zur Erlangung des akademischen Grades

Doktoringenieur

(Dr.-Ing.)

genehmigte Dissertation

Robin Materlik

Born on: 31st October 1987 in Augsburg

Chairman:	Prof. Dr. Stefan Mannsfeld	Technische Universität Dresden
Supervisor:	Prof. Dr. Thomas Mikolajick	Technische Universität Dresden
Supervisor:	Prof. Dr. Alfred Kersch	Hochschule München
4th Member:	Prof. Dr. Johann W. Bartha	Technische Universität Dresden

Submitted on: 18th January 2019

Defended on: 9th July 2019

Erklärung der Urheberschaft

Ich erkläre hiermit an Eides statt, dass ich die vorliegende Arbeit ohne Hilfe Dritter und ohne Benutzung anderer als der angegebenen Hilfsmittel angefertigt habe; die aus fremden Quellen direkt oder indirekt übernommenen Gedanken sind als solche kenntlich gemacht. Die Arbeit wurde bisher in gleicher oder ähnlicher Form in keiner anderen Prüfungsbehörde vorgelegt und auch noch nicht veröffentlicht.

Ort, Datum

Unterschrift

Abstract

Die überraschende Entdeckung von ferroelektrischem Hafniumoxid durch Böske et al. im Jahre 2011 eröffnet zahlreich technologische Möglichkeiten wie zum Beispiel voll CMOS kompatible ferroelektrische RAM Speicherzellen. Als kristallographische Ursache für dieses Verhalten erwies sich die Raumgruppe $Pca2_1$. In theoretischen Untersuchungen mit Hilfe der Dichtefunktionaltheorie erwies sich diese Phase jedoch als thermodynamisch instabil. Ziel dieser Dissertation ist daher zu klären, wie diese Phase stabilisiert werden kann. Dazu werden Faktoren wie Stöchiometrie, Temperatur, Druck, Spannung, Grenzflächenenergie sowie Defekte und Dotierung mit Hilfe der Dichtefunktionaltheorie untersucht. Die errechneten Ergebnisse werden mit Hilfe von Modellen interpretiert, welche im Laufe dieser Dissertation erarbeitet werden. Es zeigt sich, dass neben dem energetischen Zustand auch der Herstellungsprozess des Materials eine bedeutende Rolle in der Stabilisierung der ferroelektrischen Phase von Hafniumoxid spielt. Abschließend wird versucht Verbindung zum Experiment herzustellen, in dem experimentell zugängliche Stellschrauben aufgezeigt werden, welche die ferroelektrischen Eigenschaften von Hafniumoxid verbessern können und sich aus den erarbeiteten Ergebnissen ableiten.

Abstract

The surprising discovery of ferroelectric hafnium oxide by Böske et al. in 2011 enables various technological possibilities like CMOS compatible ferroelectric RAM devices. The space group $Pca2_1$ was identified as the crystallographic cause of this behavior. However, this phase was proved to be thermodynamically unstable by several theoretical studies using density functional theory. Therefore, the goal of this dissertation is to investigate physical effects contributing to the stabilization of the ferroelectric phase by means of density functional theory. These effects include stoichiometry, temperature, stress, strain, interface energy, as well as defects and dopants. The computational results will be interpreted with models, which will be developed within this dissertation. It will become apparent, that in addition to the energetic state, the production process of a sample plays an important role in the stabilization of the ferroelectric phase of hafnium oxide. In the conclusion, this work will attempt to find a connection to the experiment, by identifying experimentally accessible parameters within the computational results which can be used to optimize the ferroelectric properties of ferroelectric materials.

Acknowledgments

My gratitude goes to **Thomas Mikolajick**, my doctoral advisor at the technical university Dresden, for offering this opportunity and supervising my doctorate studies. His willingness to accept me as one of his external doctorate students despite the large distance between Munich and Dresden is not to be taken for granted and greatly appreciated.

I would like to thank the entire staff of the Department of Applied Sciences and Mechatronics at the Munich University of Applied Sciences. During my time at the department, there was always somebody willing to help, discuss, or advise, whenever I ran into troubles and I am proud to call them my friends and colleagues.

I would like to particularly thank **Alfred Kersch** for his supervision and the opportunity to work on this fascinating topic. In his role as the head of MoSiLab (Labor für Modelbildung und Simulation) he always took great interest in my research and contributed greatly with his advice, insights, and suggestions. He also knew how to push when needed, yet maintain a friendly and cordial work environment.

I would also like to cordially thank my colleagues at MoSiLab, particularly:

- **Christopher Künneth** for the countless and sometimes even quite heated but friendly debates we had together. Because we often approached a topic from different points of view, these discussions were always very productive and illuminating, and contributed greatly to my understanding of any given topic. He was also in charge of maintaining the software infrastructure, and was of immeasurable help whenever some software related troubles arose or something did not work as intended.
- **Max Falkowski**, who likewise was an excellent discussion partner willing to share his knowledge and insights. He also was always willing to offer a helping hand when needed.
- **Mustafa Yusufi** and **Andreas Dörfler**, while working at unrelated topics, they were always happy to provide an outsider's perspective or to have a friendly chat.

Furthermore, I would like to thank my colleagues **Christina Schindler**, **Michael Kaiser**, and **Bernhard Huber** from the microsystems technology laboratory for letting me work in their clean room and the use of their measurement equipment. I thoroughly enjoyed the opportunity to gain some practical experience, since my own work at MoSiLab was mostly theoretical in nature. Likewise I want to thank **Hans Christian Alt** and **Hans Edwin Wagner** from the solid state physics laboratory for training me in the use of infrared spectroscopy.

Naturally I want to thank our collaborators at RWTH Aachen, particularly **Ulrich Böttger**, **Sergej Starschich**, and **Fenja Berg** and at NaMLab in Dresden, particularly **Uwe Schroeder**, **Tony Schenk** and **Min Hyuk Park**, as well as **Stefan Müller**, **Claudia Richter**, **Michael Hoffmann**, **Milan Pešić**, and **Stefan Schmult**. Our frequent discussions, exchanges, and meetings deeply informed my understanding of the topic of ferroelectrics and inspired me to explore new avenues in my research.

The German research foundation (Deutsche Forschungsgemeinschaft, DFG) is acknowledged for funding this work within the project "Inferox" (MI 1247/11-1). DFT calculations were performed at the clusters of the Leibniz Supercomputing Centre (Leibniz-Rechenzentrum, LRZ).

Last but not least, I want to cordially thank **my family** and **all my friends** for their continued support and understanding, especially during the tougher times. Without them, this work would not have been possible.

Contents

Abstract	I
Abstract	I
Acknowledgments	II
Contents	IV
1 Motivation	1
2 Phenomenology and Theory	3
2.1 Thermodynamics in Crystalline Materials	3
2.2 Theory of Ferroelectricity and Related Effects	4
2.2.1 Materials in an Electric Field	4
2.2.2 Piezoelectricity and Pyroelectricity	5
2.2.3 Ferroelectricity and the Landau-Devonshire Model	7
2.2.4 Field Induced Ferroelectricity	11
2.3 Hafnia and Zirconia and their Mixtures	13
2.3.1 Structure and Properties	14
2.3.2 Ferroelectricity in doped HfO ₂	15
2.3.3 Ferroelectricity in doped ZrO ₂	17
2.3.4 Ferroelectricity in Hf _{1-x} Zr _x O ₂	18
2.3.5 Summary of the Experimental State of the Art	18
2.4 Density Functional Theory	20
2.4.1 Schrödinger Equation and the Born-Oppenheimer Approximation	20
2.4.2 Geometry Optimization and the Hellmann-Feynman Theorem	21
2.4.3 Density Functional Theory and the Kohn-Sham Equation	22
2.4.4 Basis Sets	23
2.4.5 Pseudopotentials and LAPW and PAW	24
2.4.6 Phonons and Perturbation Theory and Berry-Phase	26
3 Methods	28
3.1 Tools	28
3.1.1 ABINIT	28
3.1.2 FHI-AIMS	28

3.2	Computational Methods	29
3.2.1	Self Consistent Cycle and Structural Relaxation	29
3.2.2	Total Energy Derivatives	29
3.2.3	Stress and Strain Calculation	30
3.2.4	Electric Fields and Polarization	30
3.3	Defect Types and Defect Structure Generation	30
3.3.1	Defect Types and Defect Reactions of Charge Neutral Defects	30
3.3.2	Formation Energy and Charged Defects	36
4	Grain size and Surface / Interface Energy Model	38
4.1	Surface Energy Model	39
4.2	Interface Energy Model	41
4.3	Grain Radius Distribution	42
5	Results of DFT Calculations	44
5.1	Convergence Study	44
5.2	Total Energy and Structure	45
5.3	DFPT calculations	52
5.4	Stress and Strain	55
5.4.1	Uni-axial Stress	56
5.4.2	Uni-axial Strain	60
5.4.3	Bi-axial Stress	62
5.4.4	Bi-axial Strain	64
5.4.5	Hydrostatic Stress	66
5.5	Grain Size and Interface Energy	70
5.6	Interim Conclusion	73
5.7	Dopants and Defects	74
5.7.1	Vacancies and Interstitials	74
5.7.2	Sr-Doping	75
5.7.3	Be-Doping	77
5.7.4	Mg-Doping	78
5.7.5	Ca-Doping	79
5.7.6	Ba-Doping	80
5.7.7	Al-Doping	81
5.7.8	Y-Doping	84
5.7.9	La-Doping	86
6	Summary and Conclusion	88

Bibliography	91
Appendix A	VII
Wyckoff positions	VII
Ion position	VII
Defect position	XX
Appendix B	XXII
ABINIT input file	XXII
FHI-AIMS input file	XXIV
Appendix C	XXV
Total Energy	XXV
Elastic tensor	XXVII
Appendix D	XXVIII
List of Symbols	XXVIII
List of Figures	XXXI
List of Tables	XXXVII
Abbreviations	XXXVIII
6.1 Curriculum Vitae	XXXIX
List of Scientific Publications	XL

1 Motivation

Market demands and harsh competition in the semiconductor industry requires constant miniaturization and innovation. At the current pace, computational power and storage capacity doubles every 24 months according to Moore's Law[1, 2]. This trend has now lasted for over 50 years. This requires that the physical dimensions of the electrical devices on a silicon die such as transistors or capacitors are shrunk down by a factor of 0.7 every 24 month time period. As of 2018, the current generation of dynamic random access memory (DRAM) devices are produced with the 10 nm technology node[3, 4, 5]. At such scales, limitations imposed by physical effects like leakage currents and heat[6, 7] become more and more problematic in the further development of the technology. Furthermore, the volatile nature of the DRAM principle requires constant refresh cycles, which further increases energy consumption and heat production. This heat production comes with a hefty price tag attached, as modern data centers spend around 50 % [8, 9] of their energy bill in cooling. The cost associated with DRAMs necessitates a division in expensive but fast short-term memory and cheap but slow but non-volatile long-term data storage. Bridging the difference in access time between permanent and short-term, also called the "memory gap", is therefore of great interest. In light of these challenges, it is no surprise that in recent years new means of data storage have been developed or older but until now disregarded technologies have gathered new interest. These include restive random access memory (ReRAM)[10, 11], phase change memory (PCM)[12, 13], or ferroelectric memory. The latter comes in three different varieties.

1. Ferroelectric tunnel junctions (FTJs)[14] work by the principle of the giant tunnel electroresistance, where the tunneling resistance across a ferroelectric thin film is dependent on the polarization direction of the ferroelectric. These devices are non-volatile and can be read out non-destructively.

2. 1 transistor - 1 capacitor (1T-1C) ferroelectric random access memory (FeRAM) [15, 16, 17, 18] are in principle identical to DRAMs with the notable exception that the dielectric of the capacitor is replaced with a ferroelectric, therefore solving the volatility issue. However, the readout of a memory cell is still destructive.

3. 1 transistor (1T) devices use a field effect transistor (FET), where the gate dielectric has been replaced by a ferroelectric. The current through the channel of the ferroelectric field effect transistor (FeFET)[16, 18] is dependent on the polarization direction of the ferroelectric, allowing for non-volatility non-destructive readout.

Despite the various advantages like non-volatility, non-destructive, high read and write speeds, low power consumption, high data retention, low soft error rate, and high storage density on-chip due to the possibility of capacitor-less memory, ferroelectric memory never gained major attention from the industry. Commercial products by Ramtron[19], Fujitsu[20], and Texas Instruments[21] remained a niche market product due to problems integrating the ferroelectric material (lead zirconate titanate) into existing semiconductor manufacturing techniques[22] and the resulting large technology node of 130 nm structure width[17, 23].

The discovery of ferroelectricity in doped HfO_2 [24] and ZrO_2 [25] as well as in $\text{Hf}_{1-x}\text{Zr}_x\text{O}_2$ [26] opened up possibilities for the miniaturization of ferroelectric memory devices. As this material system is a standard material in the semiconductor industry, many problems associated with lead zirconate titanate can be avoided using $\text{Hf}_{1-x}\text{Zr}_x\text{O}_2$ instead[27]. This led to the successful demonstration of a 28 nm FeFET[28]. However, the reason for the occurrence of the phenomena in those materials is not well understood as the thermodynamic ground state phase of these materials shows no ferroelectricity. Therefore, the existence of ferroelectricity within this group of materials necessitates the stabilization of an alternative, ferroelectric phase. This dissertation is an attempt to gain a better understanding of the mechanisms responsible for the stabilization of the ferroelectric phase. In this work, simulation tools working on the atomic level and implementing density functional theory will be used to answer the following three research questions:

**Which mechanisms are responsible for the stabilization of the ferroelectric phase?
What is the role of the dopants? Can a phenomenological model be developed,
that can predict material properties from density functional theory data?**

While this dissertation uses theoretical methods, it is created in the context of a larger research project, which includes two other research groups (at NaMLab, a research focused company of TU Dresden, and at RWTH Aachen) capable of manufacturing ferroelectric thin films. Implementing the regular and mutual knowledge exchange, this dissertation is in part guided by the results provided by these institutions and hopes to achieve the same in turn.

2 Phenomenology and Theory

2.1 Thermodynamics in Crystalline Materials

The (non-degenerate) ground state of crystalline materials is a crystallographic phase, which exhibits the lowest energy of all possible configurations at a temperature of 0 K. At this temperature the entropy S of the non-degenerate (number of microstates $\Omega = 1$) ground state is 0 eV/K due to the third law of thermodynamics[29]:

$$S = k_B \ln \Omega \quad (2.1.1)$$

where k_B is the Boltzmann constant. Assuming the pressure p applied to the system is also 0 GPa, the energy of the crystal is determined only by the absolute value of the internal energy as follows from the first law of thermodynamics:

$$\Delta U = \Delta Q + \Delta W \quad (2.1.2)$$

where ΔU is the change in internal energy, while ΔQ and ΔW are the heat and work applied to the system. With temperature T , entropy S , pressure p , and volume V the change in internal energy amounts to:

$$\Delta U = TdS - pdV \quad (2.1.3)$$

with $T = 0$ and $p = 0$:

$$U = U_0 + \Delta U = U_0 + 0 = U_0 \quad (2.1.4)$$

U_0 is the internal energy in the absence of any temperature related effects including the zero point energy and is called total energy. It is composed of the electron kinetic energy and the potential energy of nucleus-nucleus, nucleus-electron, and electron-electron interactions. Therefore, U_0 is of great importance in the field of computational quantum physics and density functional theory. It will be discussed in more detail later on in chapter 2.4.

Calculating U_0 is often sufficient to determine the crystallographic phase of a crystalline material, but this is not always the case. Three macroscopic potentials, the Gibbs energy, the enthalpy, and the Helmholtz energy, are used to define the crystallographic phase.

1. The **Gibbs energy** G is the maximum amount of work a system can do at a constant

temperature and pressure[30].

$$G = U + pV - TS \quad (2.1.5)$$

2. Related to the Gibbs energy is the **enthalpy** H . A change in enthalpy is equal to the sum of the change in internal energy and the pressure-volume work of the system against its surroundings at a constant pressure.

$$H = U + pV \quad (2.1.6)$$

3. The **Helmholtz energy** F is the maximum amount of work a system can do at a constant temperature and volume[30].

$$F = U - TS \quad (2.1.7)$$

These thermodynamic potentials can be further extended to polycrystalline materials with a surface A and surface energy γ , or external electric fields E_k and polarization P .

$$G = U + pV - TS - PE_k + \gamma A \quad (2.1.8)$$

The theory behind the influence of electric fields on the free energy is discussed in chapter 2.2.3 and the influence of the surface energy in chapter 4.

2.2 Theory of Ferroelectricity and Related Effects

2.2.1 Materials in an Electric Field

Any solid permeated by an external electric field E_k ($k = x, y, z$) reacts by producing an internal counter field, thereby screening the external field. Responsible for this effect is the displacement of charges q within the solid. This results in an areal charge density or electric displacement field D_i . In a dielectric material the relation of the electric displacement field and the external electric field is given by the permittivity tensor ϵ_{ik} , which is a product of the electric field constant ϵ_0 and the relative permittivity tensor k_{ik} . Using the Einstein summation convention, this can be written as:

$$D_i = \epsilon_{ik} E_k = \epsilon_0 k_{ik} E_k \quad (2.2.1)$$

By separating the vacuum contribution $\epsilon_0 E_k$ ($k_{ik} = \delta_{ik}$) from the displacement field from

the material contribution $k_{ik} > \mathbf{1}$ results in the material property susceptibility χ_{ik} .

$$\chi_{ik} = k_{ik} - \delta_{ik} \quad (2.2.2)$$

$$D_i = \epsilon_0(\delta_{ik} + \chi_{ik})E_k = \epsilon_0\delta_{ik}E_k + \epsilon_0\chi_{ik}E_k \quad (2.2.3)$$

The susceptibility of a given material determines how easy charges in the material can follow the external electric field. Therefore, free charge carriers like electrons in a metal result in a large susceptibility, while the movement of ions, surrounded and restricted by neighboring atoms, only contribute moderately to the susceptibility. Electrical insulators, despite not having free electrons, still possess an electronic contribution to the susceptibility since the electron gas still reacts to external electric fields. However, the resulting susceptibility is much smaller than in conductors.

$$\chi_{ik} = \chi_{ik(\text{ionic})} + \chi_{ik(\text{electronic})} \quad (2.2.4)$$

As a result of the displacement in an electric field, charge q accumulates at a surface A_i of a solid. The resulting areal charge density is called polarization P_i :

$$P_i = \frac{q}{A_i} = \epsilon_0\chi_{ik}E_k \quad (2.2.5)$$

All materials express this behavior and are called dielectrics. A common convention in the field of high-k materials and ferroelectrics is $D_i = P_i$ as $\chi \gg \mathbf{1}$ for these materials. Nonlinear responses to electric fields exist as well with corresponding proportionality constants. Additionally, the susceptibility is generally dependent on the frequency of the applied electric field. However, neither of these effects will be discussed in this thesis.

2.2.2 Piezoelectricity and Pyroelectricity

In crystalline solids, additional effects can influence the electrical polarization. Of the 32 existing crystallographic point groups, 20 react with a change in polarization in response to mechanical forces. The cause for this behavior is the non-centrosymmetric nature of the lattice[31]. Deformation of the crystals leads to a separation of the barycenters of positive and negative charges. This is depicted in FIG. 2.1. These materials are called piezoelectric. The relation between the applied stress σ_{kl} and the resulting polarization P_i or electric field E_i is:

$$P_i = d_{ikl}\sigma_{kl} \quad (2.2.6)$$

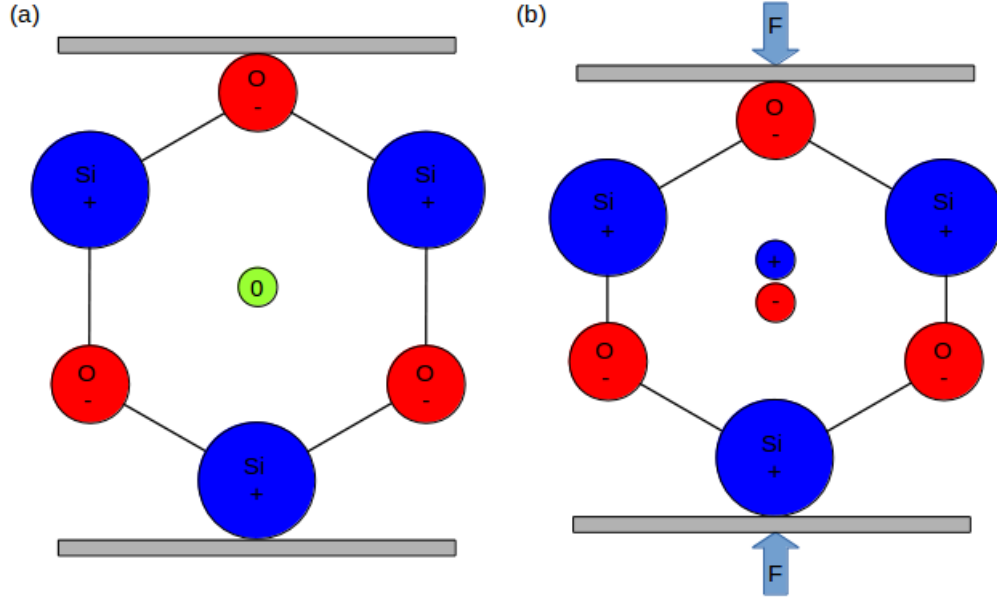


FIG. 2.1: Example for separation of charge barycenters under mechanical stress. (a) relaxed solid, the charge barycenters overlap, no polarization. (b) strained solid with separation of charge barycenters resulting in a polarization

$$E_i = g_{ikl}\sigma_{kl} \quad (2.2.7)$$

The factors d_{ikl} and g_{ikl} are the piezo coefficients. In a similar fashion, a relationship between strain τ_{kl} and a resulting polarization or electric field can be established with corresponding piezo coefficients h_{ikl} and e_{ikl} .

$$P_i = h_{ikl}\tau_{kl} \quad (2.2.8)$$

$$E_i = e_{ikl}\tau_{kl} \quad (2.2.9)$$

For each of these four effects a converse effect exists[31]. This means that an applied electric field results in a mechanical deformation of the piezoelectric solid. If the polarization of a solid is also temperature dependent, the material is also pyroelectric.

$$\Delta P_i = p_i\Delta T \quad (2.2.10)$$

Since the temperature is a scalar quantity and the polarization is a vector, the pyroelectric coefficient must be a vector as well. It furthermore follows, that $p_i \parallel P_i$. This means, that out of the 20 piezoelectric point groups with at least one polar direction, only those 10 with only one polar axis can exhibit pyroelectricity. Therefore, all pyroelectric materials are also piezoelectric, but not all piezoelectric materials are pyroelectric[31].

2.2.3 Ferroelectricity and the Landau-Devonshire Model

If the polarization of a pyroelectric material is reversible by an external electric field of sufficient strength, the material is called ferroelectric. The electric field strength at which reversal of polarization occurs is called the coercive field strength \mathbf{E}_c , the value of the polarization at zero external field is called remanent polarization \mathbf{P}_r . The polarization as a function of electric field strength forms a hysteresis loop as depicted in figure 2.2 (a).

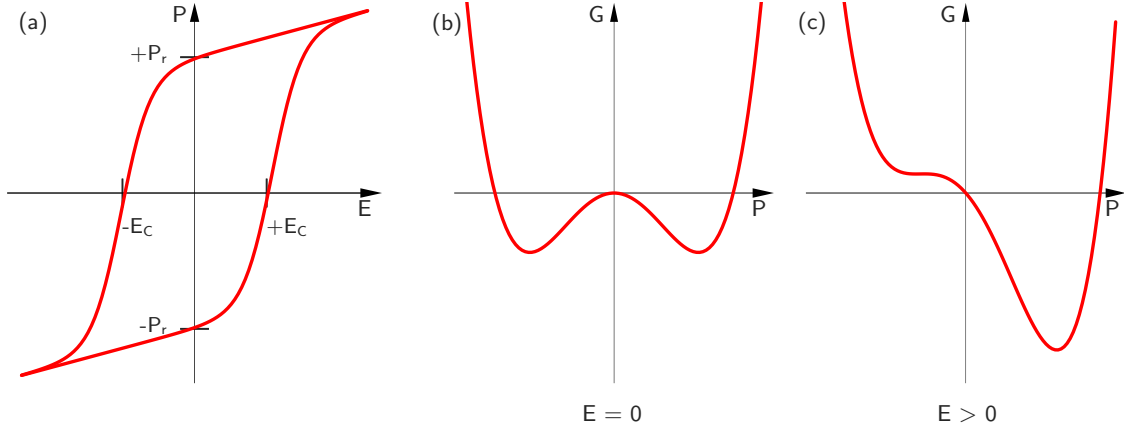


FIG. 2.2: (a) Hysteresis loop of a ferroelectric. The Landau-Devonshire model predicts vertical edges, but experiments often produce sloped edges (sketched here). (b) double-well potential for the two polarization states of a ferroelectric without an external electric field, (c) double-well potential for the two polarization states of a ferroelectric with an external electric field favoring one polarization state.

The existence of the two polarization states necessitates the existence of two minima of equal depth in the potential energy surface, separated from each other by some energy barrier (see figure 2.2 (b)). A common phenomenological description of ferroelectricity is the Landau-Devonshire model[31, 32], which describes the potential energy surface around the two minima as a 6th order polynomial of the polarization P . As a consequence of the parity of the two minima, all uneven polynomial orders must be zero in the field free case.

$$g = \frac{G}{V} = \frac{1}{2}c_2P^2 + \frac{1}{4}c_4P^4 + \frac{1}{6}c_6P^6 - E_kP \quad (2.2.11)$$

In a paraelectric, the 4th and 6th orders are zero ($c_4 = c_6 = 0$) and the minimum of the Gibbs energy G coincides with $P = 0$. It also follows, that factor c_2 is proportional to the inverse of the susceptibility, which follows a Curie-Weiss law[33, 31] with the Curie temperature T_c and a constant C :

$$c_2 = \frac{1}{\epsilon_0\chi} = \frac{T - T_c}{C} \quad (2.2.12)$$

The Curie temperature can be equal to or less than the phase transition temperature T_p at which the paraelectric phase transitions into the ferroelectric phase. Below T_p the 4th and 6th order term of the Gibbs energy can therefore no longer be neglected. The highest order of equation 2.2.11 must always be positive since otherwise, the Gibbs energy would become indefinitely negative for $P \gg 0$. Therefore, two distinct cases can be defined for the temperature driven transition into a ferroelectric phase:

1. First order phase transitions, where $c_6 > 0$ and $c_4 < 0$
2. Second order phase transitions, where $c_6 \approx 0$ and $c_4 > 0$

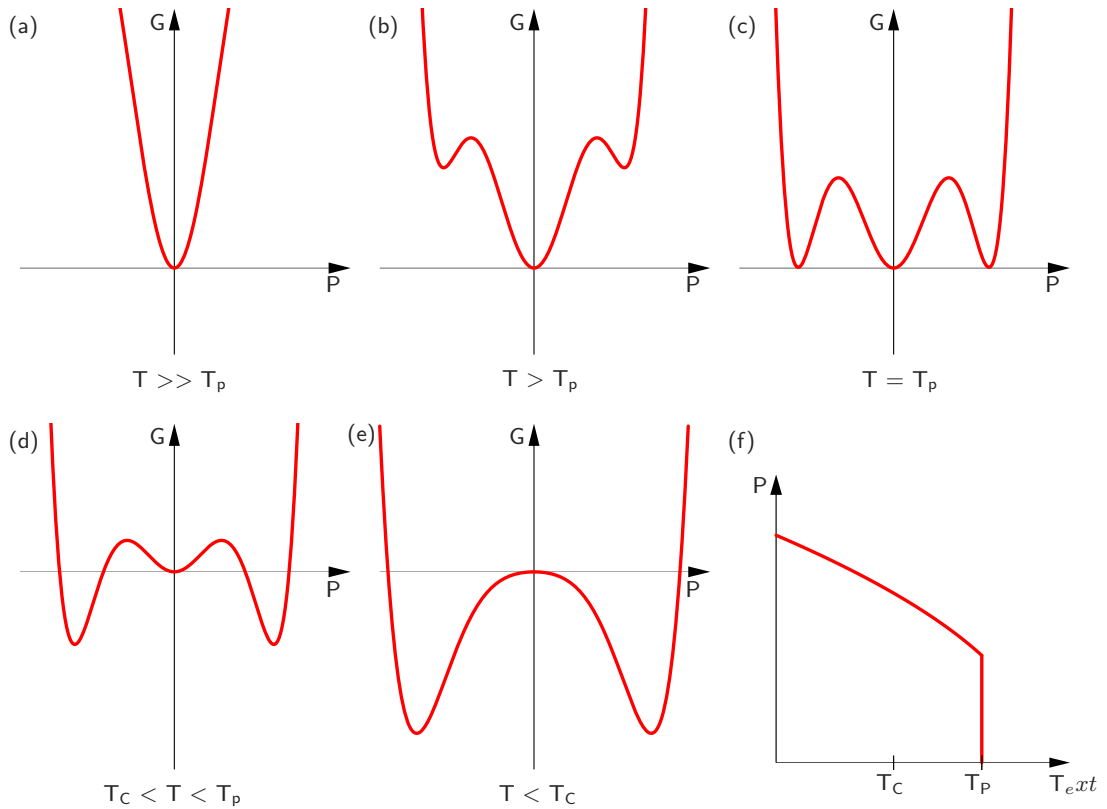


FIG. 2.3: (a)-(e) Landau-Devonshire model of a first order phase transition from paraelectric to ferroelectric in the various temperature ranges (explanation see text). (f) Resulting polarization as a function of temperature.

First order phase transitions are characterized by the existence of a sixth order term in the Gibbs energy and the fact that T_c and T_p do not coincide. The polarization can be calculated as a function of temperature by inserting equation 2.2.12 into equation 2.2.11 and finding the minima of $G = 0$:

$$\mathbf{P}_r = P(E = 0) = \pm \sqrt{\frac{|c_4| + \sqrt{c_4^2 - \frac{4c_6(T-T_c)}{C}}}{2c_6}} \quad (2.2.13)$$

Figure 2.3 shows the Gibbs energy for different temperature ranges during a first order phase transition. (a) shows the Gibbs energy for temperatures far above T_p for which only the paraelectric phase exists and the Gibbs energy is parabolic with its minimum at $P = 0$. If the temperature approaches the phase transition temperature, localized minima form at $P \neq 0$ (b). The paraelectric phase is still stable, but the ferroelectric phase is metastable. At exactly the phase transition temperature, three minima exist, one for $P = 0$ and two for $P \neq 0$ (c). Both the ferroelectric phase and the paraelectric phase coexist. In the temperature range between the phase transition temperature and the Curie temperature, the ferroelectric phase is stable and the paraelectric phase is metastable (d). The minimum at $P = 0$ is only local. At temperatures below the Curie temperature, the local minimum at $P = 0$ disappears and becomes a local maximum (e). Figure 2.3 (f) shows the polarization as a function of temperature.

Second order phase transitions are characterized by the lack of a sixth order term in the Gibbs energy and the fact that T_c and T_p do coincide. The polarization can be calculated in a similar manner as previously done for the first order phase transition, but the resulting equation is much simpler due to the lack of the 6th order term:

$$\mathbf{P}_r = P(E = 0) = \pm \sqrt{\frac{T - T_c}{C c_4}} \quad (2.2.14)$$

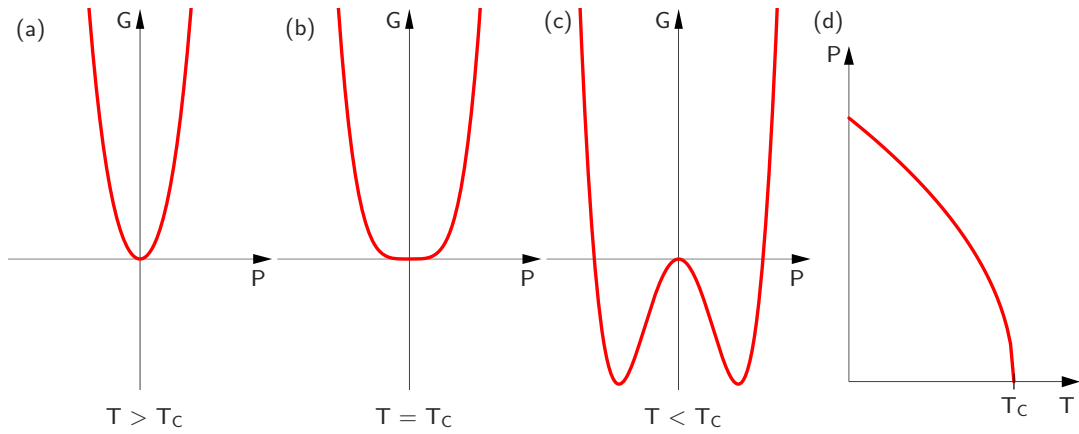


FIG. 2.4: (a)-(c) Landau-Devonshire model of a second order phase transition from paraelectric to ferroelectric in the various temperature ranges (explanation see text). (d) Resulting polarization as a function of temperature.

As a consequence of equation 2.2.14, the polarization drops continuously with increasing temperature and reaches zero at the Curie temperature as shown in figure 2.4 (d). Figure 2.4 (a) shows the Gibbs energy for temperatures far above T_p for which only the paraelectric phase exists and the Gibbs energy is parabolic with its minimum at $P = 0$. At the Curie temperature (b) the minimum at $P = 0$ splits into two separate minima which shift continuously towards higher polarization values when the temperature is further decreased (c).

The Landau-Devonshire model shows, that all ferroelectric materials are also pyro- and therefore piezoelectric as depicted in figure 2.5 due to their structural relationships. However, pyro- and piezoelectric materials are not necessarily always ferroelectric.

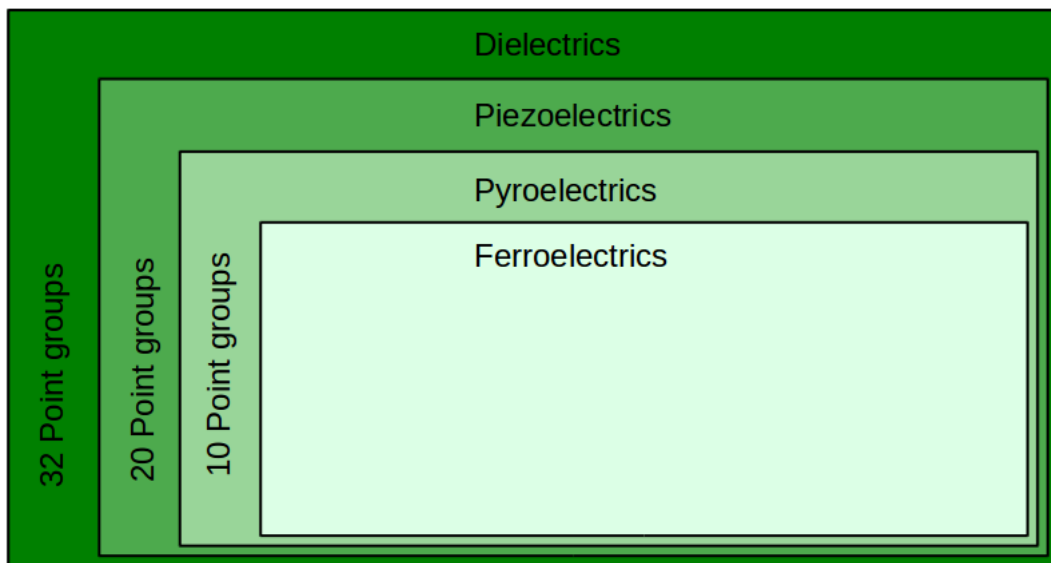


FIG. 2.5: Euler diagram depicting the structural relation ship between dielectrics, piezoelectrics, pyroelectrics, and ferroelectrics.

Typical ferroelectric materials are perovskite-type oxides of the ABO_3 class, where A and B are II- and IV-valent cations, respectively. This class of materials is named after the mineral perovskite ($CaTiO_3$). The ideal perovskite is a cubic cell with the II-valent cations on each cube corner position $(0, 0, 0)$ and the IV-valent cation in the body-centered position $(1/2, 1/2, 1/2)$. The oxygen anions sit on the face-centered positions. The cubic unit cell may be subject to various symmetry breaking distortions, heavily influenced by the relative size of A and B type cations. A displacement of the center ion leads to the formation of a polar axis and results in ferro-, pyro-, and piezoelectric properties. This is depicted in figure 2.6 in the example of lead zirconate titanate. Well known perovskites that show this kind of distortion are BTO ($BaTiO_3$), STO ($SrTiO_3$), BST ($Ba_xSr_{1-x}TiO_3$), and PZT ($PbZr_xTi_{1-x}O_3$).

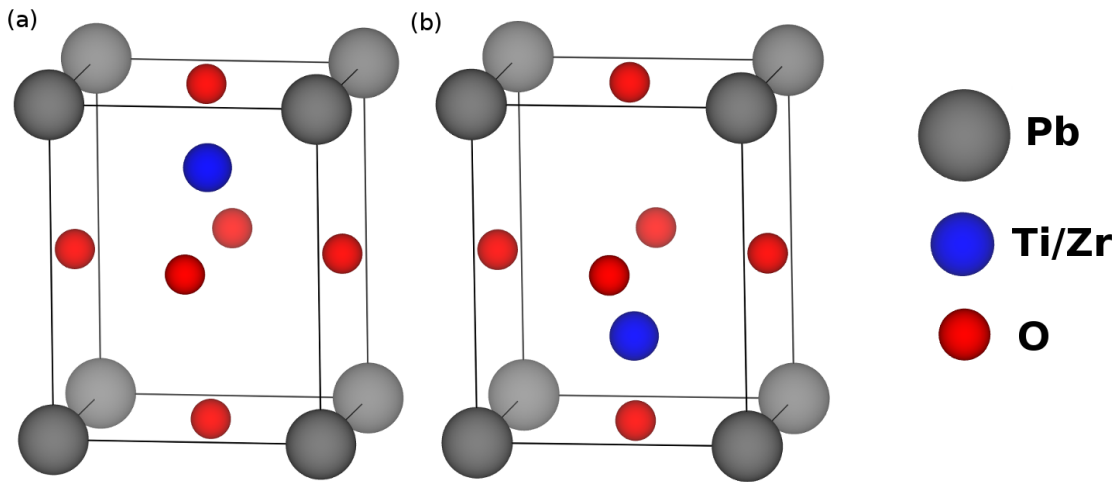


FIG. 2.6: The two polarization states of ferroelectric lead zirconate titanate.

2.2.4 Field Induced Ferroelectricity

Figure 2.3 depicts the Gibbs energy for various temperatures at zero electric field. However, an interesting phenomenon can be observed if an electric field is applied, in particular in the case of $T > T_p$ in sub-figure (b). The results of this are shown in figure 2.7. Figure 2.7 (b) repeats the case $T > T_p$ in the absence of an electric field, where a global minimum of the Gibbs energy exists for $P = 0$. Two local minima exist for $P \neq 0$, but are energetically unfavorable. Keeping the temperature constant while increasing the external electric field lowers one of the local minima while raising the other. Further increasing the electric field causes the former to become the new global minimum, but a secondary local minimum may still exist close to $P = 0$ (c). At this point, both states may coexist. The small shift in polarization of this secondary minimum is caused by dielectric polarization. Reaching a critical field strength E_c the secondary minima disappears in favor of a saddle point and the crystal can completely switch into the polar state without passing over an energy barrier (d). Figure 2.7 (e) depicts the Gibbs energy for the saturation state, for which an increase

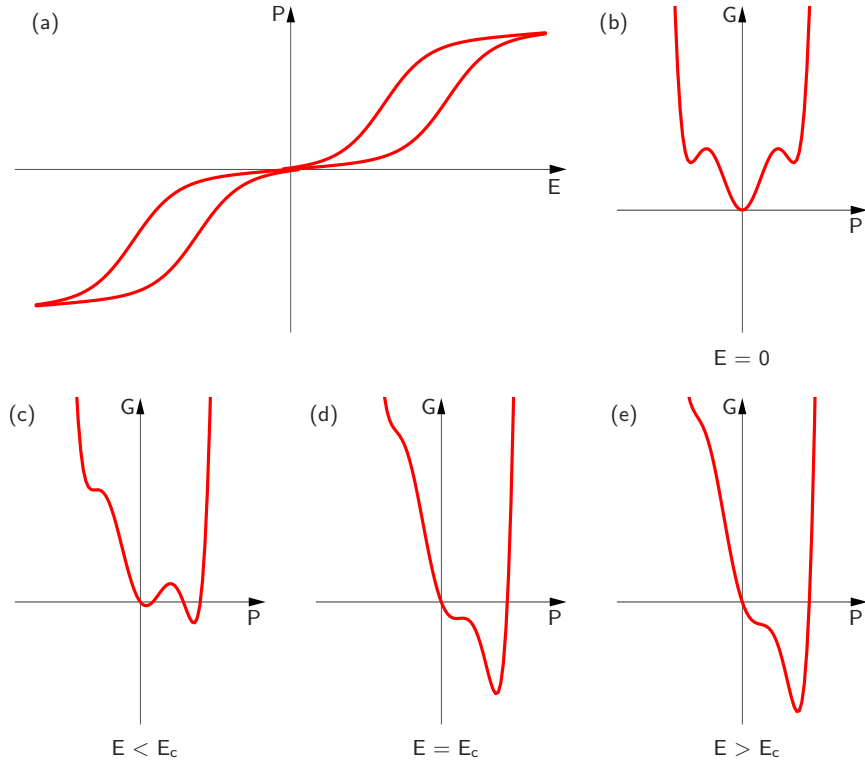


FIG. 2.7: (a) Hysteresis curve of field induced ferroelectricity. (b)-(e) Landau-Devonshire model of field induced ferroelectricity for various electric fields (explanation see text). The temperature is held constant.

in polarization can only be achieved by dielectric displacement. The resulting Hysteresis curve is depicted in (a). Due to its nature, this phenomenon is referred to as **field induced ferroelectricity**. Typical for this phenomenon is its constricted hysteresis curve. In a material, domains with different values for T_p may exist due to inhomogeneities of grain size or dopant concentration. Therefore, ferroelectricity and field-induced ferroelectricity may occur simultaneously. The resulting hysteresis curve has non-zero values for the remanent polarization but is still somewhat constricted. Similar hysteresis curves can be caused by anti-ferroelectricity. However, this phenomenon is caused by an anti-parallel orientation of ferroelectric domains, rather than a phase transition. Since field induced ferroelectricity requires the existence of secondary minima, it can only occur in first order ferroelectrics above the phase transition temperature.

2.3 Hafnia and Zirconia and their Mixtures

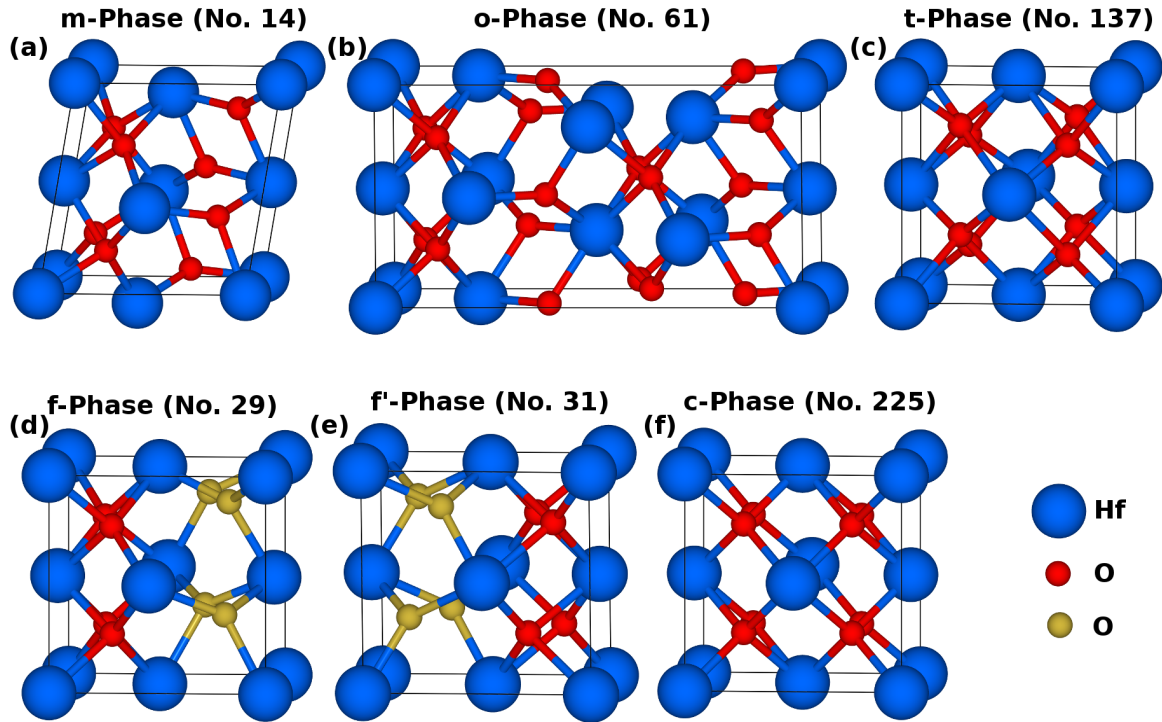


FIG. 2.8: The six polymorphs of the $\text{Hf}_{1-x}\text{Zr}_x\text{O}_2$ system. Depicted are (a) the monoclinic phase, (b) the orthorhombic phase, (c) the tetragonal phase, (d) the ferroelectric phase, (e) the second ferroelectric phase, and (f) the cubic phase. Blue ions are Hf or Zr ions, red are oxygen ions. The golden ions in (d) and (e) are oxygen ions, that are visibly displaced from centrosymmetric positions and therefore the cause of the polarization of the two ferroelectric phases

Hafnium(IV) oxide or hafnia or HfO_2 , as well as zirconium(IV) oxide or zirconia or ZrO_2 , are the binary oxides of the metals hafnium and zirconium. Both elements are chemically and physically very similar to each other in both their pure and oxidized form [34, 35]. However, hafnium (Element No. 72) is significantly heavier than zirconium (Element No. 40) with atomic masses of 178.49 u and 91.22 u respectively [36]. Despite this, both elements are approximately of the same size [37, 38] due to an effect called lanthanide contraction [39]. Both oxides are almost identical in their atomic structure and unit cell volume [40], see Chapter 2.3.1. This allows for the formation of a continuous solid solution $\text{Hf}_{1-x}\text{Zr}_x\text{O}_2$ with x ranging from 0 to 1 [34]. $\text{Hf}_{1-x}\text{Zr}_x\text{O}_2$ and ($\text{Hf}_{0.5}\text{Zr}_{0.5}\text{O}_2$ in particular) are often abbreviated as HZO. The following chapters will summarize the literature concerning the structure and properties of this material system with a special focus on ferroelectric properties and related phenomena.

2.3.1 Structure and Properties

ZrO₂ and to a lesser extent HfO₂, can be found naturally in the form of the mineral baddeleyite. Baddeleyite mostly consists of ZrO₂ with HfO₂ as a substituting impurity due to their relative abundance. The crystallographic phase of baddeleyite is the primitive monoclinic space group P2₁/c (No. 14), which is also the ground state of the Hf_{1-x}Zr_xO₂ material system. The phase with a 12-atomic unit cell is centrosymmetric and therefore not ferroelectric. For the sake of readability, this phase will be referred to as m-phase. The k-value of the m-phase is approximately 20 [41].

Hf_{1-x}Zr_xO₂ transforms thermally driven into a primitive tetragonal P4₂/mnc phase (No. 137). The transition temperature depends on the value of x as well as sample preparation and history. For the pure oxides HfO₂ and ZrO₂ the equilibrium temperatures T₀ for the phase transition are reported by Wang et al. as 2052 K and 1367 K respectively [42]. This tetragonal phase will be referred to as the t-phase. The t-phase is of technological interest due to the high k-value of approximately 47 [41], leading to successful applications as a dielectric in DRAM-capacitors (ZrO₂) [41] and as gate oxides in CPU-transistors (HfO₂) [2]. The phase transition between the m- and t-phase ZrO₂ can also be exploited for transformation toughening [43, 44] due to the size difference of the two polymorphs (see Tables 5.1-5.3). The t-phase has a 6-atomic centrosymmetric unit cell and is therefore not ferroelectric.

Further heating results in a transformation into the face-centered cubic Fm $\bar{3}$ m phase (No. 225) at 2370 K (ZrO₂) and 2600 K (HfO₂) [35]. This phase will be referred to as the c-phase. The c- and t-phase are structurally very similar. The main differences are a change in the c/a ratio from 1.02 (t-phase) to values around 1.00 (c-phase) [45, 26] and a displacement in ionic positions. This displacement corresponds to a soft phonon mode with imaginary frequency [46]. This has implications for first principles calculations like the ones presented later in this work. It means that a barrier-free transition path from the c- to the t-phase exists. Ab initio codes searching for a local energy minimum sometimes fail to find a c-phase for this reason. The c-phase has a 3-atomic centrosymmetric unit cell and is therefore not ferroelectric. The k-value of the c-phase is approximately 37 [41]. Cubic HfO₂ and ZrO₂ melt at 2800 K and 2690 K respectively [35].

Besides these three phases, a variety of orthorhombic phases exist. The non-centrosymmetric Pca2₁ (No. 29) has been conjectured to be the source of ferroelectricity in the Hf_{1-x}Zr_xO₂ system by Böscke et al. [24] in 2011. This conjecture is consistent with ab initio calculations, which consistently found this phase to be the energetically most favorable polar phase in the Hf_{1-x}Zr_xO₂ system [47, 48, 49, 50, 51]. Experimental evidence for this claim was published 2015 by Sang et al. who identified the Pca2₁ phase in Gd-doped HfO₂ by aberration corrected high-angle annular dark-field scanning transmission electron microscopy [52]. The polar na-

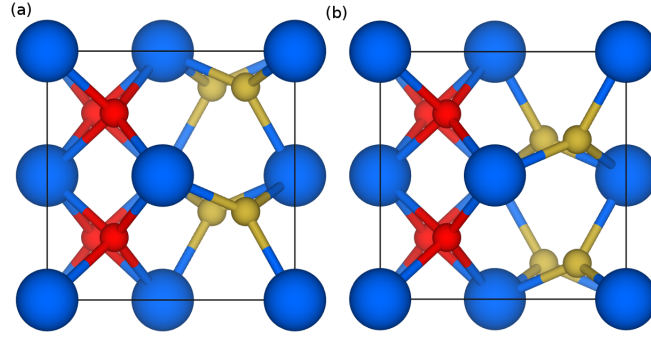


FIG. 2.9: The two polarization states of ferroelectric HfO_2

ture of this phase is caused by the oxygen sublattice. Four of the eight oxygen ions in the 12-atomic unit cell are visibly displaced from the center position along the z -axis. This leads to two structurally equivalent structures with opposite polarization, which are displayed in Fig. 2.9. In order to better distinguish this important phase from the other orthorhombic phases, the $\text{Pca}2_1$ will be referred to as f-phase (f for ferroelectric).

A second non-centrosymmetric phase $\text{Pmn}2_1$ (No. 31) has been suggested by Huan et al., but found to be higher in energy[47]. Furthermore, the results of the previously mentioned transmission electron microscopy study by Sang et al. were inconsistent with this phase. The unit cell consists of 6 atoms. To separate this phase from the other orthorhombic phases, the $\text{Pmn}2_1$ will be referred to as f'-phase.

A third orthorhombic phase can be observed under high pressure. However, this Pbca (No. 61) phase is centrosymmetric and therefore not ferroelectric. A transition pressure in the range of 4 GPa to 12 GPa [53, 54, 55, 56] has been reported. Unlike the other orthorhombic phases, the unit cell of Pbca has 24 atoms. It will be referred to as o-phase. Wyckoff positions of all phases are recorded in Table 6.1 in Appendix A and experimental values for lattice parameters, unit cell volume, and density of all crystallographic phases can be found in the tables 5.1 to 5.3 in chapter 5 together with ab initio values. Fig. 2.8 depicts the unit cells of all phases, with the t-and c-phase expanded to 12 atoms for better comparison.

2.3.2 Ferroelectricity in doped HfO_2

The ferroelectricity of HfO_2 was first discovered in Si-doped thin films by Böske et al.[24] Thin films in the range of 7 nm to 10 nm were produced with atomic layer deposition (ALD) with a dopant concentration ranging from 2.5 mol% to 6 mol%, whereby films with less than 4 mol% exhibited ferroelectric behavior. Increasing the dopant concentration above that limit resulted in antiferroelectric hysteresis loops and subsequently paraelectric hysteresis loops. The antiferroelectric hysteresis loops are commonly attributed to field induced ferroelectricity[48]. A more detailed study by Richter et al.[57] observed ferroelectric behavior in 36 nm thin films, particularly with an ALD cycle ratio of 24:1 and 26:1 $\text{HfO}_2:\text{SiO}_2$. Si-doped

HfO₂ is also an excellent pyroelectric with a pyroelectric coefficient of $-46.2 \mu\text{C}/(\text{K m}^2)$ [58].

Starschich et al. found weak ferroelectricity in 42 nm Mg-doped HfO₂ thin films produced by chemical solution deposition (CSD) [59]. Varying the dopant concentration from 3.75 mol % to 15 mol %, the maximum remanent polarization \mathbf{P}_r of $3 \mu\text{C}/\text{cm}^2$ was measured at a dopant concentration of 7.5 mol %. In samples with 5 mol % and 11 mol % ferroelectric switching peaks could be observed as well.

In Sr-doped HfO₂, ferroelectricity was observed in both ALD and CSD films, but the dopant concentration range for which ferroelectricity could be observed (also called ferroelectric process window) varies between the two methods. Schenk et al. observed ferroelectricity in 10 nm ALD deposited HfO₂ from 1.7 mol % to 7.9 mol % with the maximum remanent polarization at 3.4 mol % according to the issued erratum[60]. In contrast Starschich et al. found ferroelectricity in 42 nm CSD deposited HfO₂ in the full experimental range from 3.75 mol % to 15 mol % with the maximum remanent polarization at 7.5 mol %[59]. In the same study, Starschich et al. investigated Ba-doping as well and found a ferroelectric process window from 3.75 mol % to 11 mol % with the maximum remanent polarization at 7.5 mol %.

Ferroelectricity in Al-doped HfO₂ was discovered by Mueller et al.[61] in 16 nm thick ALD films deposited on TiN electrodes. At a dopant concentration of 4.3 mol % ferroelectric hysteresis loops were observed, while at a dopant concentration of 8.5 mol % antiferroelectric hysteresis loops in combination with a X-ray diffraction (XRD) pattern consistent with the t-phase were observed¹. In a 2017 study by Park et al.[62] similar observations were made, but unfortunately, only ALD cycle ratios were given for the dopant concentration. Cycle ratios in the range of 100:3 and 100:4.2 resulted in a ferroelectric polarization. However, the authors estimated, that these ratios correspond to a dopant concentration ranging from 1 cat % to 3 cat % (cat = cation). At higher concentrations, the t-phase was formed. Yoo et al.[63] investigated ALD deposited Al-doped HfO₂ films on Mo electrodes in the range from 11 nm to 100 nm and a dopant concentration ranging from 0.5 % to 10 %. No f-phase could be detected in the XRD, but a m- to t-phase transition was observed between 1.4 % and 2 %. HfO₂ films with 4.7 % or more did not crystallize even after a thermal annealing at 580 °C. CSD deposited 42 nm films by Starschich et al. [59] showed only a very weak polarization of $6 \mu\text{C}/\text{cm}^2$ in Al-doped HfO₂ at 5.2 mol %.

Müller et al. [64] discovered ferroelectric Y-doped HfO₂ in 10 nm thick ALD films with a ferroelectric process window ranging from 3 mol % to 9 mol %. Above that limit, the c-phase was found. The maximum polarization was found around 5 mol % to 6 mol % coinciding with

¹Percentages used in this section and onwards are recited as they appeared in the original works. However, these percentages are often not properly defined and used inconsistently or incorrectly by various authors. Particularly the use of mol % and at % is often ill-defined. After correspondence with some of the authors, it seems they all mean the same: the ratio between dopant cations and the overall number of cations. The units cat %, mol %, at %, and f.u. % are therefore interchangeable. A definition of the unit f.u. % is given at the end of section 3.3.1

an increase of the c-phase fraction. This is consistent with the data from Kita et al. [65] who found the c-phase in the range of 4 at % to 17 at % (at = atom). CSD results from Starschich et al.[66] found a ferroelectric process window from 3.75 mol % to 7.5 mol % with the maximum at 5.2 mol %. The presence of a c-phase was confirmed by XRD. Epitaxial Y-doped HfO₂ films of 15 nm thickness were grown by Shimizu et al.[67, 68] by pulsed laser deposition (PLD) on yttrium oxide-stabilized zirconium oxide substrate. The 7 cat % doped films were found to be ferroelectric with a saturated polarization value of 16 $\mu\text{C}/\text{cm}^2$. Ferroelectricity can also be produced by co-sputtering (PVD = physical vapor deposition) Y into HfO₂ [69]. However, the ferroelectric process window differs widely from ALD produced films as ferroelectricity was only observed in the range from 0.9 mol % to 1.9 mol % in the 12 nm thick films.

A 2013 study by Müller et al.[70] reported the discovery of ferroelectric La-doped HfO₂. A more detailed investigation by Chernikova et al.[71] found a ferroelectric process window ranging from 2.1 at % to 3.7 at % in 10 nm ALD deposited HfO₂. At a dopant concentration of 5.8 at % the films had completely transformed into the c-phase. This is in contrast to a study by Schröder et al.[72] who found a ferroelectricity up to 20 cat %, although a significant cubic phase fraction was observed as well. CSD results from Starschich et al.[59] mirror those of Y-doping with the maximum polarization at 5.2 mol % dopant concentration in 42 nm thick films.

There are some other dopants for which ferroelectricity has been observed in HfO₂. However, as these dopants are not subject of this work, they will not be discussed in more detail. These dopants are Ga, In, Nd, Sm, Er, Co, Ni [59] for CSD films, N, Sc, and Ge[73] for PVD films and Gd [74] for ALD films. The antiferroelectric hysteresis loops found in Si- and Al-doped HfO₂ are commonly attributed to field induced ferroelectricity rather than true antiferroelectricity[48]. This indicates, that the Hf_{1-x}Zr_xO₂ material system follows a first-order phase transition with the tetragonal phase as the paraelectric phase/transition state.

2.3.3 Ferroelectricity in doped ZrO₂

Ferroelectric doped ZrO₂ is not as well studied as ferroelectric doped HfO₂. Starschich et al.[75] investigated several dopants in 60 nm and 100 nm CSD deposited ZrO₂ films. Mg-doping resulted in pinched Hysteresis loops from 2.2 % to 9 %. However, piezo-measurements suggest, that the field-induced phase transition originates from a c-rather than a t-phase. In-doping provided similar results. However, in contrast to HfO₂ doping with La or Y only lead to the stabilization of the c-phase. Yoo et al.[63] investigated Al-doped ALD deposited ZrO₂ films, but found no ferroelectricity.

2.3.4 Ferroelectricity in $\text{Hf}_{1-x}\text{Zr}_x\text{O}_2$

A lot of research has been focused on the ferroelectricity of $\text{Hf}_{1-x}\text{Zr}_x\text{O}_2$. This material system is of particular interest, as the two oxides form a continuous solid solution, the mixture of Zr into Hf does not necessitate any oxygen vacancies, and no (intentional) doping is required to induce ferroelectricity. The first investigation into ferroelectric 9 nm ALD deposited $\text{Hf}_{1-x}\text{Zr}_x\text{O}_2$ films by Müller et al.[26] in 2012 found an increase in the remanent polarization \mathbf{P}_r when increasing the value of x from 0 to 0.5. A further increase in the Zr content leads to a decrease in \mathbf{P}_r as the hysteresis loops became more and more pinched. Pure HfO_2 did not show any ferroelectricity while pure ZrO_2 showed only field induced ferroelectricity. Park et al.[76] found an inverse correlation between film thickness and remanent polarization in $\text{Hf}_{0.5}\text{Zr}_{0.5}\text{O}_2$ films. 5.5 nm and 10 nm films exhibited the highest \mathbf{P}_r values around $16 \mu\text{C}/\text{cm}^2$, while in 17 nm and 25 nm films \mathbf{P}_r decreased to $10 \mu\text{C}/\text{cm}^2$ and $5 \mu\text{C}/\text{cm}^2$ respectively. Accompanying XRD measurements revealed a decrease in t- and f-phase fractions and an increase in m-phase fractions in the range of 10 nm to 25 nm film thickness. A similar effect was shown by Pešić et al.[77], who also observed a size effect in doped HfO_2 . A follow-up study found a positive correlation between grain size and film thickness [78, 79]. The larger surface to volume ratio of smaller grains in thinner films and the associated surface/interface energy is responsible for stabilization of the t- and f-phase [80, 50, 51]. Therefore, Kim et al.[79] were able to produce 40 nm thick ferroelectric $\text{Hf}_{0.5}\text{Zr}_{0.5}\text{O}_2$ films by introducing Al_2O_3 interlayers limiting the grain size, while 40 nm thick $\text{Hf}_{0.5}\text{Zr}_{0.5}\text{O}_2$ films without interlayers were paraelectric. The results were later reproduced by Riedel et al.[81]. This grain size effect enables the production of ferroelectric pure HfO_2 and ZrO_2 films without the need of dopants. Polakowski et al.[82] managed to observe ferroelectricity with a remanent polarization of $10 \mu\text{C}/\text{cm}^2$ in undoped HfO_2 by reducing the film thickness to 6 nm. CSD deposited ZrO_2 films by Starschich et al.[25] can exhibit ferroelectricity over a large range of film thickness, due to the columnar nature of the grains grown from CSD. This permitted the growth of ferroelectric ZrO_2 films ranging from 195 nm to 390 nm film thickness without a loss in remanent polarization. Theoretical models describing the grain size effect in both ALD and CSD deposited thin films for the entire $\text{Hf}_{1-x}\text{Zr}_x\text{O}_2$ system are developed in section 4 and were published prior to this dissertation in the journal of applied physics[50, 51].

2.3.5 Summary of the Experimental State of the Art

Summarizing the experimental data available, there are three parameters in the $\text{Hf}_{1-x}\text{Zr}_x\text{O}_2$ system that are accessible by both experimental and theoretical approaches in order to optimize the ferroelectric and dielectric properties of $\text{Hf}_{1-x}\text{Zr}_x\text{O}_2$ thin films:

1. The ratio x of Hf to Zr within the thin film.
2. The shape and size of grains which make up the thin film
3. The type and concentration of dopants and defects within the thin film.
4. The sequence of ALD-layers.
5. Temperature and duration of the annealing process.

For the purpose of comparing simulation results with experimental results, the following ferroelectric process windows of doped HfO_2 are extracted from the literature listed in the previous chapters: Mg exhibits ferroelectricity in the dopant concentration range from 5 f.u. % to 11 f.u. %, Sr from 1.7 f.u. % to 15 f.u. %, Ba from 3.75 f.u. % to 11 f.u. %, Al from 1.5 f.u. % to 4.5 f.u. %, Y from 3 f.u. % to 9 f.u. %, and La from 4 f.u. % to 20 f.u. % (f.u. = formula unit).

2.4 Density Functional Theory

Density Functional Theory (DFT) [83, 84] is a computational method to solve many-electron problems in quantum mechanics. As such, it is a powerful research tool, particularly for chemical and materials science. DFT derives its name from the electron density, which is used to calculate the total energy and related properties of a desired atomic system. The following chapters will give a brief introduction to DFT as it relates to this work. Therefore, the introduction will be restricted to non-relativistic, time-independent, ground state calculations.

2.4.1 Schrödinger Equation and the Born-Oppenheimer Approximation

The energy E of a stationary quantum mechanical system is derived from the Hamilton-operator \hat{H} acting on the wave function $\Psi(\vec{r}, \vec{R})$ [85]:

$$E = \frac{\langle \Psi(\vec{r}, \vec{R}) | \hat{H} | \Psi(\vec{r}, \vec{R}) \rangle}{\langle \Psi(\vec{r}, \vec{R}) | \Psi(\vec{r}, \vec{R}) \rangle} \quad (2.4.1)$$

The nuclear coordinates are given by $\vec{R} = (\vec{R}_1, \vec{R}_2, \dots, \vec{R}_N)$ and the electronic coordinates are given by $\vec{r} = (\vec{r}_1, \vec{r}_2, \dots, \vec{r}_n)$. In a system of n electrons with mass m_e and N nuclei with mass M_I , the Hamiltonian can be split into individual contributions:

$$\hat{H} = \hat{T}_e + \hat{T}_N + \hat{V}_{ee} + \hat{V}_{NN} + \hat{V}_{Ne} \quad (2.4.2)$$

\hat{T}_e and \hat{T}_N are the kinetic operators of the electrons and nuclei, while \hat{V}_{ee} , \hat{V}_{NN} , and \hat{V}_{Ne} are the Coulomb operators for the interaction between electrons, between nuclei, and between electrons and nuclei respectively.

$$\hat{T}_e = \sum_{i=1}^n \frac{\hbar^2}{2m_e} \nabla^2 \quad (2.4.3)$$

$$\hat{T}_N = \sum_{I=1}^N \frac{\hbar^2}{2M} \nabla^2 \quad (2.4.4)$$

$$\hat{V}_{ee} = \frac{e}{4\pi\epsilon_0} \sum_{i<j} \frac{1}{|\vec{r}_i - \vec{r}_j|} \quad (2.4.5)$$

$$\hat{V}_{NN} = \frac{e}{4\pi\epsilon_0} \sum_{I<J} \frac{Z_I Z_J}{|\vec{R}_I - \vec{R}_J|} \quad (2.4.6)$$

$$\hat{V}_{eN} = \frac{e}{4\pi\epsilon_0} \sum_{i,I} \frac{Z_I}{|\vec{r}_i - \vec{R}_I|} \quad (2.4.7)$$

However, solving equation 2.4.1 in practice is rather difficult, as this equation has $3(n + N)$ variables. To reduce the complexity of the problem the Born–Oppenheimer approximation[86] can be applied. Due to the large mass difference of electrons and nuclei, equation 2.4.1 can be separated into two separate equations, one for each type of particle. To do this the wave function $\Psi(\vec{r}, \vec{R})$ is written as the product of an electronic wave function $\psi(\vec{r}, \vec{R})$ and a wave function for the nuclei $\Phi(\vec{R})$

$$\Psi(\vec{r}, \vec{R}) = \psi(\vec{r}, \vec{R})\Phi(\vec{R}) \quad (2.4.8)$$

The large mass difference of electrons and nuclei means that nuclei are accelerated significantly less than the electrons from coulomb interactions. Therefore, from the perspective of electrons, the nuclei can be considered as static. Hence, an electronic Schrödinger equation can be formulated:

$$\hat{H}_e\psi(\vec{r}, \vec{R}) = E_h\psi(\vec{r}, \vec{R}) \quad (2.4.9)$$

The electronic Hamiltonian $\hat{H}_e = \hat{H}(\hat{T}_N = 0)$ and the electronic wave ψ function, and therefore the electronic Energy E_h , are still dependent on the nuclei coordinates \vec{R} . However, due to the quasi-static nature of the nuclei coordinates, \vec{R} are now parameters. The electronic Schrödinger equation has therefore only $3n$ variables.

2.4.2 Geometry Optimization and the Hellmann-Feynman Theorem

In order to get the total energy U_0 , the nuclear kinetic operator cannot be neglected. Within the Born–Oppenheimer approximation this is done by a second Schrödinger equation that includes nuclear movements. The nuclear Schrödinger equation is of course affected by the eigenstates of the electrons.

$$(\hat{T}_N + E_h(\vec{R}))\Phi(\vec{R}) = U_0\Phi(\vec{R}) \quad (2.4.10)$$

The two interdependent equations 2.4.9 and 2.4.10 can now be solved successively and iteratively until a convergence criterion is met. This, however, requires updating the nuclear coordinates with each iteration step according to the results of the previous iteration step. An obvious way to achieve this is to move each nucleus in the direction of the force vector \vec{F} acting upon that atom, where the distance traveled between each iteration is scaled by the norm of the force vector. The force on an atom as a spatial derivative of the total energy can be calculated by the use of the Hellmann-Feynman Theorem[87]:

$$\vec{F} = \frac{\partial U_0}{\partial \vec{R}} = \langle \Phi | \frac{\partial \hat{H}}{\partial \vec{R}} | \Phi \rangle \quad (2.4.11)$$

2.4.3 Density Functional Theory and the Kohn-Sham Equation

For systems with a large number of electrons N , the wave function $\psi(\vec{r}_1, \vec{r}_2, \dots, \vec{r}_N)$ is too complex to solve directly. An approach to further simplify the problem is Density Functional Theory [83, 84], which is an advancement of the Thomas-Fermi model[88]. Rather than calculating the interaction of each electron with all other electrons, only the interaction with the spatial charge density $\rho_e(\vec{r})$ is calculated. The basic principle of DFT is, that instead of solving one wave function for N electrons, the problem is simplified to N wave functions ϕ_i for each individual electron. The resulting single electron Schrödinger equations are called the Kohn-Sham equations[84]. Each electron is moving in the potential generated by the external potential (nuclei) and the potential generated by the $N - 1$ other electrons.

$$\rho_e(\vec{r}) = \sum_i^N |\phi_i(\vec{r})|^2 \quad (2.4.12)$$

This charge density is titular to DFT. The resulting potential \hat{V}_{Ha} from the charge density is therefore:

$$\hat{V}_{Ha} = \int \frac{\rho_e(\vec{r}')}{|\vec{r} - \vec{r}'|} d^3\vec{r}' \quad (2.4.13)$$

However, the decomposition of the wave function $\psi(\vec{r}_1, \vec{r}_2, \dots, \vec{r}_N)$ into single electron wave functions ϕ_i causes a loss of information. The wave function $\psi(\vec{r}_1, \vec{r}_1, \dots, \vec{r}_N)$ must be antisymmetric under exchange of particles due to the fermionic nature of electrons. For the example of a two electron wave function this means:

$$\psi(\vec{r}_1, \vec{r}_2) = -\psi(\vec{r}_2, \vec{r}_1) \quad (2.4.14)$$

This property is lost during decomposition of the wave function in the DFT approach, as the single electron wave functions ϕ_i are independent of each other. To solve this problem, an additional term is added to the Hamiltonian of the Kohn-Sham equations to account for electron exchange, the so-called exchange potential \hat{V}_x . Screening of the Coulomb interaction as the result of the collective behavior of electrons is also lost during the decomposition of the wave function in DFT. The correlation potential \hat{V}_c is added to the Hamiltonian of the Kohn-Sham equations to account for this systematic error. However, no exact analytical expression of this potential is known. The exchange and correlation potential are usually combined into a single exchange-correlation potential \hat{V}_{xc} . Therefore, the Kohn-Sham equations are:

$$\left(\frac{\hbar^2}{2m_e} \nabla^2 + \frac{e^2}{4\pi\epsilon_0} \int \frac{\rho_e(\vec{r}')}{|\vec{r} - \vec{r}'|} d\vec{r}' + \hat{V}_{eN}(\vec{r}) + \hat{V}_{xc}(\vec{r}) \right) \phi_i = u_i \phi_i \quad (2.4.15)$$

Since the exact exchange-correlation potential \hat{V}_{xc} is not known, several models exist. If \hat{V}_{xc} is only dependent on the value of $\rho_e(\vec{r})$ then the approximation is a local density approximation (LDA). If \hat{V}_{xc} is also a function of $\partial\rho_e(\vec{r})/\partial\vec{r}$, it is called a generalized gradient approximation (GGA)[89, 90, 91]. A commonly used GGA functional is the Perdew-Burke-Ernzerhof (PBE) functional[92]. Some so-called hybrid functionals also include Hartree-Fock exchange[93, 94]. In this work, only the LDA parametrizations of Perdew-Zunger-Ceperley-Alder (PZ-LDA)[95, 96] and Perdew-Wang (PW-LDA)[97] are used.

The Kohn-Sham equations are solved iteratively. This means the equation is solved successively for all electrons contained in the charge density $\rho_e(\vec{r})$, which completes one iteration cycle. At the start of each cycle, a new charge density is calculated from the wave functions ϕ_i of the previous cycle. This is repeated until the wave functions generate a potential whose solution results in the wave functions that created it. This iteration is therefore called the self-consistent-field (SCF) cycle. The resulting eigenvalues u_i and wave functions are not necessarily physical meaningful but are often used as an approximation. However, the resulting (ground state) charge density is both physical and unique to the causative external potential due to the Hohenberg-Kohn-Theorems[83]. Since the exact exchange-correlation potential is not known, the ground state energy is subject to a degree of uncertainty dependent on the used approximation.

2.4.4 Basis Sets

At this point, it is appropriate to take a closer look at the wave functions ϕ_i . Until this point, wave functions were treated as if the correct ground state wave functions of each potential was taken for granted, which of course is not the case. The Hohenberg-Kohn-Theorems[83] state that the energy functional is minimized if the energy density is the ground state density and therefore, the wave function is the ground state wave function. This can be expressed by the Ritz variational principle[98] on which the Hohenberg-Kohn-Theorems are based upon:

$$u_{i0} \leq \frac{\langle \phi_n | \hat{H} | \phi_n \rangle}{\langle \phi_n | \phi_n \rangle} \quad (2.4.16)$$

where u_{i0} is the ground state eigenvalue and ϕ_n are some test functions (= basis set). It is possible to exploit the fact that ϕ_n span a Hilbert space[99, 100], which means the ground state eigenfunction ϕ_{i0} can be constructed by a linear combination of the test functions:

$$\phi_{i0} = \sum_n s_n \phi_n \quad (2.4.17)$$

By trying to find a set of parameters s for which the right-hand side of equation 2.4.16 becomes minimal, one can find a good approximation of the ground state. In practice, only a partial set of test functions is used instead of the whole Hilbert space. Usually, this is done

by a user-defined energy cutoff, where only functions with a smaller energy are included. The influence of the energy cutoff on the results is discussed in section 5.1. Choosing an appropriate set of basis functions can speed up the calculations significantly. While many more exist, two appropriate sets shall be named here explicitly.

(1) Hydrogen like orbitals or more specifically numerically tabulated atom-centered orbitals of the type:

$$\phi_n = \frac{f_n(r)}{r} Y_{lm} \quad (2.4.18)$$

where $f_n(r)$ is a Gaussian-type or Slater-type radial function and Y_{lm} are spherical harmonics. An obvious advantage of this approach is, that orbitals of non-valence electrons are often hydrogen-like. This approach is used in the DFT code FHI-AIMS (see section 3.1.2) and is described in more detail in Blum et al.[101]

(2) Bloch type plane waves are often used as a basis set when performing DFT calculations of infinite periodic structures, e. g. crystals. These wave functions consist of a periodic part $f_n(r)$ and a plane wave-like part:

$$\phi_n = f_n(r) e^{i\vec{k}r} \quad (2.4.19)$$

where \vec{k} is the wave vector. These wave functions have the same periodicity as the lattice. Due to the Bloch theorem[102], any integral over an infinite periodic space can be calculated as an integral within the 1. Brillouin zone of reciprocal space. The latter can furthermore be approximated as a sum over a sufficiently dense, but finite grid of points (k-points) within the 1. Brillouin zone. The influence of the density of the k-point grid on the results is discussed in section 5.1. This method is used by the DFT code ABINIT(see section 3.1.1). The linear combination of test functions solving the energy functional creates a system of linear equations which can be solved in practice with conjugate gradient methods[103, 104].

2.4.5 Pseudopotentials and LAPW and PAW

A further reduction of the required computational effort can be achieved by treating valence electrons and non-valence (= core) electrons differently. Three methods to do so shall be discussed here:

(1) The Pseudopotential (PP) approach[105, 106, 107] separates the potential of the nucleus and the core electrons into a single effective potential, which is seen by the valence electrons. Outside of the so-called cutoff radius r_c the effective potential is identical to the real all-electron potential. However, within r_c the potentials and therefore the wave functions diverge. This approach has several advantages. Besides reducing the number of electrons, and therefore the number of Kohn-Sham equations which need to be solved, it also reduces

the size of the basis set. The reason for this is that electrons close to the nuclei have a high kinetic energy and therefore a short wavelength. This, in turn, requires a basis set which is capable to resolve these high frequencies. By including these electrons in an effective potential the value of the energy cutoff and therefore the number of basis functions can be reduced. The downside of this approach is a further dependency of the results on the choice of PP as well as a reduced transferability, meaning PPs created for a specific case may not be transferable to another case.

(2) The linearized augmented plane wave (LAPW) method[108] addresses the problem, that orthogonalized plane waves near the atomic nuclei require a large number of (high frequency) basis set functions in order to sufficiently describe the wave function. Instead, the simulation area is separated into two regions. Atomic spheres of radius r_c in which spherical harmonics Y are used to describe the wave function close to the nuclei and an external region, in which wave functions are treated as plane waves. Unlike the pseudopotential approach, the LAPW method is an all-electron method.

(3) The projector augmented wave (PAW) method[109] attempts to combine the Pseudopotential approach and the LAPW method. It augments the wave function ϕ within a spherical augmentation region around each atom to avoid the computational expensive rapid oscillations near the ion cores. This is done by linear transformation of the Kohn-Sham single-particle wave function of a valence electron into a well behaved fictitious pseudo wave function. The inner electrons can be treated with the frozen core approximation similar to the pseudopotential approach.

2.4.6 Phonons and Perturbation Theory and Berry-Phase

DFT, as described so far, allows for the calculation of the structure and total energy of a crystal or molecule. However, it is possible to calculate various material properties with first principle calculations as well. These material properties include among others the elastic tensors, dielectric properties, polarization, piezoelectric constants and phonon spectra. These properties can often be described as a first or second order derivative of the total energy.

Force:

$$F_i = -\frac{\partial U_0}{\partial R_i} \quad (2.4.20)$$

Dielectric displacement / Polarization:

$$P_i = \frac{\partial U_0}{\partial E_i} \quad (2.4.21)$$

Dielectric susceptibility:

$$\chi_{jk} = -\frac{\partial^2 U_0}{\partial E_j \partial E_k} \quad (2.4.22)$$

Elastic tensor:

$$K_{ijkl} = \frac{\partial^2 U_0}{\partial \tau_{ij} \partial \tau_{kl}} \quad (2.4.23)$$

Piezoelectric tensor:

$$e_{ikl} = -\frac{\partial^2 U_0}{\partial E_i \partial \tau_{kl}} \quad (2.4.24)$$

The Phonon frequencies ω can be obtained by solving the secular equation[110]:

$$\det\left|\frac{1}{\sqrt{M_l M_m}}\tilde{C}_{lm}^{\alpha\beta}(\vec{q}) - \omega^2(\vec{q})\right| = 0 \quad (2.4.25)$$

where \vec{q} is the (phonon-) wave vector and $\tilde{C}_{lm}^{\alpha\beta}(\vec{q})$ is the Fourier transform of the matrix of the inter-atomic force constants $C_{lm}^{\alpha\beta}(\vec{R})$

$$C_{lm}^{\alpha\beta}(\vec{R}) = \frac{\partial^2 U_0}{\partial R_l^\alpha \partial R_m^\beta} \quad (2.4.26)$$

The Greek superscripts indicate Cartesian components. With the knowledge of the phonon modes, the thermal contribution to the free energy can be calculated by summation over all phonon modes and the Brillouin zone[110]:

$$F_{Ph} = -k_B T \sum_{i,k} \log\left(2 \sinh \frac{\hbar \omega_{i,k}}{2k_B T}\right) \quad (2.4.27)$$

The calculation of these perturbations requires some extensions to DFT, namely the density functional perturbation theory (DFPT) for the strain and spatial perturbations and Berry-phase calculations for the electric field perturbations. The details of these two methods are beyond the scope of this work, but a brief explanation of these methods is given below.

Density functional perturbation theory is a method to calculate the influence of small perturbations such as atom displacements, strain, or electric fields at zero electric field strength on the energy of the system in an equilibrium state. The two main methods are from Baroni[111] and Gonze[112] and allow for the computation of energy derivatives and phonons at arbitrary wave vectors.

The treatment of finite electrical fields introduces a non-periodic term into the potential energy landscape. This conflicts with the periodic boundary conditions used in the treatment of crystals. Furthermore, the infinite large crystal simulated by the periodic boundary conditions allows an electron to minimize its own energy by tunneling from the valence band into the conduction band since the slope in the potential due to the electric field guarantees that the conduction band drops below the valence band over sufficient length scales. Therefore, there is no well-defined ground state for the DFT algorithm to find. This problem can be solved by the introduction of a so-called **Berry-phase**[113, 114, 115], which allows for the calculation of the polarization and the energy within a finite electric field.

3 Methods

3.1 Tools

3.1.1 ABINIT

ABINIT is a freeware open source package for DFT calculations managed by the ABINIT Group under a general public license [116, 117, 118]. It is able to perform structural relaxation, molecular dynamics and perturbation theory calculations based on a DFT approach. The program uses plane wave basis sets for valence electrons. It is therefore particularly suited to handle periodic structures such as crystals, but the calculation of non-periodic structures such as molecules, surfaces, or interfaces is also possible if necessary by using appropriately sized simulation domains with a vacuum. Pseudopotentials or PAW atomic data files are used for handling core region electrons. This approach reduces calculation times but introduces uncertainties as the results are dependent on the used pseudopotential or PAW atomic data file. Validation with an all-electron code like FHI-AIMS (see section 3.1.2) is therefore advisable. ABINIT implements by default a locally optimal block preconditioned conjugate gradient (LOBPCG) solver by Knyazev for the SCF-cycle [104]. The solver for structural relaxation or molecular dynamics is selectable by the user. ABINIT also offers a large library of exchange- and correlation-potentials to choose from. Most calculations can be distributed on multiple processors for parallel computing[119]. The ABINIT package includes a variety of post-processing tools such as ANADDB, AIM, or CUT3D as well[120, 121].

3.1.2 FHI-AIMS

FHI-AIMS[101] is a full-potential, all-electron ab initio code developed by the Fritz-Haber-Institut of the Max-Planck-Gesellschaft, Berlin. Its functionality includes structure optimization, ab initio molecular dynamics, perturbation theory calculations and molecular transport calculations for both periodic and non-periodic structures. Unlike ABINIT, the full set of electrons are simulated using atom-centered numeric basis functions. While this approach is much more time consuming, it is also independent of pseudopotentials or PAW atomic data files. As such, FHI-AIMS is well suited to validate the ABINIT results. Like ABINIT, FHI-AIMS offers a set of exchange- and correlation-potentials to choose from and is capable of parallel computing.

3.2 Computational Methods

3.2.1 Self Consistent Cycle and Structural Relaxation

The PAW implementation [122] of ABINIT is used in this work with PAW atomic data sets from the GBRV library[123, 124]. The energy cutoff is set to 18 Ha and the PAW energy cutoff for the double grid is set to 22 Ha by default if not otherwise stated. The LDA Perdew-Zunger-Ceperley-Alder parametrization [95, 96] for the exchange-correlation is used in all calculations as defined by the PAW atomic data sets. During the SCF-cycle the error vector is calculated by Pulay mixing [125, 126] based upon the 7 previous iterations of the SCF-cycle. The exit condition of the SCF-cycle is based on the differences of interatomic forces between individual iterations of the cycle and set to a value of 1×10^{-6} Ha/ a_0 . As the c-phase only has one degree of freedom, this exit condition of the SCF-cycle is inappropriate. Instead, an exit condition based upon the differences in the potential residual between individual iterations of the cycle is used and set to 1×10^{-15} . For structural optimization, the Broyden-Fletcher-Goldfarb-Shanno minimization method [127, 128, 129, 130] is used with a force based exit condition of 1×10^{-5} Ha/ a_0 . Lattice parameters are allowed to relax freely. The Brillouin zone is sampled with a Monkhorst-Pack[131] k-Point grid of $4 \times 4 \times 4$ divided by the number of 12-atomic standard cells in each corresponding direction. A set of self-made pseudopotentials (SM-PP) were used in the author’s 2015 publication Materlik et al.[50]. Some of these calculations will be presented here for comparison. An energy cut of 30 Ha was used in combination with a $6 \times 6 \times 6$ k-point grid. The exit criteria were identical to those used for the GBRV library.

For validation of the ABINIT results, several calculations were repeated with FHI-AIMS using numerical basis functions with “tight” settings and first and second tier basis functions enabled. For the exchange-correlation the LDA Perdew-Wang parametrization [97] is used with stopping criteria for the electronic convergence of 1×10^{-4} eV/Å and 1×10^{-3} eV/Å for the structural convergence. The Brillouin zone is sampled with a $6 \times 6 \times 6$ Monkhorst-Pack grid divided by the number of 12-atomic standard cells in each corresponding direction.

3.2.2 Total Energy Derivatives

The ABINIT code offers the ability to calculate the spatial derivatives of the total energy[120, 121]. From these derivatives, properties like elastic modulus, piezoelectric tensors, dielectric constants and phonon mode frequencies can be calculated. Fully relaxed 12 atomic cells of HfO₂ and ZrO₂ were used for the m-, f-, f’-, t-, and c-phase. For the o-phase, 24 atomic unit cells were used. The calculations were performed with a $2 \times 2 \times 2$ q-point grid. To ensure accurate results, the wave functions of the relaxed structures were recalculated with a stricter

exit criterion with a value of 1×10^{-20} for the residual potential. The results were analyzed with the MRGDDB and ANADDB tools included within the ABINIT package. The acoustic sum rule is enforced. For the integration of the thermodynamic functions, the q-point grid is interpolated to a $30 \times 30 \times 30$ Monkhorst-Pack grid. The results are analyzed for phonon frequencies, entropy, dielectric matrix, piezoelectric matrix and stiffness matrix.

3.2.3 Stress and Strain Calculation

Stress calculations[132] are performed with uni-axial, bi-axial, and hydrostatic stress conditions. The stress targets ranged from -5 GPa to 5 GPa in intervals of 1 GPa. 12 atomic cells of HfO_2 , $\text{Hf}_{0.5}\text{Zr}_{0.5}\text{O}_2$, and ZrO_2 were used for the m-, f-, f'-, t-, and c-phase. For the o-phase, 24 atomic unit cells were used with the same stoichiometries. Uni-axial stress was applied in the $[100]$, $[010]$, and $[001]$ directions, bi-axial stress was applied to the (100) , (010) , and (001) lattice plains. Lattice parameters and ion positions were fully relaxed under the aforementioned stress conditions. The results are analyzed both in terms of stress and strain.

3.2.4 Electric Fields and Polarization

Berry phase electric field calculations were performed with undoped structures of HfO_2 and ZrO_2 . The electric perturbations were applied to all three dimensions. The cell size was 12 atoms for the investigated phases. Ionic positions and lattice constants were relaxed freely. The results were analyzed in terms of polarization and dielectric tensor.

3.3 Defect Types and Defect Structure Generation

Defect structures are generated by either removing, adding, or replacing one or more atoms within an otherwise pure (super-)cell. This results in either vacancy, interstitial, or substitutional defects. A combination of two or more of these defects is possible. Dopants are considered to substitute hafnium or zirconium within this work if not otherwise stated. They might be accompanied by an oxygen vacancy.

3.3.1 Defect Types and Defect Reactions of Charge Neutral Defects

Due to the ionic character of $\text{Hf}_{1-x}\text{Zr}_x\text{O}_2$, removing, adding, or replacing one or more ions can alter the charge of the supercell. In order to maintain a charge neutral simulation area, it may be necessary to introduce one or more electrons or holes depending on the type and placement of the defect. This section will explain the different types of defects in the example HfO_2 . Defects in ZrO_2 are completely analog to the examples presented here. In the case of II-valent dopants, the following hafnium substituting dopant defect structures are considered. The $\text{M}(\text{II})_{\text{Hf}}$ defect with the Kröger-Vink defect reaction:

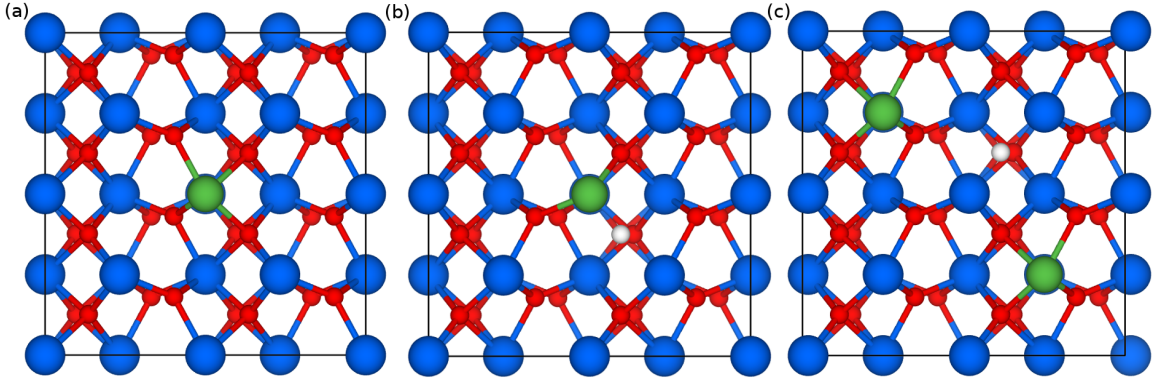
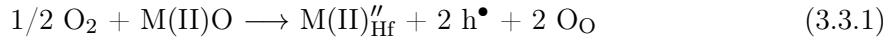
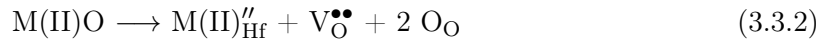


FIG. 3.1: (a) M_{Hf} , (b) $M_{\text{Hf}}V_{\text{O}}$ and (c) $(2M_{\text{Hf}})V_{\text{O}}$ defects. Blue: Hf, red: O, green: dopant M, white: vacancy

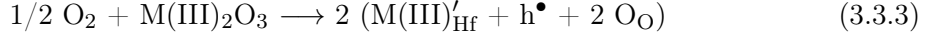


In the Kröger-Vink notation, positive charges are indicated by the " \bullet "-symbol, negative charges by the "'-symbol. Since the II-valent dopant is replacing IV-valent hafnium, 2 holes are needed in order to charge compensate for the additional oxygen in the vicinity of the dopant. Therefore, the M(II)_{Hf} defect is an electronically compensated defect. Since there is only one Wyckoff position for hafnium in all investigated space groups, all possible dopant positions are symmetrically equivalent. Therefore only one calculation needs to be performed per dopant species for this defect structure. This is true for all valences of dopants. Calculations are performed with 96- and 48-atomic (super-) cells. It is assumed, that the defect to defect interaction across the boundaries of the (super-) cells is negligible. This assumption is made for all charge neutral defects. An example of a M_{Hf} structure can also be found in Figure 3.1 (a). Charge compensation can also be achieved by introducing an oxygen vacancy instead of the holes. This leads to the $\text{M(II)}_{\text{Hf}}V_{\text{O}}$ defect with the Kröger-Vink defect reaction:



Since charge compensation is achieved by the removal of one oxygen-ion this defect is ionically compensated. The opposite charge of dopant and vacancy leads to an attractive force. The vacancy is therefore placed directly next to the dopant atom. As there are eight neighboring oxygen ions to each hafnium, eight possible structures for this defect are considered. Due to symmetry, this number can be reduced to two or one for the t-and c-phase respectively. Calculations are performed with 96- and 48-atomic (super-) cells. An example of a $M_{\text{Hf}}V_{\text{O}}$ structure can also be found in Figure 3.1 (b). The list of II-valent dopants considered in this work is Be, Mg, Ca, Sr, and Ba. The defect generation of III-

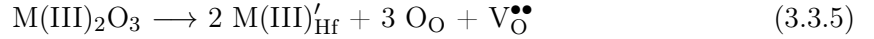
valent dopants is more complicated, due to the uneven amount of electrons. This leads to three types of hafnium substituting dopant defect structures. The electronically compensated defect $M(\text{III})_{\text{Hf}}$ is similar to the $M(\text{II})_{\text{Hf}}$ defect.



As can be seen in the Kröger-Vink defect reaction only one electron-hole is required. Calculations are performed with 96-, 48-, and 24-atomic (super-) cells. The $M(\text{III})_{\text{Hf}}V_\text{O}$ defect is different from the $M(\text{II})_{\text{Hf}}V_\text{O}$ defect as it requires one additional electron together with the oxygen vacancy to be charge neutral. The defect is therefore referred to as mixed compensated.



Like in the $M(\text{II})_{\text{Hf}}V_\text{O}$ the eight neighboring oxygen ions are investigated as positions for the vacancy. Calculations are performed with 96-, 48-, and 24-atomic (super-) cells. The ionically compensated defect $(2M(\text{III})_{\text{Hf}})V_\text{O}$ pairs two dopant ions with one oxygen vacancy. It can be written with the Kröger-Vink defect reaction:



In a 96-atomic supercell of HfO_2 , there are $1 \times 31 \times 64 = 1984$ possible combinations to place two dopant atoms and one vacancy. However, this number can be cut in half or less due to symmetry, leading to up to 992 structurally nonequivalent structures of this defect. The exact number depends on the space group of the supercell. This reduced number of necessary calculations still exceeds the computational budget of this work. Therefore a reduced set of structures based on the works of Parkes et al. [133, 134] was calculated. Due to the high degree of symmetry Parkes et al. were able to calculate the energetically most favorable positions of one and two $(2Y_{\text{Hf}})V_\text{O}$ defects within one 96-atomic supercell of cubic ZrO_2 . These defect positions can be mapped to positions within the other space groups. The ambiguity in mapping the lattice constants of the c-phase to the lattice constants of the other space groups leads to up to six structural nonequivalent defect structures. Atomic positions of these structures can be found in the Appendix A in the tables 6.8 and 6.9. An example of a $(2M_{\text{Hf}})V_\text{O}$ structure can also be found in Figure 3.1 (c).

The list of III-valent dopants considered in this work includes Al, Y, and La. The introduction of electrons or holes in electronically or mixed compensated defects necessitates an adaption of the Fermi level. IV-valent dopant defects structures require no charge compensation when the dopant is substituting for hafnium.

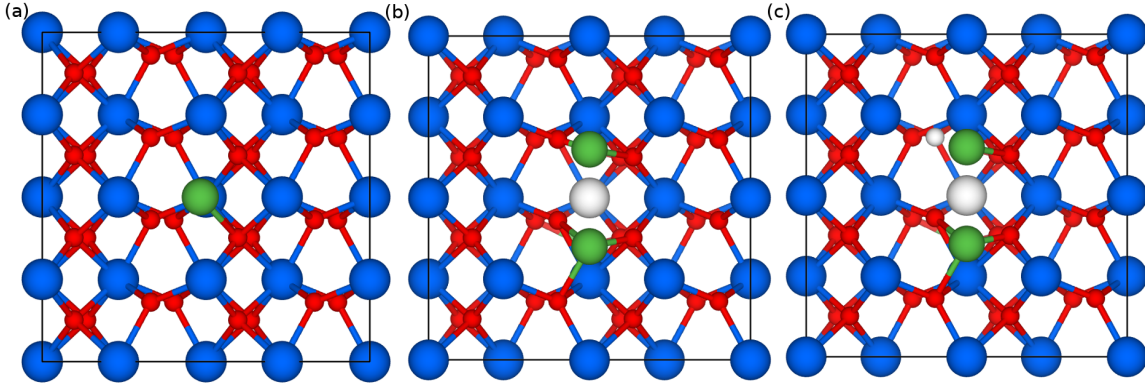
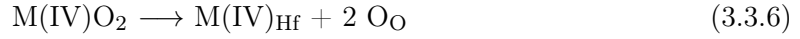


FIG. 3.2: (a) Al_I , (b) $(2Al_I)V_{Hf}$ and (c) $(2Al_I)V_{Hf}V_O$ defects. Blue: Hf, red: O, green: dopant M, white: vacancy



Therefore the mixture of hafnium and zirconium in the form of $Hf_{1-x}Zr_xO_2$ does not require any form of charge compensation. Calculations for $Hf_{0.5}Zr_{0.5}O_2$ are performed with 12- or 24- atomic cells. There are two kinds of vacancies in HfO_2 . The oxygen vacancy with the Kröger-Vink defect reaction:



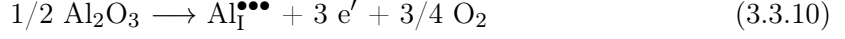
As there are two Wyckoff positions for oxygen in the m-, o-, f'-, and f-phase two nonequivalent oxygen vacancies exist. In the t- and c-phase, only one Wyckoff position and therefore oxygen vacancy exists. Calculations are performed with 96- and 48-atomic super-cells. There is also the possibility of a hafnium vacancy with the Kröger-Vink defect reaction



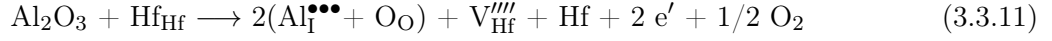
The single Wyckoff position for hafnium in all space groups necessitates the calculation of only one defect structure as all hafnium positions are structurally equivalent. Calculations are performed with 96- and 48-atomic super-cells. Within this work, two kinds of interstitial defects are considered, dopant interstitials and oxygen interstitials. For the sake of simplicity, the source of the interstitial oxygen is assumed to be external rather than an oxygen from a lattice site. Therefore, the Kröger-Vink defect reaction is:



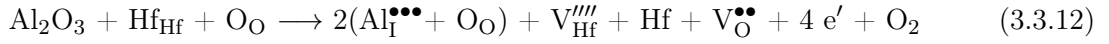
Three different types of aluminum interstitials were examined. A single aluminum on an interstitial site Al_I :



Both defects with a single interstitial atom are calculated in 96-atomic super-cells. Positions of the interstitials are listed in Appendix A in section 6. Figure 3.2 (a) depicts Al_I defect as an example. The second investigated aluminum interstitial defect includes two aluminum atoms placed in the vicinity of a hafnium vacancy $(2\text{Al}_\text{I})\text{V}_\text{Hf}$:

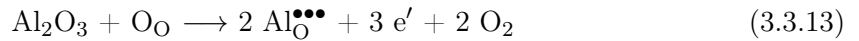


The third investigated interstitial aluminum defect is identical to the previous one with the addition of an oxygen vacancy:



The placement of the hafnium vacancy and the two aluminum interstitials is identical in both the second and third interstitial defect. Both interstitials are placed on the hafnium vacancy site but moved upwards and downwards along the z-axis to avoid overlapping. All oxygen atoms neighboring either of the interstitials are considered for the placement of the oxygen vacancy in the $(2\text{Al}_\text{I})\text{V}_\text{Hf}\text{V}_\text{O}$ defect structure. Positions of both defects are listed in the Appendix A in section 6. The defect structures are depicted in figure 3.2 (b) and (c) respectively.

Aluminum was also considered as a substitutional dopant for oxygen due to its small size in comparison with hafnium. The Kröger-Vink defect reaction of the Al_O defect is:



As there are two Wyckoff positions for oxygen in the m-, o-, f¹-, and f-phase two nonequivalent oxygen vacancies exist. In the t-and c-phase there is only one Wyckoff position, and therefore only one oxygen vacancy exists. Calculations are performed with 96- and 48-atomic super-cells.

In order to compare the results of these different defect structures with each other, a uniform definition of defect or dopant concentration is needed. When not otherwise stated, all defect concentrations in this work are given in f.u. % which is defined in the following way:

for cations:

$$\text{f.u.}\% = \frac{\text{number of defect cations} \times 100 \%}{\text{number of HfO}_2 \text{ formula units in defect free cell}} \quad (3.3.14)$$

Substitutional dopants, interstitial dopants and Hf vacancies each count towards the number of defect cations with a value of 1. In cases like the $(2Al_I)V_{Hf}$ defect, where there are both interstitial dopants and Hf vacancies, one interstitial dopant is combined with one Hf vacancy and count together with a value of 1, since this arrangement is similar to one substitutional dopant. Since the formula unit of $Hf_{1-x}Zr_xO_2$ only has one cation, this definition is identical to cat % in most cases.

for anions:

$$\text{f.u.\%} = \frac{\text{number of defect anions} \times 100 \text{ \%}}{\text{number of } HfO_2 \text{ formula units in defect free cell}} \quad (3.3.15)$$

The rules for counting the number of defect anions are identical to the rules for counting the number of defect cations. However, since the formula unit of $Hf_{1-x}Zr_xO_2$ has two anions, this definition is identical to $2 \times \text{ani \%}$ (ani = anion). In defect structures where there are both defect anions and cations, only the higher value counts, as anion and cation defects are thought to be coupled.

3.3.2 Formation Energy and Charged Defects

The formation energy E_f is the energy required to create a defect X within a crystal lattice. It is calculated as:

$$E_f(X, q) = U_0(X, q) - U_0(\text{pure}) - \sum_i m_i \mu_i + q(\epsilon_F + \epsilon_{VB}(\text{pure}) + \Delta V(X, 0)) + E_{Corr}(X, q) \quad (3.3.16)$$

$U_0(X, q)$ is the total energy of a structure with defect, $U_0(\text{pure})$ the total energy of the same structure without defect. μ_i is the chemical potential of a species of atom that is either removed or added from the lattice during the creation of the defect, m_i is the corresponding number of atoms of that species. Positive numbers for m_i indicate that atoms are added, negative numbers that atoms are removed. For charged defects with charge q that are not locally compensated other ions, electrons or holes the Fermi energy ϵ_F in respect to the valence band edge ϵ_{VB} needs to be added. For correct alignment with the band structure, an offset ΔV may be necessary.

In order to account for the long-range self-interaction E_{MP} of defects across the periodicity of the (super)cell, a correction term E_{Corr} may be added to equation 3.3.16. This term can be determined by fitting the total energies of 96- and 324-atomic supercells with a Makov-Payne scaling law[135] and extrapolating to infinity:

$$E_{MP} = \frac{a_{MP}}{L} + c_{MP} \quad (3.3.17)$$

$$E_{Corr} = E_{MP}(\infty) - E_{MP}(L_0) = -\frac{a_{MP}}{L_0} \quad (3.3.18)$$

a_{MP} and c_{MP} are fit parameters and L is the size of the supercell. However, due to the large expenditure in calculation time necessary to calculate a 324-atomic supercell, this term is set to zero within this work if not otherwise stated.

The ab initio calculation of charged dopants within supercells with ABINIT requires the specification of the desired charge, otherwise, a charge neutral calculation is performed. However, the electrostatic potential and the total energy are ill-defined within periodic boundary conditions[136]. Therefore it is necessary to introduce a background charge. Within this work, this is done by setting the average of the smooth electrostatic potential to zero.

The formation energies required for equation 3.3.16 are calculated from ab initio. The chemical potential of Hf is calculated from a two atomic hexagonal close-packed (hcp) unit cell of metallic Hf.

$$\mu_{\text{Hf}} = \frac{U_0(\text{hcp-Hf})}{2} \quad (3.3.19)$$

For the dopant atoms, the chemical potential μ_i is calculated from the thermodynamic most stable oxide using the chemical potential of oxygen μ_{O} . Therefore, for II- and III-valent dopants the chemical potential μ_{M} is:

$$\mu_{\text{M(II)}} = U_0(\text{M(II)}) - \mu_{\text{O}} \quad (3.3.20)$$

$$\mu_{\text{M(III)}} = \frac{U_0(\text{M(III)}) - 3\mu_{\text{O}}}{2} \quad (3.3.21)$$

The chemical potential of oxygen is treated as a variable within this work and is varied from an oxygen-poor condition to an oxygen-rich condition. The oxygen-rich chemical potential is simply calculated from the oxygen molecule.

$$\mu_{\text{O}_r} = \frac{U_0(\text{O}_2)}{2} \quad (3.3.22)$$

HfO₂ thin films are often grown on Si or a metal electrode. Both substrates may compete with Hf for oxygen. The value for the chemical potential in the oxygen-poor condition is therefore set to the value, where the bulk substrate precipitates into its own oxide [137]. This was done for both Si and Ti, however, both materials returned similar values for the chemical potential of oxygen. The value from anatase-TiO₂ is used in the rest of this work for the oxygen-poor chemical potential.

$$\mu_{\text{O}_p} = \frac{U_0(\text{anatase-TiO}_2) - \mu_{\text{Ti}}}{2} \quad (3.3.23)$$

The chemical potential is calculated from hcp-Ti in the same way as for Hf. Since the formation energy is a linear function of the chemical potential, the formation energy can be linearly interpolated from the oxygen-rich and poor values.

4 Grain size and Surface / Interface Energy Model

The ferroelectric properties of undoped $\text{Hf}_{1-x}\text{Zr}_x\text{O}_2$ show a thickness dependence [76, 77], as previously discussed in chapter 2.3.4. This can be attributed to the poly-crystalline nature [138] of the ferroelectric films in combination with a surface or interface effect. These surfaces/interfaces have corresponding surface/interface energies, that can stabilize phases other than the ground state phase. This effect has previously been observed in a monoclinic to tetragonal phases transition in ZrO_2 [80]. In the following sections, models will be developed that attempt to reproduce the experimental thickness and stoichiometry dependence of ferroelectricity in undoped $\text{Hf}_{1-x}\text{Zr}_x\text{O}_2$ thin films. This is done by using the DFT results to describe the bulk of the grains in the polycrystalline material and a thermodynamic description of the surface/interface energy with phenomenological model parameters. The associated values of the specific surface/interface energies are model parameters that are used to fit the model to experimental data. In section 4.1 a surface energy model is described, which is based on the formerly published model by the author in 2015 in the Journal of Applied Physics [50]. In section 4.2 this model is further refined into an interface energy model due to new experimental data available at the time. This interface model was published in 2017 in the Journal of Applied Physics [51]. This publication further improved upon the model by introducing a grain size distribution model, which will be briefly discussed in section 4.3. This combined model is the product of close cooperation between the author and his coworker Christopher Künne, who should be explicitly credited for his work on the grain size distribution model.

4.1 Surface Energy Model

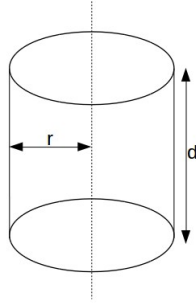


FIG. 4.1: Model of a grain with grain radius r_G and grain thickness d_G . The grain thickness is assumed to be equal to the film thickness.

This surface model assumes cylindrical grains of uniform thickness d_G equal to the film thickness and uniform radius r_G as depicted in figure 4.1. The surface A and volume V of such a grain is:

$$A = 2\pi r_G(r_G + d_G) \quad (4.1.1)$$

$$V = 2\pi d_G r_G^2 \quad (4.1.2)$$

The surface energy $\Gamma_S(\Phi)$ can be interpreted as an interface energy between the grain and its surroundings or vacuum and is therefore calculated as:

$$\Gamma_S(\Phi) = A\gamma_\Phi = 2\pi r_G(r_G + d_G)\gamma_\Phi \quad (4.1.3)$$

where γ_Φ is the value of the specific surface energy of phase Φ ($\Phi \in \text{m-,f-,t-phase}$). This surface energy has to be added to the bulk energy of the grain consisting of N_G formula units $\text{Hf}_{1-x}\text{Zr}_x\text{O}_2$. The entropy contribution has to be taken into account as well. Therefore, the free energy (Helmholtz or Gibbs) present in the grain is:

$$F(\Phi) = N_G(U_0(\Phi) - TS(\Phi)) + \Gamma_S(\Phi) \quad (4.1.4)$$

However, it is more practical to break down this energy to the formula unit, which can be achieved by dividing equation 4.1.4 by N_G . The number of formula units can be calculated from the grain volume, the volume of the unit cell V_0 , and the number of formula units per unit cell, the latter having a value of 4 in the example of the f-phase. Henceforth the unit cell volumes V_{12} of all phases are calculated as 12 atomic cells, regardless of the actual number of atoms in the unit cell.

$$N_G = 4 \frac{V}{V_{12}(f)} = 4 \frac{2\pi d_G r_G^2}{V_{12}(f)} \quad (4.1.5)$$

By inserting equation 4.1.5 and 4.1.3 into equation 4.1.4, the energy stored in the grain broken down to the formula unit can be calculated as:

$$F(\Phi) = U_0(\Phi) - TS(\Phi) + \frac{r_G(r_G + d_G)\gamma_\Phi V_{12}(\Phi)}{4d_G r_G^2} \quad (4.1.6)$$

The values of γ_Φ are model parameters which need to be fitted to experimental data. When determining the stable phase, it is important to account for the conservation of mass, as a given grain consisting of N_G formula units can have different volumes, depending on the phase it forms. This model assumes that in addition to the number of unit cells, the film thickness is conserved as well. This means that grains only vary in grain radius r_G . N_G is determined by a reference grain, with a given aspect ratio r_G/d_G and a given phase (f-phase).

$$r_G(\Phi) = \sqrt{\frac{N_G V_{12}(\Phi)}{8\pi d_G}} = r_G(f) \sqrt{\frac{V_{12}(\Phi)}{V_{12}(f)}} \quad (4.1.7)$$

With this surface energy model, the preferred phase of a grain with a given radius r_G and film thickness d_G can be determined by calculating the free energy for all phases and choosing the phase, for which the free energy F is minimal.

$$\Phi(r_G, x) = \min F(r_G, x, \Phi') \quad (4.1.8)$$

$\Phi' \in \text{m-,f-,t-phase}$

The results of this model were published in 2015 in the Journal of Applied Physics[50].

4.2 Interface Energy Model

The observation of a tetragonal interlayer by Grimley et al.[139] and Pešić et al.[140] at the surface of Gd-doped HfO_2 grains with high-angle annular dark-field scanning transmission electron microscopy (HAADF-STEM) inspired the transition from a surface energy model to a coherent interface energy model. Within this model, the grain consists of a **bulk or core region** in the center and an **interlayer in the outer region**, as is depicted in figure 4.2 (a). The interlayer consists of t-phase $\text{Hf}_{1-x}\text{Zr}_x\text{O}_2$, the core assumes any phase that minimizes the energy of the system. Core and interlayer are separated by a **coherent interface** with an associated interface energy, whose value depends on the phase of the core as well as the interface area. The interlayer also forms an outer **surface** to the surrounding grains or electrodes.

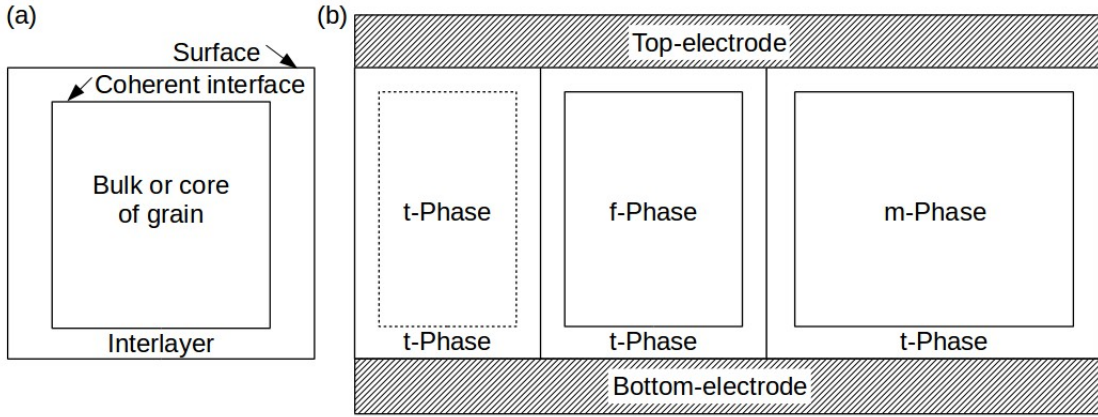


FIG. 4.2: (a) Model of a single grain. (b) Model of multiple grains with a tetragonal interface layer, where the bulk phase is determined by the surface to volume ratio of the interface and the interface energy

The energy present in the grain is calculated from the bulk energy U_0 of the core, the entropy contribution TS , the interface energy between the core and the tetragonal surface layer Γ_I , and a term C_t which summarizes the bulk energy of the tetragonal surface layer and the surface energy of the grain.

$$F = U_0 - TS + \Gamma_I + C_t \quad (4.2.1)$$

Since the interlayer always consists of the tetragonal phase and is also very thin, the term C_t is assumed to be independent of the bulk phase of the grain. As a consequence this term can be neglected in the determination of the stable phase. The interface energy is calculated in a similar fashion to the surface energy:

$$\Gamma_I(\Phi) = \frac{\tilde{r}_G(\tilde{r}_G + \tilde{d}_G)V_{12}(\Phi)}{4\tilde{d}_G\tilde{r}_G^2} \tilde{\gamma}_{\Phi t} \quad (4.2.2)$$

\tilde{r}_G and \tilde{d}_G are the radius and thickness of the grain core. The thickness of the tetragonal interlayer δ is assumed to be uniform over the whole grain with a value of 1 nm. It therefore follows:

$$\tilde{r}_G = r_G - \delta \text{ and } \tilde{d}_G = d_G - 2\delta \quad (4.2.3)$$

The values of the interface energies $\tilde{\gamma}_{\Phi t}$ are fit parameters but can be approximated from the surface energies of Materlik et al.[50] as:

$$\tilde{\gamma}_{\Phi t} = \gamma_{\Phi} - \gamma_t \quad (4.2.4)$$

Therefore, the value of $\tilde{\gamma}_{tt}$ is set to 0, which can also be understood as a perfectly coherent interface between the tetragonal interlayer and bulk. Values for the total energy, specific interface energy, cell volume are linearly interpolated between HfO_2 and ZrO_2 .

While this model is inspired by the experimental observations of Grimley et al.[139] and Pešić et al.[140], there are some simplifications and assumptions inherent within the model. Particularly it assumes, that the interlayer surrounds the core in its entirety, while the experimental observations of these interlayers focused on the boundary to the electrodes. Whether these interlayers also exist at the boundary to neighboring grains is not sufficiently known. The possible influence of dopants on these interlayers is also neglected. Both Grimley et al. and Pešić et al. observed the interlayers in Gd-doped HfO_2 .

4.3 Grain Radius Distribution

Experimental observations with X-ray diffraction (XRD)[64, 76, 79, 62] and scanning electron microscopy (SEM)[141, 142, 139, 62] reveal, that $\text{Hf}_{1-x}\text{Zr}_x\text{O}_2$ thin films produced with ALD or CSD are poly-crystalline were the individual grains vary in grain size, grain orientation, and phase. The material properties of such a film are therefore the result of an average of grains with corresponding individual properties weighted by stoichiometry and phase composition. Since the values of the dielectric permittivity and remanent polarization depend on the phase, the film values can be calculated from the volumetric fraction of each phase within the thin film. The volumetric fractions of each phase can be calculated from the interface energy model if the grain radius distribution $f_{\alpha,\beta}(\tilde{r}_G, \tilde{d}_G, x)$ is known.

$$\begin{aligned} \overline{k(\tilde{d}_G, x)} &= \int_0^\infty 2\pi\tilde{r}_G\tilde{d}_G \cdot f_{\alpha,\beta}(\tilde{r}_G, \tilde{d}_G, x) k(\Phi(\tilde{r}_G, \tilde{d}_G, x)) d\tilde{r}_G \\ \overline{P_r(\tilde{d}_G, x)} &= \int_0^\infty 2\pi\tilde{r}_G\tilde{d}_G \cdot f_{\alpha,\beta}(\tilde{r}_G, \tilde{d}_G, x) \hat{P}_r(\Phi(\tilde{r}_G, \tilde{d}_G, x)) d\tilde{r}_G \end{aligned} \quad (4.3.1)$$

Hoffmann et al.[142] proposed an incomplete gamma function Γ as the distribution function for grain radii in Si-doped HfO₂ ALD films, where the shape parameter is dependent on the stoichiometry. A similar investigation into Hf_{1-x}Zr_xO₂ ($x = 0, 0.19, 0.43, 0.70,$ and 1) by Park et al.[143] revealed a correlation between film thickness ($d_G = 14.2$ nm, 19.2 nm, 24.2 nm, and 29.2 nm) and grain radii. However, the strength of this correlation was found to be inversely correlated with the stoichiometry x , as pure ZrO₂ showed almost no correlation to film thickness. The thickness dependence of the grain radii was also observed by Kim et al.[79] in Hf_{0.5}Zr_{0.5}O₂. A beta distribution was fitted to the raw data of Park et al.[143] in Künneth et al.[51]

$$f_{\alpha,\beta}(\tilde{r}_G, \tilde{d}_G, x) = \frac{\Gamma(\alpha + \beta)}{\Gamma(\alpha)\Gamma(\beta)} \cdot \frac{1}{2g_S(x, \tilde{d}_G)} \cdot \left(\frac{\tilde{r}_G}{2g_S(x, \tilde{d}_G)}\right)^{\alpha-1} \times \left(1 - \frac{\tilde{r}_G}{2g_S(x, \tilde{d}_G)}\right)^{\beta-1} \quad (4.3.2)$$

α and β are fit parameters and were set to a value of 3 by manual adjustment, Γ is the gamma function. The distribution function is fitted to the experimental data by Park et al.(see Künneth et al. [144]) with the scale function g_S , which also includes the stoichiometry dependency.

$$g_S(x, \tilde{d}_G) = \tilde{d}_G \cdot \frac{7}{10} (1 - x) + 18\pi x \arctan\left(\frac{\tilde{d}_G}{10}\right) \quad (4.3.3)$$

The purpose of this model is to calculate phase fractions, dielectric constants and remanent polarization from a given stoichiometry and grain size distribution. The results of this model are depicted in chapter 5.5 and were published in 2017 in the Journal of Applied Physics[51].

5 Results of DFT Calculations

5.1 Convergence Study

In order to achieve reliable results when performing DFT calculations and not waste computational resources, a convergence study was performed. The parameters investigated are the energy cutoff of the plane wave basis set, the energy cutoff of the double grid surrounding each atom used for PAW calculations, and the number of k-points used in the k-point grid. The precision of the calculations increases with increasing values of these parameters, but so does the computational effort and memory usage.

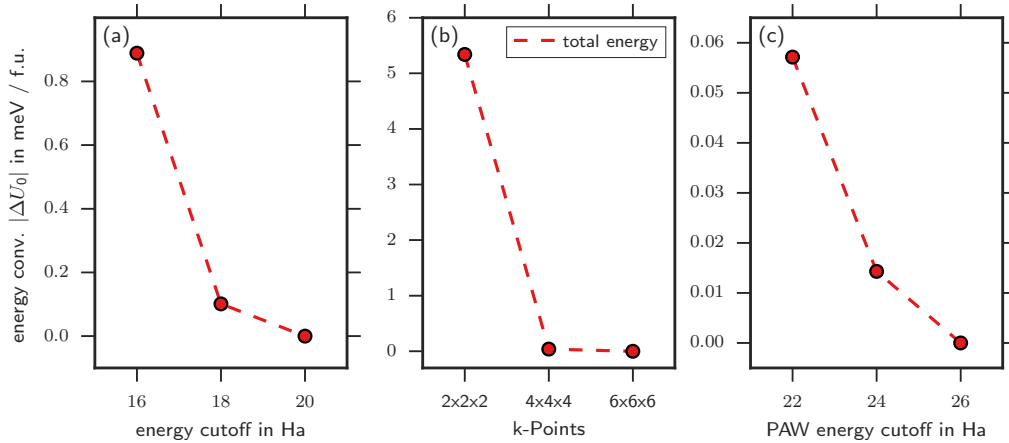


FIG. 5.1: The convergence of the total energy difference $|\Delta U_0|$ between the m- and f-phase as an absolute value. The most precise calculation serves as the reference point for the total energy. (a) depicts the total energy dependency from the energy cutoff, (b) from the k-point grid, and (c) from the PAW energy cutoff.

Figure 5.1 shows the convergence of the total energy difference between the m- and f-phase as a function of the three investigated parameters. The values of the most precise calculations are set to zero. At a value of 18 Ha for the energy cutoff, $|\Delta U_0|$ drops below 0.1 meV which shall be considered sufficiently converged. The same is true for a k-point grid of $4 \times 4 \times 4$ and a PAW cut off of 22 Ha. Figure 5.2 shows the convergence of the lattice constants a , b , and c as well as the unit cell volume of the f-phase. The values of the most precise calculations are set to zero. A convergence of 0.001 \AA or better for the lattice constants and 0.005 \AA^3 for the unit cell volume can be achieved with values of 18 Ha for the energy cutoff, $4 \times 4 \times 4$ for the k-point grid, and 22 Ha for the PAW cutoff. These values are therefore used in the set up of all other calculation as described in section 3.2. However, the k-point grid is being scaled to the size of the cell for supercell calculations.

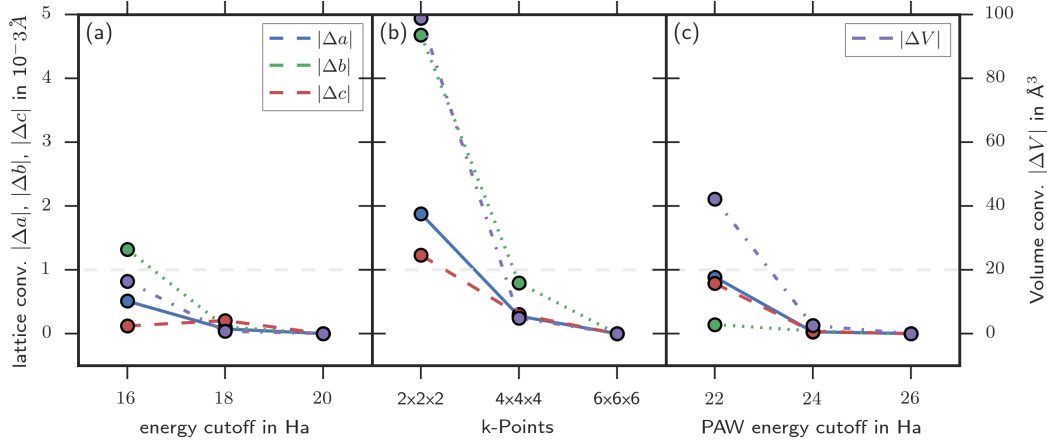


FIG. 5.2: The convergence of the lattice constants $|\Delta a|$, $|\Delta b|$, $|\Delta c|$, and $|\Delta V|$ for f-phase as an absolute value. The most precise calculation serves as the reference point. (a) depicts the lattice constant dependency from the energy cutoff, (b) from the k-point grid, and (c) from the PAW energy cutoff.

5.2 Total Energy and Structure

With the parameters from section 5.1 the total energy and lattice constants can be calculated. Table 5.1 shows the simulation results for 6 HfO₂ polymorphs for total energy, lattice constants (scaled to 12 atomic cell), cell volume (scaled to 12 atomic cell), and mass density. Ab initio values from the literature are provided for comparison. Experimental results are printed directly below the corresponding simulation results. The sequence in total energy from lowest to highest is m-, o-, f-, f'-, t-, and c-phase. Consequently, the total energy of the m-phase is set to zero for better comparison. The total energies of the other phases are given in reference to the m-phase. Comparing the total energy values of this work with those from the literature, it becomes apparent, that the sequence in total energy of the phases is preserved, regardless of the method used. Furthermore, the total energies of this work obtained with PAW atomic data files from the GBRV library resemble closely those obtained with the all-electron code FHI-AIMS from Künneth et al.[145], giving credibility to the chosen data set. While the sequence in total energy is preserved, the exact values differ depending on the chosen method. A particular trend that can be observed is, that the total energy values of the different phases cluster much more together with the LDA, than it is the case with GGA/PBE¹²

Table 5.1 also lists the lattice constants, cell volume and mass density of the different phases. These values are given for 12 atomic cells for better comparison. Values for the o-, f'-, t-, and c-phase were adjusted accordingly. Furthermore, table 5.1 attempts to present

¹PBE is a commonly used GGA functional.

²The total energy values of Huan et al.[47] may, in fact, be free energy values at 0 K and therefore contain a zero point energy contribution. The label 0 K is sometimes used for both physical quantities in the literature and the authors of [47] did not specify which convention they used.

the results in a uniform crystallographic orientation. Since the crystallographic orientation is not consistent throughout the literature, this means that the sequence of lattice constants is permuted compared to the original works. Specifically, this affects the f-phase of Müller et al.[26], as well as the f-and o-phase of Huan et al.[47]. In all three cases, the lattice constants a and b are exchanged. Values of the cell volume and mass density were calculated from the lattice constants and the atomic weights from the IUPAC technical report of 2016[36] if not provided within the original research.

LDA calculations are known to underestimate the values of lattice constants. This effect is known and recorded in the literature[146]. This can also be observed in the data presented here. This can in part be explained, that the ab initio calculations do not take the thermal expansion into account, while experimental values necessarily do. GGA/PBE calculations are better in reproducing experimental values for the lattice constants, even without taking the thermal expansion into account. It is possible to calculate the thermal expansion from first principles, however, this is beyond the scope of this work.

TABLE 5.1: Simulation and experimental results of the 6 HfO₂ polymorphs. Values for cell volume and mass density are calculated from lattice constants if not provided in the original research. Lattice constants are for 12 atomic cells.

Name	Symb.	Method	ΔU_0 [$\frac{\text{meV}}{\text{f.u.}}$]	a [Å]	b [Å]	c [Å]	β	V_{12} [Å ³]	ρ_m [$\frac{\text{g}}{\text{cm}^3}$]	
m-phase	P2 ₁ /c	LDA ¹	0.000	5.038	5.121	5.200	80.34°	132.251	10.57	
		LDA ²	0.000	5.120	5.175	5.298	80.3°	138.440	10.10	
		LDA ³	0.000	5.032	5.141	5.218	80.399°	133.595	10.47	
		PBE ⁴	0.000	5.14	5.20	5.31	80.2°	139.855	10.00	
		LDA ⁵	0.000	4.95	5.06	5.08	80.47°	125.483	11.14	
		PBE ⁶	0.000	5.085	5.159	5.262	80.298°	136.066	10.28	
		GGA ⁷	0.000	5.128	5.191	5.297	80.29°	138.983	10.06	
		LDA ⁷	0.000							
		<i>Exp.</i> ⁸			5.116	5.172	5.295	80.82°	138.04	10.13
		<i>Exp.</i> ⁹			5.07	5.14	5.29		136.09	10.27
<i>Exp.</i> ¹⁰			4.97	5.24	5.18		133.17	10.50		
o-phase	Pbca	LDA ¹	26.656	4.993	5.100	5.206	90.00°	132.547	10.55	
		LDA ²	24.014	5.077	5.155	5.296	90.00°	138.607	10.09	
		LDA ³	28.1	5.010	5.117	5.223	90.00°	133.898	10.44	
		PBE ⁴	70	5.015	5.08	5.27	90.00°	134.260	10.41	
		GGA ⁷	65	4.916	5.169	4.962	90.00°	126.088	11.09	
		LDA ⁷	29							
		<i>Exp.</i> ¹¹			5.01	5.11	5.23		133.89	10.44
f-phase	Pca2 ₁	LDA ¹	52.416	4.961	5.163	4.980	90.00°	127.550	10.96	
		LDA ²	61.974	5.037	5.237	5.056	90.00°	133.371	10.48	
		LDA ³	49.5	4.978	5.182	4.998	90.00°	128.928	10.84	
		PBE ⁴	80	5.01	5.29	5.08	90.00°	134.635	10.38	
		PBE ⁶	62.7	5.107	4.900	4.920	90.00°	123.120	11.36	
f'-phase	Pmn2 ₁	LDA ¹	108.496	5.040	5.065	5.040	83.80°	127.937	10.93	
		PBE ⁴	160	4.82	5.18	5.42		134.533	10.39	
t-phase	P4 ₂ /mnc	LDA ¹	113.989	4.984	4.984	5.072	90.00°	125.997	11.10	
		LDA ²	92.54	5.048	5.048	5.140	90.00°	130.979	10.67	
		LDA ³	115.8	5.004	5.004	5.102	90.00°	127.754	10.94	
		PBE ⁴	175	5.063	5.063	5.28	90.00°	135.347	10.33	
		PBE ⁶	137.1	5.030	5.030	5.146	90.00°	130.198	10.74	
		GGA ⁷	156	5.059	5.059	5.200	90.00°	133.086	10.51	
		LDA ⁷	99							
		<i>Exp.</i> ¹²			5.061	5.061	5.201		133.217	10.49
c-phase	Fm $\bar{3}$ m	LDA ¹	167.875	4.981	4.981	4.981	90.00°	123.585	11.31	
		LDA ²	135.777	5.047	5.047	5.047	90.00°	128.558	10.88	
		LDA ³		5.003	5.003	5.003	90.00°	125.207	11.17	
		PBE ⁶	208.2	5.029	5.029	5.029	90.00°	127.188	10.99	
		GGA ⁷	237	5.063	5.063	5.063	90.00°	129.785	10.77	
		LDA ⁷	152							
		<i>Exp.</i> ¹⁰			5.08	5.08	5.08		131.10	10.66

When comparing the ab initio results for lattice constants of this work with experimental results, one finds good agreement among them, apart from the before mentioned underestimation of about 1% to 2% due to the nature of LDA and the lack of thermal expansion. An exception to that rule appears to be the o-phase, where both all electron LDA and GBRV LDA produce quite accurate results, assuming the correctness of the experimental data. As a consequence, the o-phase is identified as the phase with the largest cell volume by ab initio calculations. As a result, one might be mistaken into believing that an o- to f-phase transition is a promising candidate for a giant piezoelectric effect when only looking at ab initio results, especially when taking into account the structural similarity of the two phases. However, this large volume difference between the two phases is not present in experimental data, where the m-phase has the largest volume of all phases. When comparing the results of PAW-LDA with atomic data sets from the GBRV library, LDA with SM pseudopotentials, and all electron LDA with FHI-AIMS one finds that GBRV better approximates the total energy of the all-electron code, but LDA with SM pseudo potentials produces better values for the lattice parameters than either of the other two LDA methods.

¹this work, with PAW atomic data sets from the GBRV library

²From Ref. [50], with SM-LDA pseudo potentials

³From Ref. [145], all electron LDA with FHI-AIMS

⁴From Ref. [47]

⁵From Ref. [48]

⁶From Ref. [49]

⁷From Ref. [147]

⁸From Ref. [148]

⁹From Ref. [26]

¹⁰From Ref. [149]

¹¹From Ref. [150]

¹²Extrapolated by Ref. [151] from [35]

Table 5.2 shows the simulation results for 6 $\text{Hf}_{0.5}\text{Zr}_{0.5}\text{O}_2$ polymorphs for total energy, lattice constants (scaled to 12 atomic cell), cell volume (scaled to 12 atomic cell), and mass density. Ab initio values from the literature are provided for comparison. Experimental results are printed directly below the corresponding simulation results. The $\text{Hf}_{0.5}\text{Zr}_{0.5}\text{O}_2$ data is presented in an identical fashion as the HfO_2 data.

TABLE 5.2: Simulation and experimental results of the 6 $\text{Hf}_{0.5}\text{Zr}_{0.5}\text{O}_2$ polymorphs. Values for cell volume and mass density are calculated from lattice constants if not provided in the original research. Lattice constants are for 12 atomic cells.

Name	Symb.	Method	ΔU_0 [$\frac{\text{meV}}{\text{f.u.}}$]	a [\AA]	b [\AA]	c [\AA]	β	V_{12} [\AA^3]	ρ_m [$\frac{\text{g}}{\text{cm}^3}$]
m-phase	P2 ₁ /c	LDA ¹	0.000	5.065	5.150	5.223	80.40°	134.326	8.25
		LDA ²	0.000	5.116	5.193	5.288	80.4°	138.521	8.00
		LDA ³	0.000	5.069	5.160	5.231	80.435°	134.920	8.21
		<i>Exp.</i> ⁴		<i>5.127</i>	<i>5.177</i>	<i>5.299</i>	<i>80.72°</i>	<i>138.80</i>	<i>7.98</i>
o-phase	Pbca	LDA ¹	25.354	5.021	5.128	5.228	90.00°	134.608	8.23
		LDA ²	24.636	5.075	5.172	5.289	90.00°	138.825	7.98
		<i>Exp.</i> ⁵		<i>5.024</i>	<i>5.071</i>	<i>5.249</i>		<i>133.73</i>	<i>8.29</i>
f-phase	Pca2 ₁	LDA ¹	44.663	4.989	5.188	5.005	90.00°	129.549	8.55
		LDA ²	49.090	5.041	5.241	5.057	90.00°	133.605	8.30
		LDA ³	43.6	4.998	5.197	5.015	90.00°	130.263	8.51
		<i>Exp.</i> ⁶		<i>5.01</i>	<i>5.25</i>	<i>5.05</i>		<i>132.83</i>	<i>8.34</i>
f'-phase	Pmn2 ₁	LDA ¹	88.992	5.052	5.103	5.057	84.96°	129.864	8.53
t-phase	P4 ₂ /mnc	LDA ¹	80.791	5.008	5.011	5.091	90.00°	127.763	8.67
		LDA ²	70.775	5.055	5.054	5.144	90.00°	131.419	8.43
		LDA ³	81.1	5.016	5.019	5.105	90.00°	128.541	8.62
c-phase	Fm $\bar{3}$ m	LDA ¹	135.691	5.004	5.005	5.005	90.00°	125.338	8.84
		LDA ²	118.040	5.051	5.051	5.050	90.00°	128.839	8.60

The sequence in total energy from lowest to highest is m-, o-, f-, t-, f'-, and c-phase. This means the t-phase has overtaken the f'-phase. Otherwise, the sequence remains the same as in HfO_2 . However, the total energies are clustered more closely together than in HfO_2 , regardless of method. Despite experimental observation of ferroelectric behavior in $\text{Hf}_{0.5}\text{Zr}_{0.5}\text{O}_2$ by Müller et al.[26] and others, neither ferroelectric phase becomes energetically stable. This means that the observed ferroelectricity in $\text{Hf}_{1-x}\text{Zr}_x\text{O}_2$ thin films is not an effect of the total energy alone. Consequently, this means other effects must contribute. Similar to HfO_2 , the

¹this work, with PAW atomic data sets from the GBRV library

²From Ref. [50], with SM-LDA pseudo potentials

³From Ref. [51], all electron LDA with FHI-AIMS

⁴From Ref. [34] at 1000 °C $\text{Hf}_{0.60}\text{Zr}_{0.40}\text{O}_2$

⁵From Ref. [150]

⁶From Ref. [26]

PAW calculations with the GBRV atomic data sets resemble the all-electron calculations with FHI-AIMS more closely in terms of total energy, than the SM-PP calculations do. However, when comparing the lattice parameters of experiment and simulation, SM-PP calculations are a closer fit than either GBRV or all-electron calculations. A similar trend was observed in HfO₂. Likewise, the lattice constants have a tendency to come out short in the ab initio calculations due to the LDA.

Table 5.3 shows the simulation results for 6 ZrO₂ polymorphs for total energy, lattice constants (scaled to 12 atomic cell), cell volume (scaled to 12 atomic cell), and mass density. Ab initio values from the literature are provided for comparison. Experimental results are printed directly below the corresponding simulation results. The ZrO₂ data is presented in an identical fashion as the HfO₂ and Hf_{0.5}Zr_{0.5}O₂ data previously. The sequence in total energy from lowest to highest is m-, o-, f-, t-, f'-, and c-phase, and therefore identical to Hf_{0.5}Zr_{0.5}O₂. The total energies are clustered even more closely together than in HfO₂ and Hf_{0.5}Zr_{0.5}O₂. The trend, that calculations with the GBRV library fit closely to the all-electron calculations with FHI-AIMS, while calculations with the SM-PP best fit the experimental lattice constants remains true for ZrO₂.

To summarize the data from Tables 5.1 to 5.3, the total energy results of this work are consistent with results taken from the literature. The total energy sequence of the various phases is identical across the literature and the values obtained with the GBRV library closely resemble the results obtained with the all-electron code FHI-AIMS for all stoichiometries. The total energies cluster closer together with increasing Zr content, meaning the energy difference between the phases is smaller for Zr rich crystals than for Hf rich crystals. The total energy of Hf_{1-x}Zr_xO₂ can be well approximated from the weighted averages of pure HfO₂ and ZrO₂, although small deviations in the meV range do exist. The largest deviation from the average of pure HfO₂ and ZrO₂ exists for the f'-phase with 5.34 meV. The total energy alone proved insufficient to explain the observed ferroelectricity regardless of stoichiometry. Looking at the cell volume, an increase in volume with Zr content is observable in the ab initio data. This trend is consistent with the presented experimental data. The following sections of this work will take a closer look at various factors expected to influence the sequence in energies of the different phases.

TABLE 5.3: Simulation and experimental results of the 6 ZrO₂ polymorphs. Values for cell volume and mass density are calculated from lattice constants if not provided in the original research. Lattice constants are for 12 atomic cells.

Name	Symb.	Method	ΔU_0 [$\frac{\text{meV}}{\text{f.u.}}$]	a [Å]	b [Å]	c [Å]	β	V_{12} [Å ³]	ρ_m [$\frac{\text{g}}{\text{cm}^3}$]	
m-phase	P2 ₁ /c	LDA ¹	0.000	5.088	5.184	5.243	80.46°	136.390	6.00	
		LDA ²	0.000	5.106	5.221	5.262	80.541°	138.369	5.91	
		LDA ³	0.000	5.088	5.179	5.244	80.45°	136.268	6.01	
		LDA ⁴	0.000	5.09	5.20	5.24	80.61°	136.834	5.98	
		LDA ⁵	0.000	5.085	5.183	5.240	80.54°	136.225	6.01	
		PBE ⁵	0.000	5.190	4.243	5.379	80.35°	116.776	7.01	
		GGA ⁶	0.000	5.197	5.280	5.350	80.47°	144.779	5.65	
		LDA ⁶	0.000							
		<i>Exp.</i> ⁷			5.159	5.204	5.324	80.97°	141.16	5.80
		<i>Exp.</i> ⁸			5.15	5.21	5.315	80.69°	140.73	5.82
<i>Exp.</i> ⁹			5.14	5.27	5.32		142.32	5.75		
o-phase	Pbca	LDA ¹	24.305	5.048	5.159	5.251	90.00°	136.735	5.99	
		LDA ²	25.158	5.069	5.198	5.264	90.00°	138.699	5.90	
		LDA ³	24.6	5.047	5.156	5.250	90.00°	136.615	5.99	
		LDA ⁵	26.124	4.987	5.212	5.030	90.00°	130.741	6.26	
		PBE ⁵	67.47	5.008	5.299	5.132	90.00°	136.190	6.01	
		GGA ⁶	49	5.087	5.315	5.1	90.00°	137.891	5.94	
		LDA ⁶	14							
		<i>Exp.</i> ¹⁰			5.043	5.262	5.091		141.879	5.77
f-phase	Pca2 ₁	LDA ¹	39.997	5.016	5.215	5.032	90.00°	131.651	6.22	
		LDA ²	36.604	5.043	5.247	5.055	90.00°	133.758	6.12	
		LDA ³	39.7	5.016	5.213	5.031	90.00°	131.562	6.22	
		LDA ⁴	33.8	5.02	5.22	5.04	90.00°	132.070	6.20	
		<i>Exp.</i> ¹¹			5.068	5.260	5.077		135.34	6.05
f'-phase	Pmn2 ₁	LDA ¹	80.202	5.077	5.134	5.077	85.43°	131.898	6.21	
t-phase	P4 ₂ /mnc	LDA ¹	50.708	5.033	5.033	5.112	90.00°	129.497	6.32	
		LDA ²	49.657	5.060	5.060	5.149	90.00°	131.833	6.21	
		LDA ³	48.1	5.031	5.031	5.110	90.00°	129.339	6.33	
		LDA ⁴	34.3	5.04	5.04	5.12	90.00°	130.056	6.29	
		LDA ⁵	49.86	5.032	5.032	5.110	90.00°	129.390	6.33	
		PBE ⁵	112.02	5.122	5.122	5.284	90.00°	138.625	5.90	
		GGA ⁶	109	5.132	5.132	5.207	90.00°	137.139	5.97	
		LDA ⁶	38							
		<i>Exp.</i> ¹²			5.08	5.08	5.17		133.42	6.13
		<i>Exp.</i> ⁸			5.080	5.080	5.194		134.038	6.09
<i>Exp.</i> ⁹			5.048	5.048	5.149		131.208	6.24		

Name	Symb.	Method ^e	ΔU_0 [$\frac{\text{meV}}{\text{f.u.}}$]	a [Å]	b [Å]	c [Å]	β	V_{12} [Å ³]	ρ_m [$\frac{\text{g}}{\text{cm}^3}$]
c-phase	Fm $\bar{3}$ m	LDA ¹	95.362	5.029	5.029	5.029	90.00°	127.155	6.44
		LDA ²	100.917	5.055	5.055	5.055	90.00°	129.171	6.34
		LDA ³	94.4	5.027	5.027	5.027	90.00°	127.036	6.44
		LDA ⁴	82.0	5.03	5.03	5.03	90.00°	127.036	6.44
		LDA ⁵	93.78	5.028	5.028	5.028	90.00°	127.112	6.44
		PBE ⁵	215.22	5.118	5.118	5.118	90.00°	134.061	6.10
		GGA ⁶	171	5.128	5.128	5.128	90.00°	134.848	6.07
		LDA ⁶	67						
	<i>Exp.</i> ¹³			5.12	5.12	5.12		134.22	6.10

5.3 DFPT calculations

The first factor investigated is the role of temperature and entropy. The entropy contribution to the Helmholtz free energy was calculated from DFPT phonon modes according to equation 2.4.27. Figure 5.3 depicts the Helmholtz free energy as a function of temperature for (a) HfO₂ and (b) ZrO₂. The SM-PPs were fine-tuned to a set of criteria that included accurate values for the m- to t-phase transition temperature. As a result, the values of the phase transition temperatures of the SM-LDA PP fit the experimental data better than the GBRV or AIMS values³. The experimental equilibrium values for the m- to t-phase transition are 2052 K and 1367 K [42] for HfO₂ and ZrO₂ respectively. GBRV produces values of approximately 1740 K and 2500 K, while SM-LDA produces values of approximately 2070 K and 1270 K for HfO₂ and ZrO₂ respectively. Values for AIMS are 2150 K and 1450 K for HfO₂ and ZrO₂ respectively. The Helmholtz free energies of the o- and f'-phase are omitted from Figure 5.3, as the corresponding DFPT calculations did not converge with the GBRV library. The c-phase was omitted since the cubic phase has imaginary phonon modes. This is in conflict with equation 2.4.27, which assumes no imaginary phonon modes. However, data for both the o- and c-phase can be found in [50] for the SM-LDA pseudopotentials. As can be expected from a known high-temperature phase, the t-phase shows a strong dependency of

¹this work, with PAW atomic data sets from the GBRV library

²From Ref. [50], with SM-LDA pseudo potentials

³From Ref. [51], all electron LDA with FHI-AIMS

⁴From Ref. [48]

⁵From Ref. [152]

⁶From Ref. [147]

⁷From Ref. [34]

⁸From Ref. [45]

⁹From Ref. [149]

¹⁰From Ref. [53]

¹¹From Ref. [153]

¹²From Ref. [26]

¹³From Ref. [154]

³Anharmonic effects were neglected here. The inclusion of these effects might lead to improved values for GBRV and AIMS, and a decrease in accuracy for SM-LDA

the Helmholtz free energy from the temperature. In contrast, the f-phase shows very little dependency of the Helmholtz free energy from the temperature. It is therefore not possible to stabilize the f-phase with temperature. In fact, an increase in temperature will contribute to the destabilization of the f-phase, which is typical for ferroelectrics (see Landau-Devonshire Model in chapter 2.2.3).

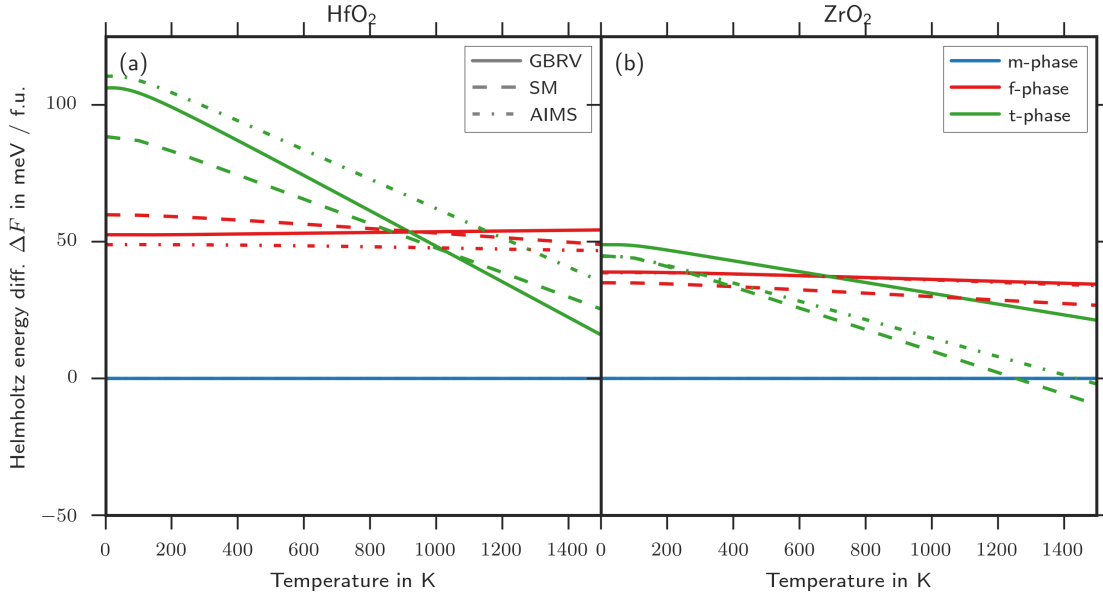


FIG. 5.3: Helmholtz free energy as a function of temperature for (a) HfO_2 and (b) ZrO_2 . Phase is marked by line color, pseudopotential library by line type. Results obtained with the PAW atomic data sets from the GBRV library are plotted with a continuous line, results obtained with the SM-pseudo potentials in dashed line. Results obtained with the all electron code FHI-AIMS are represented by a dash-dotted line.

The DFPT results obtained with the GBRV library are further analyzed with the ANADDB tool included with the ABINIT package. The resulting dielectric properties are tabulated in table 5.4. The dielectric tensor values vary only slightly between HfO_2 and ZrO_2 . The m-phase has the smallest k-value of all three investigated phases, closely followed by the f-phase. However, the t-phase shows significantly increased values, which is why this phase is used as a high-k dielectric in ZrO_2 DRAM capacitors[41] and HfO_2 logic transistors[2]. The k-values of both HfO_2 and ZrO_2 are high in comparison with other possible gate oxide materials such as SiO_2 ($k = 3.9$ [155]) or Al_2O_3 ($k = 9$ [155]).

TABLE 5.4: Dielectric tensor elements and average dielectric constants for HfO₂ and ZrO₂ calculated with LDA DFPT with the GBRV library. The depicted values are the sum of the electronic dielectric tensor and the ion dielectric tensor.

	HfO ₂				ZrO ₂			
	k_{11}	k_{22}	k_{33}	k	k_{11}	k_{22}	k_{33}	k
m-phase	24.34	22.20	18.74	21.76	27.13	25.04	20.64	24.27
f-phase	27.39	23.10	27.36	25.92	31.27	25.71	29.30	28.76
t-phase	41.13	41.13	23.57	35.28	53.50	53.50	25.09	44.03

The piezoelectric tensor elements e_{ikl} including values for the transversal effect (e_{31}), longitudinal effect (e_{33}), and shear effect (e_{15}) can be found in table 5.5. The piezo shear effect of HfO₂ and ZrO₂ is small in comparison to both LiNbO₃ and PZT-4. The longitudinal effect of HfO₂ and ZrO₂ is of opposite sign, but about equal in magnitude with LiNbO₃, but significantly smaller than PZT-4. The transversal effect of HfO₂ and ZrO₂ is larger in magnitude than LiNbO₃ but still smaller than PZT-4.

TABLE 5.5: Piezoelectric tensor elements e_{ikl} in C/m² for HfO₂ and ZrO₂ calculated with LDA-DFPT with the GBRV library as well as experimental values of common piezo materials for comparison

	e_{15}	e_{24}	e_{31}	e_{32}	e_{33}
HfO ₂	0.68	-0.17	-1.49	-1.14	-1.67
ZrO ₂	0.75	-0.19	-1.62	-1.11	-1.67
LiNbO ₃ ¹	3.65		0.31		1.72
PZT-4 ²	12.7		-5.2		15.1

Table 5.6 shows the main elements of the elastic tensor K_{ijkl} in Voigt notation for the m-, f-, and t-phase for HfO₂ and ZrO₂. The complete tensors can be found in Appendix C in section 6.

TABLE 5.6: Elastic main tensor elements (in Voigt notation) K_{ijkl} in GPa for HfO₂ and ZrO₂ calculated with LDA-DFPT with the GBRV library

		K_{11}	K_{22}	K_{33}	K_{44}	K_{55}	K_{66}
m-phase	HfO ₂	395	497	314	120	110	165
	ZrO ₂	362	457	284	108	96.3	149
f-phase	HfO ₂	456	481	445	117	110	160
	ZrO ₂	425	440	406	106	98.3	143
t-phase	HfO ₂	581	408	581	54.5	96.7	54.5
	ZrO ₂	533	384	533	57.9	71.9	87.6

Berry-phase calculations for the f-phase yields the polarization vector. Table 5.7 shows both the vector elements and its modulus. The derived values for the polarization are too high compared to experimental values, which are in the range of 20 $\mu\text{C}/\text{cm}^2$ [26, 141, 158] with

¹Ref. [156]

²Ref. [157]

a coercive field strength in the range of 1 MV/cm[26, 159, 141, 160]. However, experimental values usually measure the average polarization of multiple grains of random orientation. Therefore, a factor of 0.5 must be taken into account[51]. The theoretical values are therefore consistent with experimental values. Experimental values of PZT-4 for comparison are 31 $\mu\text{C}/\text{cm}^2$ for the polarization and 14.4 kV/cm[161] for the coercive field.

TABLE 5.7: Ferroelectric vector \mathbf{P}_r in $\mu\text{C}/\text{cm}^2$ for HfO_2 , $\text{Hf}_{0.5}\text{Zr}_{0.5}\text{O}_2$, and ZrO_2 calculated with Berry-Phase with the SM-PP

	P_{r1}	P_{r2}	P_{r3}
HfO_2	0.0	0.0	50.4
$\text{Hf}_{0.5}\text{Zr}_{0.5}\text{O}_2$	0.0	0.0	54.1
ZrO_2	0.0	0.0	57.9

5.4 Stress and Strain

Stress and Strain have been suspected to be responsible for the stabilization of the ferroelectric phase. Park et al. suggested, that tensile strains in t-phase $\text{Hf}_{0.5}\text{Zr}_{0.5}\text{O}_2$ causes a phase transformation into the f-phase [78]. Batra et al suggest stress as an important factor in the stabilization of the f-phase as well and particularly identifies capping and lattice and thermal coefficient mismatch as sources of these stresses[162]. However, Reyes-Lillo et al. propose epitaxial strain as the source of ferroelectricity[48]. In the following, these hypotheses are tested by studying the influence of various stress conditions on phase stability with ab initio calculations. The occurrence of stress necessitates the enthalpy as the chosen thermodynamic potential for determining the stable phase. A change in enthalpy is equal to the sum of the change in internal energy and the pressure-volume work of the system against its surroundings at a constant pressure as defined by equation 2.1.6. There are three principle stress conditions: mono-axial stress, bi-axial stress, and tri-axial stress. Thin films are typically associated with bi-axial stress. This is a consequence of the different thermal expansion coefficients of thin film and substrate. Thin films crystallized at a high temperature grow stress-free, but the difference in thermal expansion coefficients results in a bi-axial stress. This stress does not need to be equi-bi-axial, but due to a combination of endless bi-axial stress conditions and limitations in computational power, only two cases are considered: Both stress components are equal (equi-bi-axial) or one stress condition is zero (uni-axial). An example of a tri-axial stress is the stress of a grain surface on the core of the grain. Again, the individual stress components do not need to be equal, but due to limitations in computational power only hydrostatic (equi-tri-axial) stresses are considered. In this chapter, the sign convention of the ABINIT code is used for the mechanical stress. This means negative values correspond to compressive stress, positive values correspond to tensile stress.

5.4.1 Uni-axial Stress

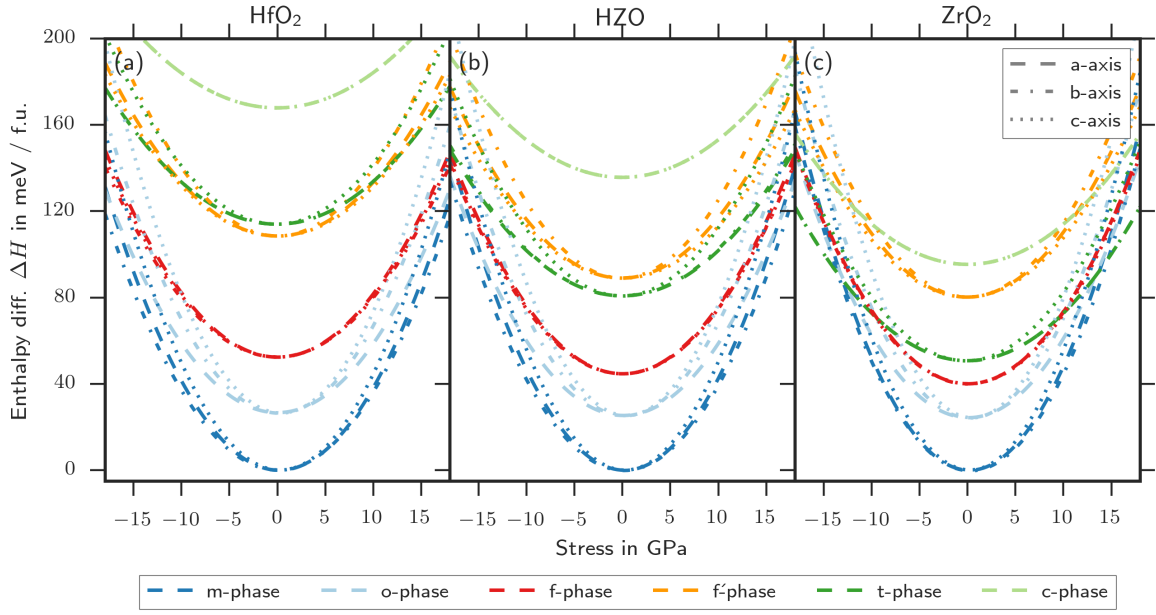


FIG. 5.4: Enthalpy as a function of applied uni-axial stress. (a) HfO_2 , (b) $\text{Hf}_{0.5}\text{Zr}_{0.5}\text{O}_2$, and (c) ZrO_2 . Phase is marked by line color, stress direction by line type.

Figure 5.4 depicts the enthalpy of the various polymorphs of (a) HfO_2 , (b) $\text{Hf}_{0.5}\text{Zr}_{0.5}\text{O}_2$ (HZO), and (c) ZrO_2 as a function of uni-axial stress from -18 GPa to 18 GPa. The anisotropic nature of the applied stress and stress and strain fall outside the range of validity of the Birch–Murnaghan equation of state. For this reason, a polynomial fit, truncated after the 2nd order term, was used to fit the enthalpy values to the applied stress and strain. This approach is justified, since the technological relevant range of stress in the range of 1 GPa to 2 GPa[143] is covered by DFT calculations. However, extrapolations beyond the range of the DFT calculations are subject to a degree of uncertainty. The parabolic regression curves based on DFT calculations are depicted in figure 5.5. The stress direction in figure 5.4 is indicated by line type, phase is indicated by line color. The sensitivity of the enthalpy to an external stress is dictated by the compliance coefficients of the corresponding phase, and therefore dependent on the stress direction. For example, the monoclinic phase reacts most sensitive to an applied stress along the crystallographic $[001]$ -direction (high E-module in c-axis, dotted line) and least sensitive to an applied stress along the crystallographic $[010]$ -direction (low E-module in b-axis, dash-dotted line). The spatial orientation of the various polymorphs relative to each other is therefore important to consider when comparing enthalpy values under uni-axial stress. Two scenarios shall be discussed in the following in more detail:

1. The spatial orientation of polymorphs relative to each other is free, the various phases compete with each other based on the energetically most favorable orientation.

2. The spatial orientation of polymorphs relative to each other is fixed, the various phases compete with each other based on the E-module in a given crystallographic direction.

Scenario 1: For HfO_2 and $\text{Hf}_{0.5}\text{Zr}_{0.5}\text{O}_2$ there are no uni-axial stress conditions that lead to any phase being energetically more favorable than the m-phase in the range from -18 GPa to 18 GPa as depicted in figure 5.4. However, based on the trajectory of the parabolic regression curves, the o-phase will eventually become the energetically most favorable phase for stress values in excess of ± 18 GPa. This is due to the low E-module of the o-phase in the crystallographic $[100]$ -direction (a-axis, dashed line). In ZrO_2 , the t-phase becomes the energetically most favorable phase for stress values in excess of ± 12 GPa due to the low E-module of the t-phase in the crystallographic equivalent a- and b-axis. The c-axis of the t-phase does react much stronger to uni-axial stress and is therefore energetically less favorable. The f'-phase reacts most strongly to stress along the b-axis and weakest to stress along the c-axis. Since the f'-phase has a higher E-module than the t-phase it can never be stabilized by uni-axial stress. The E-module of the f-phase is highly isotropic. The f-phase cannot be stabilized by uni-axial stress in either stoichiometry. In c-phase all crystallographic directions are equivalent, therefore no direction dependency exists. The c-phase has the lowest uni-axial E-module of all phases, but due to the high starting enthalpy it cannot be stabilized within the investigated stress range.

Scenario 2: Figure 5.5 depicts the enthalpy of the various polymorphs of (a)-(c) HfO_2 , (d)-(f) $\text{Hf}_{0.5}\text{Zr}_{0.5}\text{O}_2$, and (g)-(i) ZrO_2 as a function of uni-axial stress. Considering the symmetry of the six phases, there are 108 combinations of parabolic regression curves possible. For the sake of brevity, only the three possibilities, where the axes are aligned, are depicted in figure 5.5. Readers interested in other possible orientations can view the relevant data in figure 5.4. Parabolic regression curves ranging from -18 GPa to 18 GPa were fitted based on the DFT calculations performed in the range from -5 GPa to 5 GPa in intervals of 1 GPa. Fixing the spatial orientation of the polymorphs relative to each other leads to possibilities for stress-induced phase transitions.

Stress along the a-axis greatly favors the o-phase. Hence, the o-phase becomes the energetically most favorable phase at $p < -17.5$ GPa and $p > -19.5$ GPa in HfO_2 and $p < -14.8$ GPa and $p > -16.2$ GPa in HZO. In ZrO_2 the intercepts of the m- and o-phase are at $p = -13.4$ GPa and $p = 14.4$ GPa, but the t-phase becomes more favorable than either phase at the same time. Although the f-phase will become energetically more favorable than either the m- or o-phase, the t-phase will do so before. As a result, the f-phase will not be

stabilized.

Uni-axial stress along the b-axis allows for the f-phase in small ranges at very high stress values. For HfO_2 these ranges are from -23.5 GPa to -28.2 GPa and 24.1 GPa to 28.2 GPa. For $\text{Hf}_{0.5}\text{Zr}_{0.5}\text{O}_2$ the range is from -19.9 GPa to -20.6 GPa. No range exists for tensile stress in $\text{Hf}_{0.5}\text{Zr}_{0.5}\text{O}_2$ and in ZrO_2 . Higher stress values lead to the formation of the t-phase.

The most effective way to stabilize the f-phase with uni-axial stress is with stress along the polar c-axis, since the m-, o-, and t-phase all have a particular high E-module in this axis and are therefore less favorable. This leads to very large ferroelectric stress windows. For HfO_2 these windows range from -16.1 GPa to -81.3 GPa and 17.4 GPa to 90.0 GPa and for ZrO_2 from -12.2 GPa to -18.1 GPa and 13.0 GPa to 25.7 GPa. For $\text{Hf}_{0.5}\text{Zr}_{0.5}\text{O}_2$ the f-phase becomes stable at stress values < -13.5 GPa and >14.6 GPa.

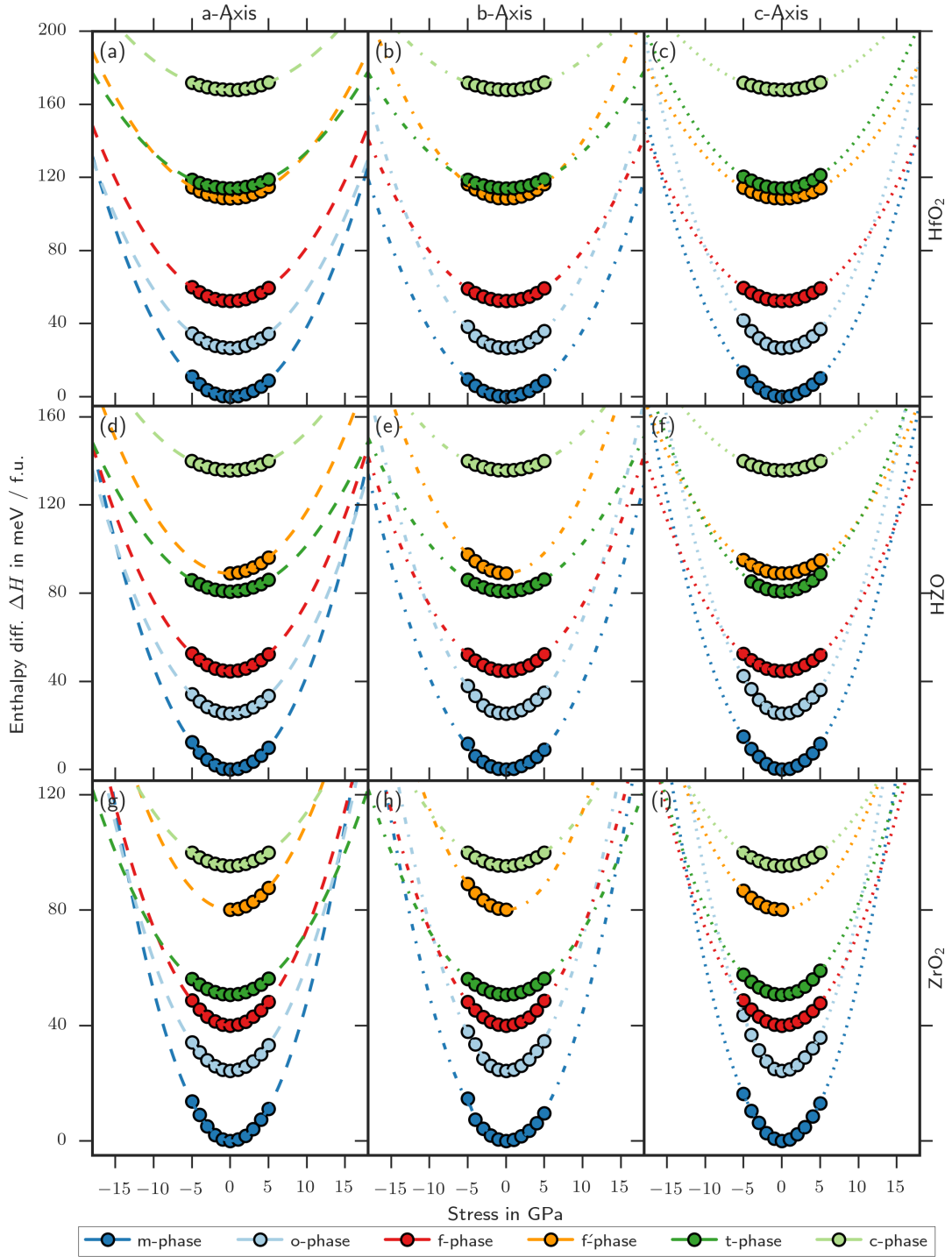


FIG. 5.5: Enthalpy as a function of applied uni-axial stress. (a)-(c) HfO_2 , (d)-(f) $\text{Hf}_{0.5}\text{Zr}_{0.5}\text{O}_2$, and (g)-(i) ZrO_2 . Phase is marked by line color, stress direction by line type. The spatial orientation of polymorphs relative to each other is fixed, the various phases compete with each other based on the E-module in a given crystallographic direction.

5.4.2 Uni-axial Strain

The results of the uni-axial stress calculations can be interpreted in a different manner, yielding different results. Implicit in the results depicted in figure 5.4 and figure 5.5 was the assumption, that the system was in a relaxed monoclinic ground state, which needed to be destabilized by stress. An alternative interpretation can be derived, when plotting the enthalpy of the stress calculations over the length of the lattice vector as depicted in figure 5.6. This implies, that the system is restricted by some manner of confinement and therefore not in the relaxed ground state. The possible nature of such confinements will be discussed later on, but is related to the history/production process experienced by the thin film. For now, it is important to note, that these confinements open up the possibility of stabilizing other phases than the m-phase, while the system experiences only a small amount of stress. Strain of the a-axis is not sufficient to stabilize any other phase than the m-phase for all stoichiometries, since the minima of the enthalpy all fall relatively close to each other. Compressive strain of the b-axis leads the m- and o-phase becoming indistinguishable in terms of enthalpy. Hence, HfO_2 and $\text{Hf}_{1-x}\text{Zr}_x\text{O}_2$ films with a constricted b-axis might exhibit a phase mixture of those two phases. Additionally, in the case of ZrO_2 , the t-phase becomes indistinguishable to both the m- and o-phase. Since the depicted results exclude thermal effects which further stabilize the t-phase, ZrO_2 thin films with a compressed b-axis should be primarily tetragonal. The c-axis of the f-phase is particularly small in comparison to the other investigated phases. Therefore, the f-phase can easily be stabilized by compressive strain, since all other phases require a much larger amount of compression and are therefore energetically more expensive. This holds true for all stoichiometries. Unfortunately, this is difficult to utilize technologically, since the compression by lattice mismatch would require the polar axis to be in-plane and therefore not measurable.

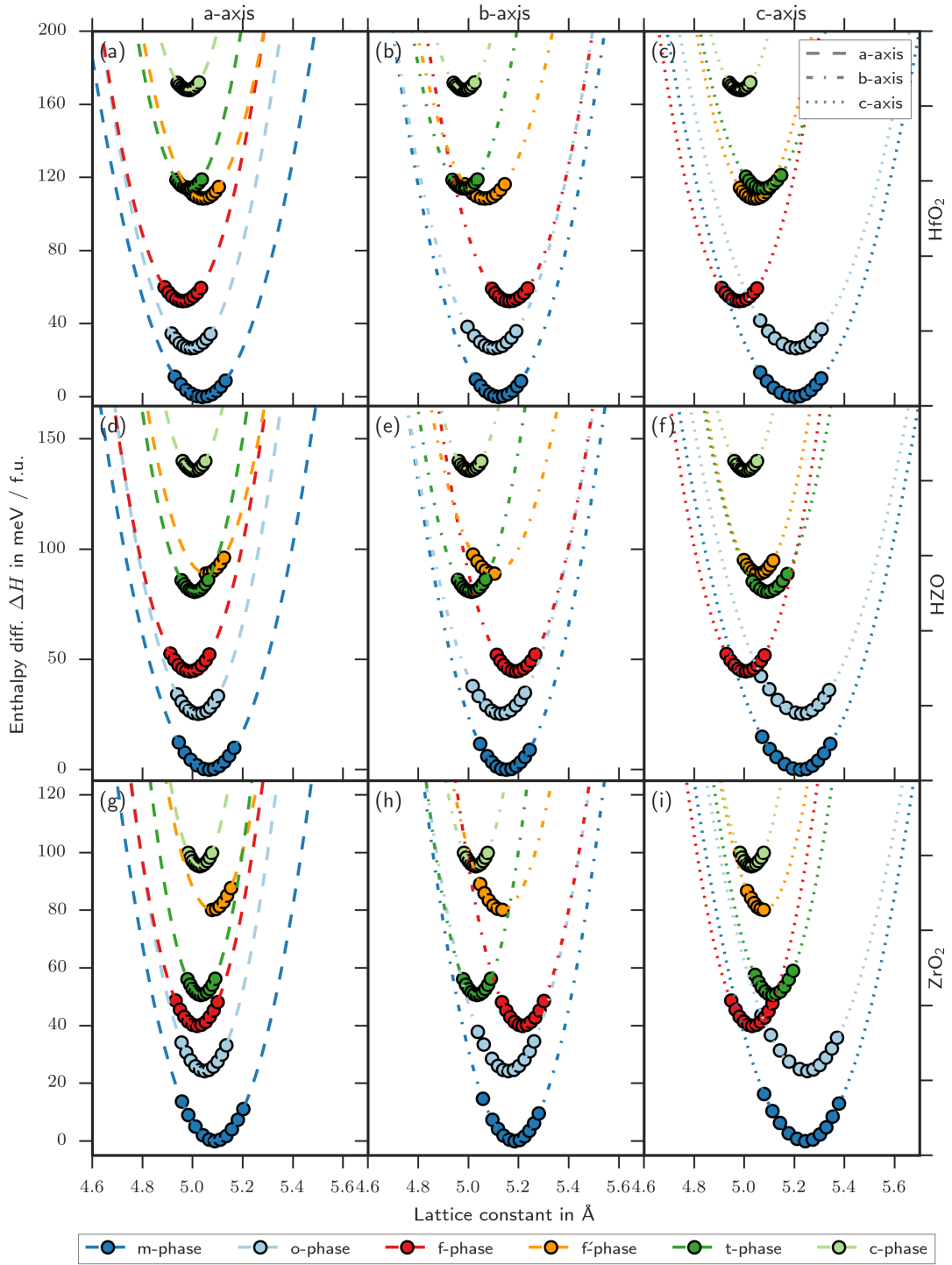


FIG. 5.6: Enthalpy as a function of lattice constants. (a)-(c) HfO_2 , (d)-(f) $\text{Hf}_{0.5}\text{Zr}_{0.5}\text{O}_2$, and (g)-(i) ZrO_2 . Phase is marked by line color, strain direction by line type. The spatial orientation of polymorphs relative to each other is fixed, the various phases compete with each other based on the E-module in a given crystallographic direction.

5.4.3 Bi-axial Stress

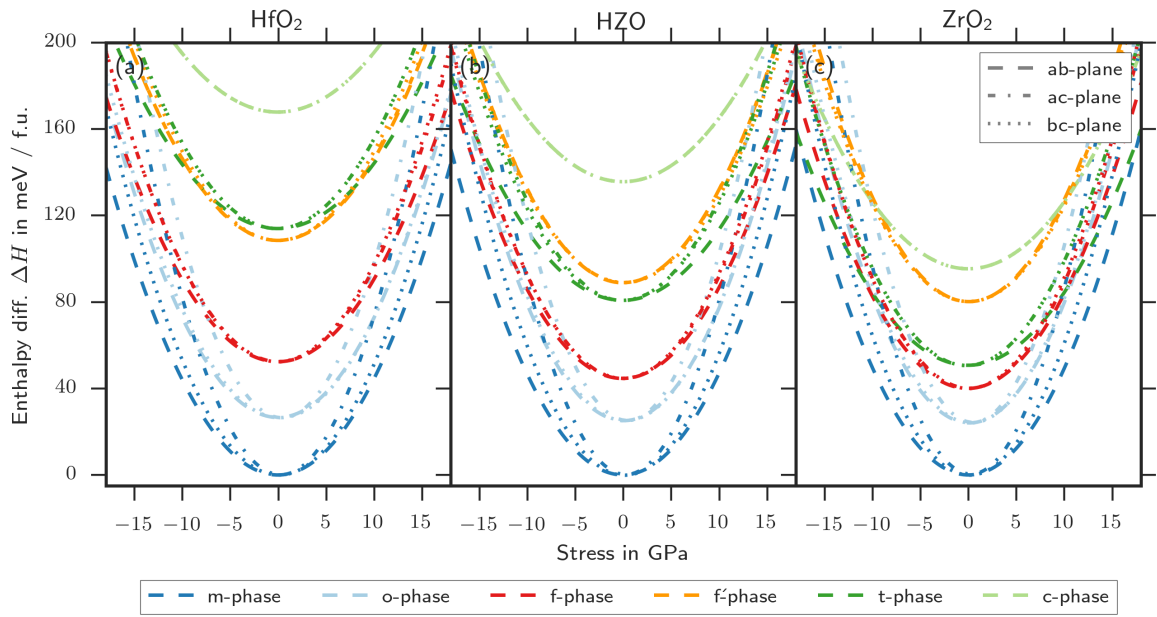


FIG. 5.7: Enthalpy as a function of applied bi-axial stress. (a) HfO_2 , (b) $\text{Hf}_{0.5}\text{Zr}_{0.5}\text{O}_2$, and (c) ZrO_2 . Phase is marked by line color, stress direction by line type.

Figure 5.7 depicts the enthalpy of the various polymorphs of (a) HfO_2 , (b) $\text{Hf}_{0.5}\text{Zr}_{0.5}\text{O}_2$ (HZO), and (c) ZrO_2 as a function of bi-axial stress from -18 GPa to 18 GPa. The individual curves are parabolic regression curves based on DFT calculations depicted in figure 5.8. The stress planes in figure 5.7 are indicated by line type, phase is indicated by line color. The sensitivity of the enthalpy to an external stress is dependent on the stress plane. Similar to the uni-axial case, the same two scenarios can be constructed. In **scenario 1**, all stress planes compete with each other, in **scenario 2** the orientation of the various phases is fixed and only select stress planes compete with each other.

Scenario 1 does not lead to a stabilization of the f-phase as the t-phase is always stabilized before the f-phase for all stoichiometries.

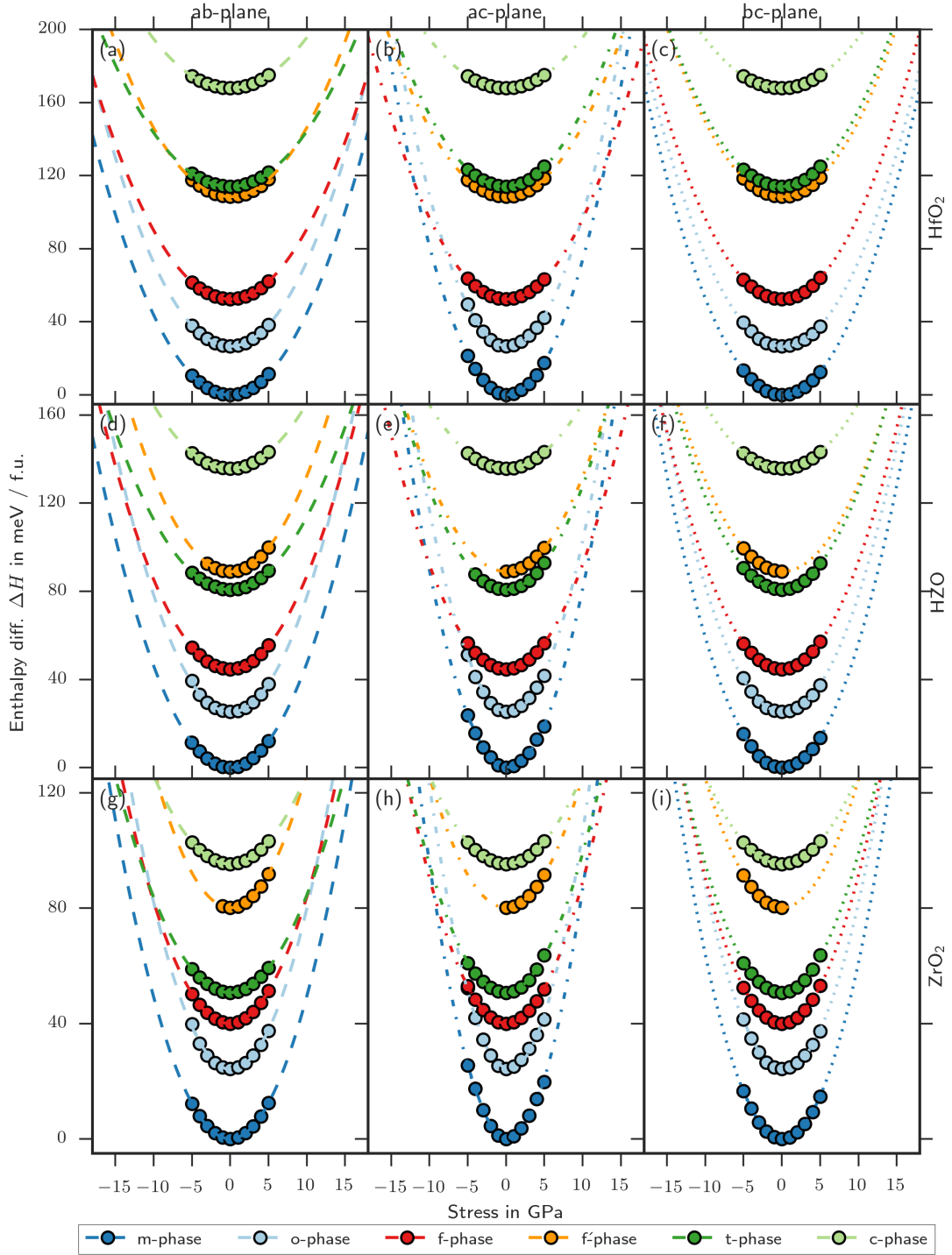


FIG. 5.8: Enthalpy as a function of applied bi-axial stress. (a)-(c) HfO_2 , (d)-(f) $\text{Hf}_{0.5}\text{Zr}_{0.5}\text{O}_2$, and (g)-(i) ZrO_2 . Phase is marked by line color, stress plane by line type. The spatial orientation of polymorphs relative to each other is fixed, the various phases compete with each other based on the sensitivity of the enthalpy to an external stress in a given crystallographic plane.

In **Scenario 2**, there are some conditions that lead to the stabilization of the f-phase. For bi-axial stress applied to the ac-plane, the range of ferroelectric stability ranges from -12.0 GPa to -39.1 GPa and from 13.0 GPa to 43.0 GPa for HfO_2 , from -10.3 GPa to -54.7 GPa and from 11.5 GPa to 60.2 GPa for $\text{Hf}_{0.5}\text{Zr}_{0.5}\text{O}_2$, from -9.4 GPa to -14.5 GPa and from 10.3 GPa to 22.6 GPa for ZrO_2 . For larger stress values, the t-phase is stabilized. For bi-axial stress in the bc-plane the f-phase becomes stable in the range of -25.8 GPa to -37.1 GPa and from 27.7 GPa to 38.3 GPa for HfO_2 and from -20.5 GPa to -26.9 GPa and from 22.6 GPa to 28.6 GPa for $\text{Hf}_{0.5}\text{Zr}_{0.5}\text{O}_2$. ZrO_2 transforms directly from the m- to the t-phase. Bi-axial stress in the ab-plane does not stabilize the f-phase regardless of stoichiometry and transforms directly from the m- to the t-phase as well.

5.4.4 Bi-axial Strain

Figure 5.9 depicts the parabolic regression curves for the enthalpy under bi-axial strain, plotted over the stress plane area A . Phase is marked by line color, stress plane by line type. Therefore, the results can be evaluated in terms of strain. Since the depicted data stems from stress calculations, strains are not uniform within all directions of the stress plane but rather inversely proportional to the corresponding E-module. The third lattice constant was able to relax freely. The calculation of the stress plane area assumed a (hypothetical) 12-atomic unit cell. Due to the large size of the unit cell of the m-phase, it is not possible to stabilize any other phase but the m-phase under expansion, regardless of stress plane and stoichiometry. Under compression, several other phases can be stabilized. Reducing the size of the ab-plane results in the stabilization of the o-phase. A further reduction results in the t-phase, particularly for ZrO_2 . Neither of the ferroelectric phases can be observed for this particular plane. The same is true for the ac-plane, but the enthalpy difference between the m- and f-phase becomes very small. Reducing the value of A in the bc-plane can result in the stabilization of the f-phase for all stoichiometries. When comparing the bi-axial results to the uni-axial results, the role of the c-axis in the stabilization of the f-phase is quite remarkable. Uni-axial strain in the a- or b-axis proved insufficient to allow ferroelectricity, however, strain in the c-axis was quite effective. In the bi-axial case, only strain conditions that involve the c-axis produce the f-phase. It is reasonable to assume that the observed effect comes mostly from the strained c-axis. For sufficiently small values of A_{bc} the tetragonal phase becomes energetically favorable compared to both the m- and f-phase.

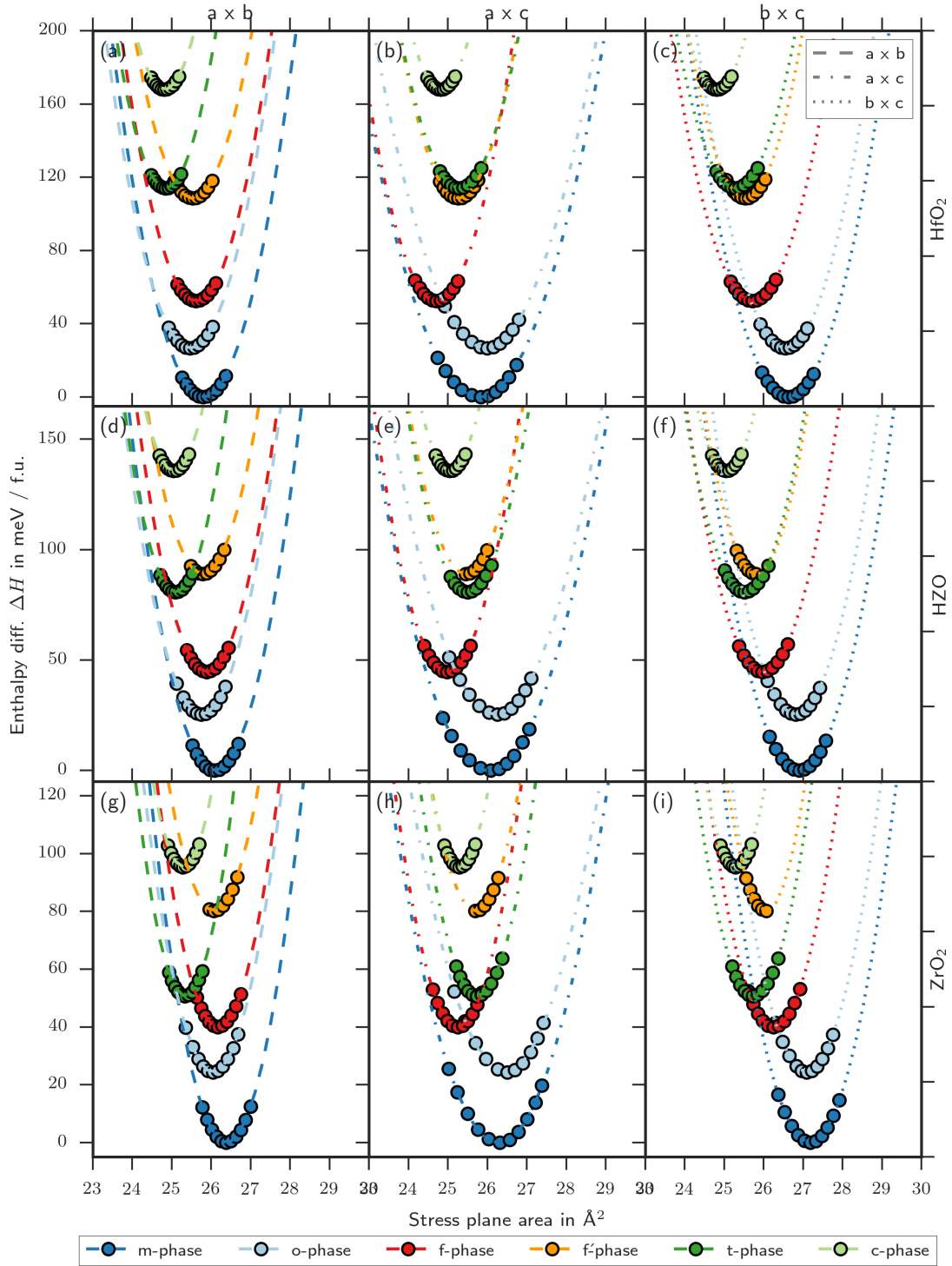


FIG. 5.9: Enthalpy as a function of lattice plane area. (a)-(c) HfO_2 , (d)-(f) $\text{Hf}_{0.5}\text{Zr}_{0.5}\text{O}_2$, and (g)-(i) ZrO_2 . Phase is marked by line color, strain plane by line type. The spatial orientation of polymorphs relative to each other is fixed, the various phases compete with each other based on the sensitivity of the enthalpy to strain in a given crystallographic plane.

5.4.5 Hydrostatic Stress

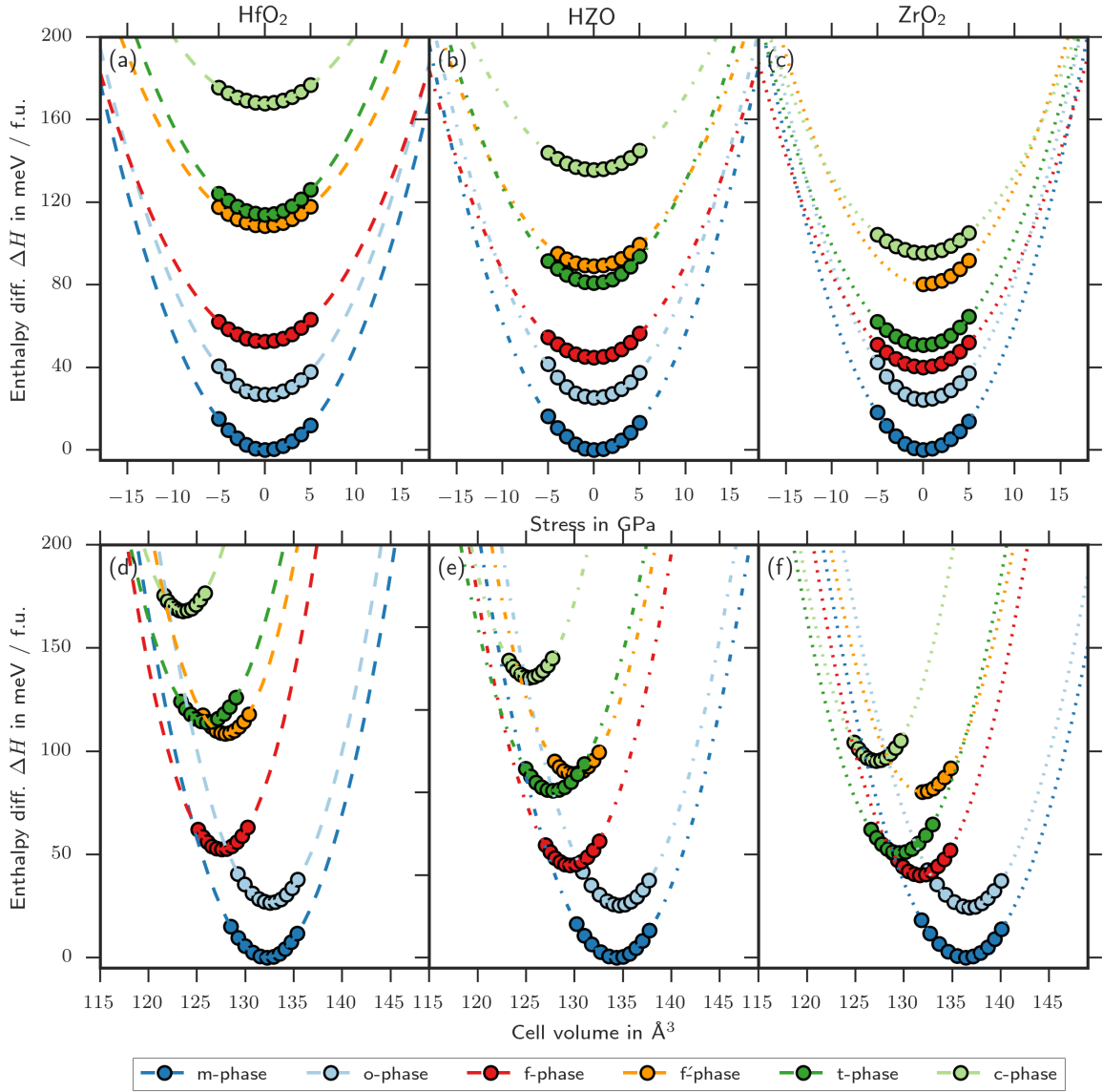


FIG. 5.10: Enthalpy as a function of hydrostatic stress for (a) HfO₂, (b) Hf_{0.5}Zr_{0.5}O₂, and (c) ZrO₂. Enthalpy as a function of cell volume for (d) HfO₂, (e) Hf_{0.5}Zr_{0.5}O₂, and (f) ZrO₂. Phase is marked by line color.

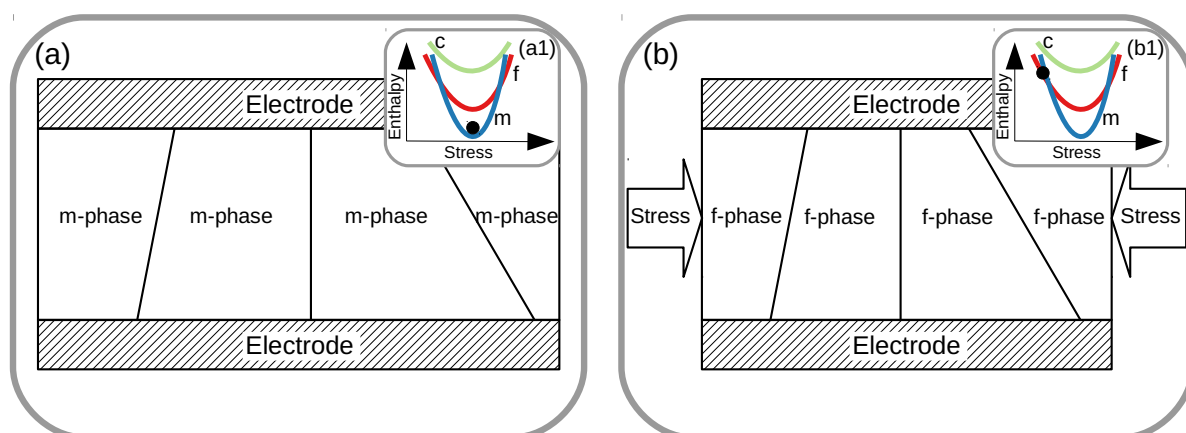
Figure 5.10 depicts the enthalpy plotted over hydrostatic stress for (a) HfO₂, (b) Hf_{0.5}Zr_{0.5}O₂, and (c) ZrO₂. Phase is marked by line color. The depicted results show no stabilization of the ferroelectric phase within the range of -18 GPa to 18 GPa for HfO₂. For Hf_{0.5}Zr_{0.5}O₂ and ZrO₂, the f-phase is stabilized around -15 GPa. Enthalpy plotted over the cell volume V_{12} is shown in (d) for HfO₂, in (e) for Hf_{0.5}Zr_{0.5}O₂, and in (f) for ZrO₂. Since the depicted data stems from stress calculations, strain is not uniform within all directions but rather inversely proportional to the corresponding E-module. Due to the different initial volumes of the different phases, small phases like the f- and t-phase have an advantage over the large m- and o-phase at small volumes. This opens up a possibility to stabilize the ferroelectric phase

with a strain constraint.

This idea is supported by an experimental observation, that the lattice constants of ferroelectric thin films often differ significantly from those expected from bulk phases. Particularly, the ratio of the lattice constants a and c are often found to be close to 1, while XRD shows a tetragonal or ferroelectric symmetry[163, 164]. This is often referred to as a "pseudo cubic phase". The correctness of the interpretation of the data has yet to be confirmed, but given the prospect of a possible explanation of ferroelectricity in the $\text{Hf}_{1-x}\text{Zr}_x\text{O}_2$ system, some speculations are in order.

Ostwald's step rule[165] states, that during a crystallization process it is usually the least stable polymorph, that crystallizes first. The most stable state is then reached by a series of phase transitions. While Ostwald's step rule is not a universal law but an often observed trend, there are some experimental observations that indicate that this rule applies to the $\text{Hf}_{1-x}\text{Zr}_x\text{O}_2$ system[163, 164]. This means that during the thermal annealing process after deposition, it is the c-phase that crystallizes first. The transition from the initial amorphous state into the c-phase is depicted in figure 5.11 (c) and (d). The cubic phase also happens to be the phase with the smallest cell volume as well as unit cell surface area. It may be the case, that these cubic crystallites fill the available space and thus determine the lattice constants and cell volume of the fully crystallized grains. These crystallites then transition into more stable phases of equal or similar physical dimension, particularly the t- and f-phase. Figure 5.11 (e) depicts the sample in the ferroelectric state. The change in enthalpy associated by the transition from the c- into the f-phase can be observed in the subplots (d1) and (e1). The t-phase is not depicted in figure 5.11 to aid the comprehensibility. The t-phase might occur either as an intermediate phase between the c- and the f-phase or it might occur instead of the f-phase. However, the transition into the more stable o- and m-phase could be prohibited, since these phases are large in comparison and are therefore strongly disadvantaged when compressed into constraints of a cubic cell as depicted in figure 5.11 (f) and (f1). Therefore, the thin film is strain constrained in the t- or f-phase without the appearance of stress. This sets this mechanism apart from stress stabilization, which assumes in contrast a monoclinic ground state (see figure 5.11 (a) and (a1)) which is then destabilized by an external stress condition in favor of another phase (see figure 5.11 (b) and (b1)). The existence of the strain effect means, that the history of a sample can also play an important role in the stabilization of the f-phase in the $\text{Hf}_{1-x}\text{Zr}_x\text{O}_2$ system.

Stress induced stabilization of the ferroelectric phase



Strain induced stabilization of the ferroelectric phase

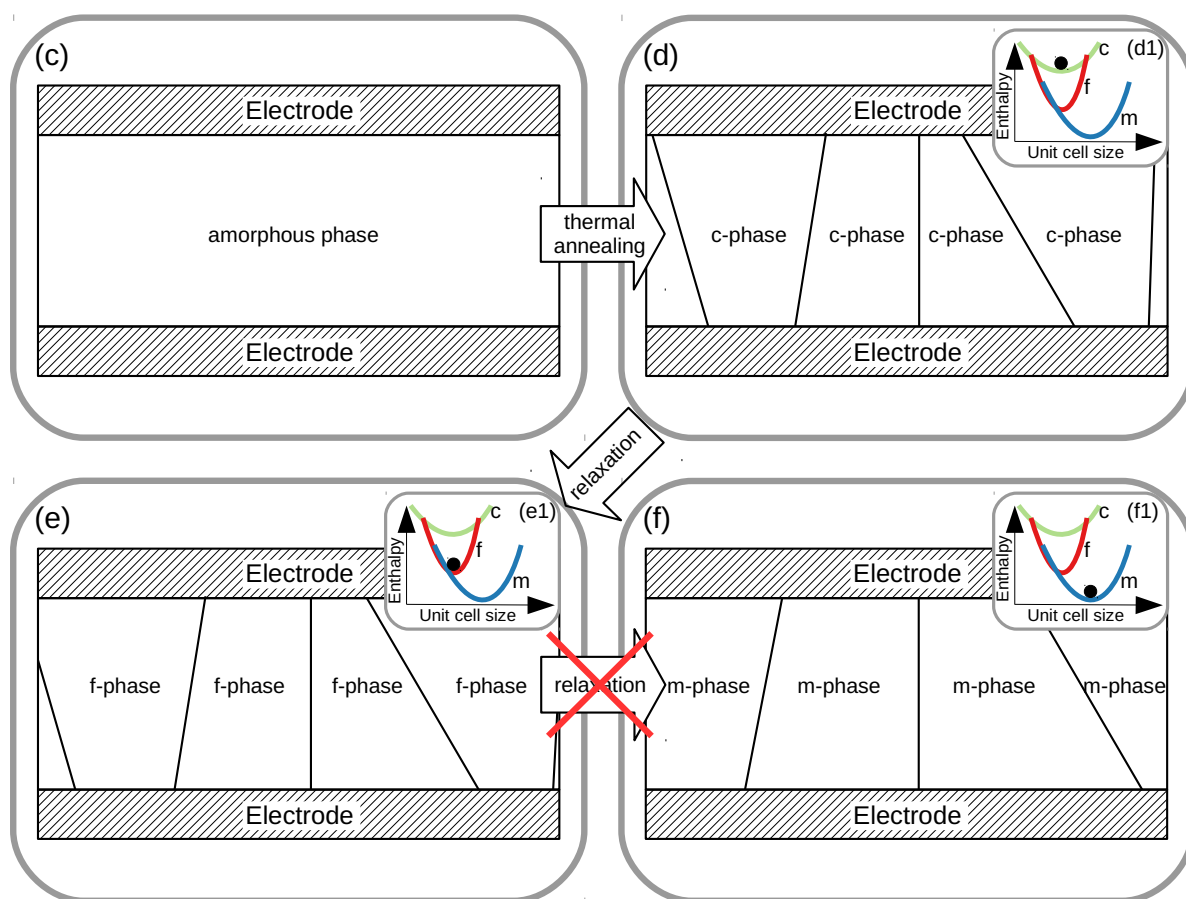


FIG. 5.11: Two possible mechanisms of stabilization of the ferroelectric phase in the $\text{Hf}_{1-x}\text{Zr}_x\text{O}_2$ system. (a) and (b) depicts the stabilization by stress with the associated energies depicted in (a1) and (b1). The strain effect is depicted in (c)-(f) with the associated energies in (d1), (e1) and (f1).

While this model is only hypothetical so far, there is some evidence for its validity.

1. The previously mentioned repeated observation of c/a ratio close to 1[163, 164].
2. The deposition of the top electrode **before** thermal annealing leads to a higher fraction of ferroelectric phase within the thin film, while deposition of the top electrode **after** thermal annealing leads to a higher fraction of monoclinic phase within the thin film[24, 166]. Therefore, the top electrode may help with the volume constriction of the thin film.
3. A recent observation, that reheating ferroelectric samples above the thermal annealing temperature over an extended period of time yields the monoclinic phase (while still at high temperature) at the cost of ferroelectric and tetragonal phase fractions, with a corresponding increase in lattice constants[167]. This observation is initially counter-intuitive, since one would expect the higher temperatures to be beneficial to the high-temperature phases t- and c-phase rather than the low-temperature m-phase. A possible explanation is, that the increase in temperature with the associated thermal expansion of the lattice results in the thin film overcoming the strain constraint due to processes like diffusion. This necessitates, that a significant fraction of f- and t-phase grains are metastable.

While this strain model has significant explanatory power, some critical points should be noted.

1. The results depicted in figure 5.10 (d)-(e) do not take into account the thermal expansion, particularly of the cubic phase. Therefore, the volume constraint may be much weaker than one might expect from figure 5.10. However, it should also be noted, that the thermal annealing temperature of the amorphous deposited film is in the range of 650 °C to 1000 °C, which is much lower than the liquid crystallization temperature. The thermal expansion is therefore also much lower than one might initially suspect.
2. The imperfect nature inherent in all DFT methods, and therefore also in the GBRV-LDA, may lead to an overestimation of the stabilizing effect of the volume constraint on the f-phase. Particularly the role of the o-phase is of concern. GBRV-LDA places the o-phase above the m-phase in terms of volume, while experiments place it below (see tables 5.1 to 5.3). The o-phase is also a known high-pressure phase, a fact reproduced by other DFT methods[47, 50], but not by GBRV-LDA. While the effect of the constrained lattice will definitely affect the energy balance of the ferroelectric phase in a favorable manner if experimentally realized, it might not be enough to explain the observed ferroelectricity in $\text{Hf}_{1-x}\text{Zr}_x\text{O}_2$ on its own. Additional effects may be necessary to do so. These effects may include the grain size effect, dopants or effects from electric field cycling.

To summarize the section on stress and strain effects, the following statements should be noted. While it is possible to stabilize the f-phase with stress, this usually requires stress conditions >10 GPa. Stress seems therefore to be a possible but unrealistic explanation for the observed ferroelectricity, as such large values should surely have been noted within the

literature. Values from wafer bow measurements or other methods indicate stress values in the range of 1 GPa to 2 GPa tensile stress[143], which is absolutely insufficient. A more promising explanation are strains, particularly volumetric strain and strains constricting the c-axis. A scenario was developed in this section, which requires a kinetic model for the sequence of phase transitions which explains the stabilization of the f-phase with a volume constriction. However, it is inaccurate to describe a so stabilized phase as stress stabilized. Only a hypothetical m-phase, trying to fit within the volume constraints would be subject to high stresses, the actual f-phase may only experience a small amount of stress due to its smaller initial volume.

5.5 Grain Size and Interface Energy

The next effect under investigation is the grain size effect, which will be considered to be caused by the interface energy between a bulk phase and a tetragonal surface layer within grains as described in section 4.2. For a given film thickness, the results of this model can be plotted as a phase diagram, where phase is indicated as a function of both grain radius and stoichiometry. The model parameter "film thickness" is used to generate grain size distribution functions as described in section 4.3. Shape parameters and the scale function of the distribution function were fitted to data from Park et al.[143], as were the values for the specific interface energy. In the following several films with the stoichiometries HfO_2 , $\text{Hf}_{0.5}\text{Zr}_{0.5}\text{O}_2$, and ZrO_2 are investigated. Figure 5.12 shows the volumetric grain size distribution for (a) 7 nm and (b) 10 nm thick HfO_2 films. The corresponding phase diagrams for these film thicknesses are depicted in figure 5.12 (c) and (d).

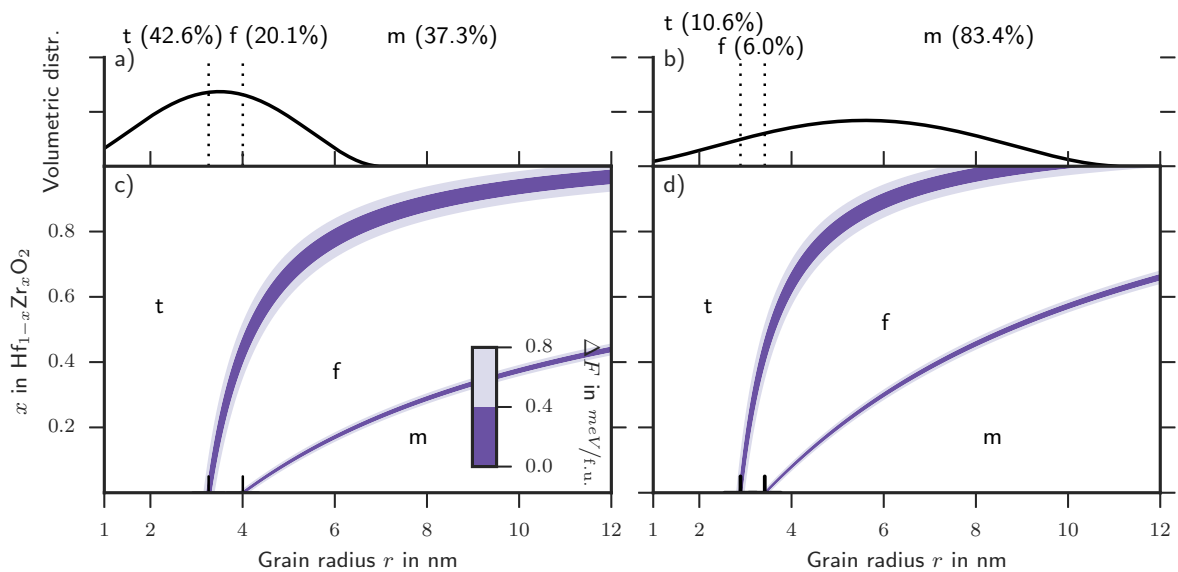


FIG. 5.12: Grain size distribution of (a) 7 nm and (b) 10 nm HfO_2 films, with the corresponding phase diagram below in (c) and (d).

The phase diagrams show, that the f-phase forms as an intermediate of the m- and t-phase, where the former is dominant in the Hf-rich domain and at larger grain radii, while the latter dominates in the Zr-rich region and smaller grains. The grain radius range, in which grains become ferroelectric depends on the stoichiometry of the grain. For the selected film thicknesses, the ferroelectric window is very small for pure HfO₂ and widens with increasing Zr content. Comparing the subplots (c) and (d) it becomes apparent, that the exact values for the ferroelectric grain radius range also depends on film thickness, as the model is sensitive to the surface to volume ratio. The phase fraction of a thin film can be determined by projection of the phase boundaries for a selected stoichiometry onto the grain radius distributions depicted in subplots (a) and (b). This means, that about 20 % by volume of the 7 nm pure HfO₂ film is ferroelectric. In the 10 nm film, only 6 % by volume are ferroelectric. This is consistent with experimental results [82] who found ferroelectricity in 6 nm to 8 nm thick pure HfO₂ films, but not in 10 nm films. The shaded areas indicate energy differences between adjacent phases, therefore the broadness of the shaded areas is an indicator for the gradient of the energy landscape. The gradient between the t- and f-phase is much smaller than between the m- and the f-phase. This means, that small changes in energy, caused for example by an external electric field or the amplification of stress may cause some grains to transform from the t-phase into the f-phase and vice versa. Due to the steep gradient in the energy landscape, much fewer grains are able to transform from the m-phase into the f-phase. Figure 5.13 shows the volumetric grain size distribution for (a) 20 nm and (b) 40 nm thick Hf_{0.5}Zr_{0.5}O₂ films in an effort to comprehend experimental data by Kim et al[79], who was able to mitigate the thickness dependence of the ferroelectric properties of ALD deposited Hf_{0.5}Zr_{0.5}O₂ by introducing a 1 nm thick Al₂O₃ interlayer. Without these interlayers, Kim et al. observed a decrease of the remanent polarization with increasing film thickness, whereby at a film thickness of 40 nm no ferroelectricity could be observed. The introduction of this interlayer halfway through the film inhibited grain growth and therefore maintained the ferroelectric polarization. The interface model predicts a volume fraction of 16 % ferroelectric grains within a 20 nm thin Hf_{0.5}Zr_{0.5}O₂ film, and therefore a measurable albeit decreased remanent polarization. For the 40 nm thin films the model predicts a ferroelectric phase fraction of only 2.3 % by volume, and therefore a negligible remanent polarization.

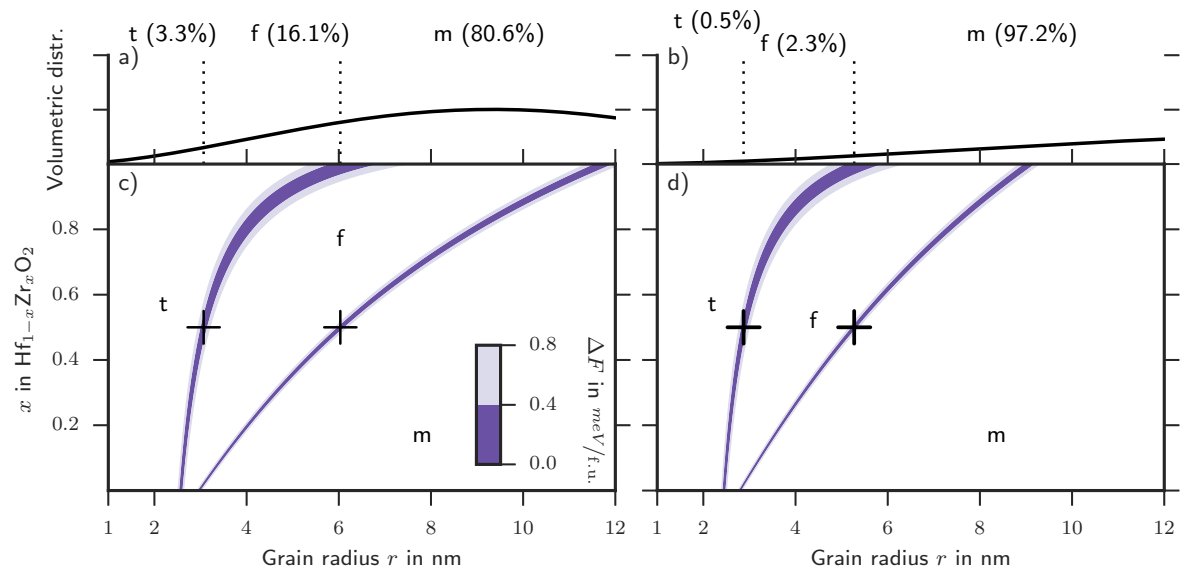


FIG. 5.13: Grain size distribution of (a) 20 nm and (b) 40 nm $\text{Hf}_{1-x}\text{Zr}_x\text{O}_2$ films, with the corresponding phase diagram below in (c) and (d).

As shown in this section, the interface model is able to replicate experimental results in at least a qualitative manner. However, exact numerical precision may depend on the chosen DFT method.

5.6 Interim Conclusion

This work so far has looked at stoichiometry, temperature, stress, strain, and grain size coupled with an interface energy as possible mechanisms for stabilizing ferroelectricity in the $\text{Hf}_{1-x}\text{Zr}_x\text{O}_2$ system. Stoichiometry alone proved insufficient to explain the observed behavior, as the total energy of ferroelectric phases never comes below the total energy on the non-ferroelectric m- or o-phase for either stoichiometry. Temperature was only able to promote the known high-temperature t-phase. Stress was found a possible stabilization mechanism, particularly when the stressed axis includes the c-axis. However, the necessary stress values are in the range of 10 GPa or higher, which should be experimentally observable as a significant wafer bow. According to the author's knowledge, no such observations exist. Since this is not the case, stress should not be considered to be responsible for the stabilization of the f-phase. Strain, on the other hand proved, quite effective in stabilizing the f-phase, particularly bi-axial strain in the bc-plane as well as tri-axial strain. In this section, a hypothesis applying Ostwald's step rule was formulated, explaining how such strain conditions could be produced within a thin film. Experimental observations from the literature in support of this hypothesis were presented. This effect can contribute in a favorable way to the stabilization of the f-phase if realized in experiments. DFT calculation fine-tuned for stress calculations as well as calculations considering anisotropic stress and strain may further improve this model in the future. Another effect capable of explaining the ferroelectric stabilization is the influence of the grain size in combination with an interface energy effect between the bulk of a grain and its tetragonal interlayer. A quasi-empiric model, using DFT values where possible, was described. This model was able to reproduce experimental observations. A combined model, including both the strain effect and the grain size effect, may be able to reproduce experimental results in $\text{Hf}_{1-x}\text{Zr}_x\text{O}_2$ to a high degree of accuracy.

5.7 Dopants and Defects

So far the focus of this work was on perfect crystals of $\text{Hf}_{1-x}\text{Zr}_x\text{O}_2$ under some sort of external influence and how these influences affect the phase stability of the f-phase. In the following subchapter, the focus will be on the role of dopants and other defects of the crystal lattice and how they influence the phase stability of ferroelectric HfO_2 . The high doping concentration necessary for ferroelectricity requires charge neutrality of the defects, otherwise, the resulting charge density would be enormous in the range of $10 \times 10^{21} \text{ 1/cm}^3$. Therefore, electronically compensated, ionically compensated, and mixed compensated defects are investigated in this section. A detailed description of these defects can be found in the method section 3.3.1 of this work. Selected parts of the data presented here has also been published in Applied Physics Letters [168] and the Journal of Applied Physics [169]. Further information can also be found in Falkowski et al.[170]

5.7.1 Vacancies and Interstitials

Figure 5.14 depicts the influence of the (a) V_O and (b) O_I defects on the total energy differences U_0 between the various HfO_2 polymorphs and the m-phase.⁴ The associated formation energies are depicted in (c).

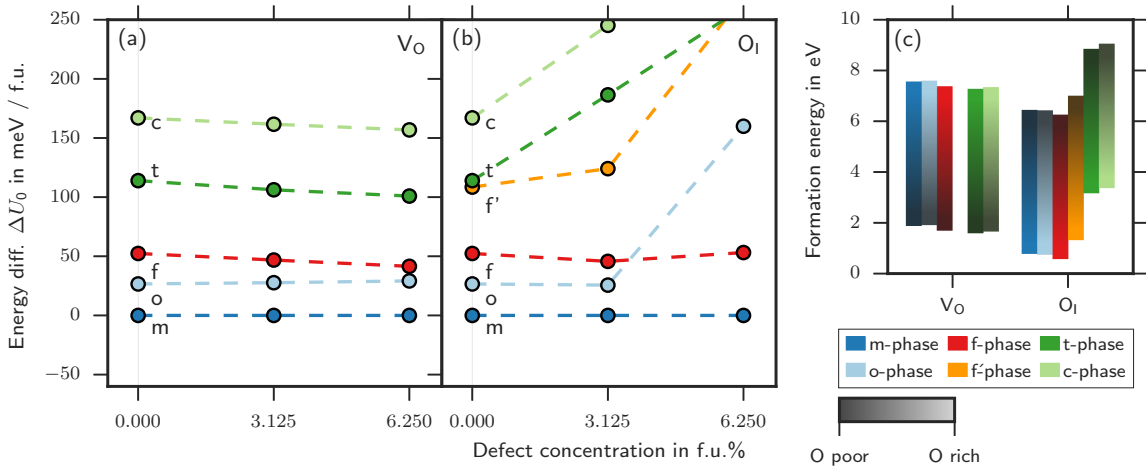


FIG. 5.14: Effect of oxygen vacancies (a) and interstitials (b) on the total energy difference ΔU_0 of the various HfO_2 polymorphs compared to the m-phase. Subplot (c) shows the formation energy of those defects as a function of the oxygen chemical potential with the light color representing oxygen-rich and the dark color oxygen-poor conditions.

The effect of oxygen vacancies on the total energy U_0 of otherwise pure HfO_2 is small within the concentration range from 0 f.u.% to 6.25 f.u.%. The f-, t-, and c-phase profit only

⁴The data points for a dopant concentration of 6.25 f.u.% are calculated with a 48-atomic supercell. There are up to 3 different possibilities (orientations) to construct a 48-atomic supercell: $2 \times 2 \times 1$, $2 \times 1 \times 2$, and $1 \times 2 \times 2$. The depicted data for the O_I defect is the average of those three orientations. The depicted data for the V_O defect is for the $2 \times 1 \times 2$ only due to the associated calculation effort necessary to calculate all 3 orientations for all vacancy positions.

slightly in comparison to the m- and o-phase. In comparison, the effect of interstitial oxygen is more pronounced. The f-phase is the only phase, that slightly decreases in total energy in comparison to the m-phase. All other phases increase significantly in total energy. The formation energy of both defects is positive for all values of the oxygen chemical potential, meaning their creation requires energy. As one would suspect, the trend of the formation energy as a function of the oxygen chemical potential is reversed between the two dopants. Oxygen vacancies have the lowest formation energy at oxygen-poor conditions, while oxygen interstitials are particularly favorable at oxygen-rich conditions.

5.7.2 Sr-Doping

Figure 5.15 depicts the influence of the (a) Sr_{Hf} and (b) $\text{Sr}_{\text{Hf}}\text{V}_{\text{O}}$ defects on the total energy differences U_0 between the various HfO_2 polymorphs and the m-phase.⁵ The associated formation energies are depicted in (c).

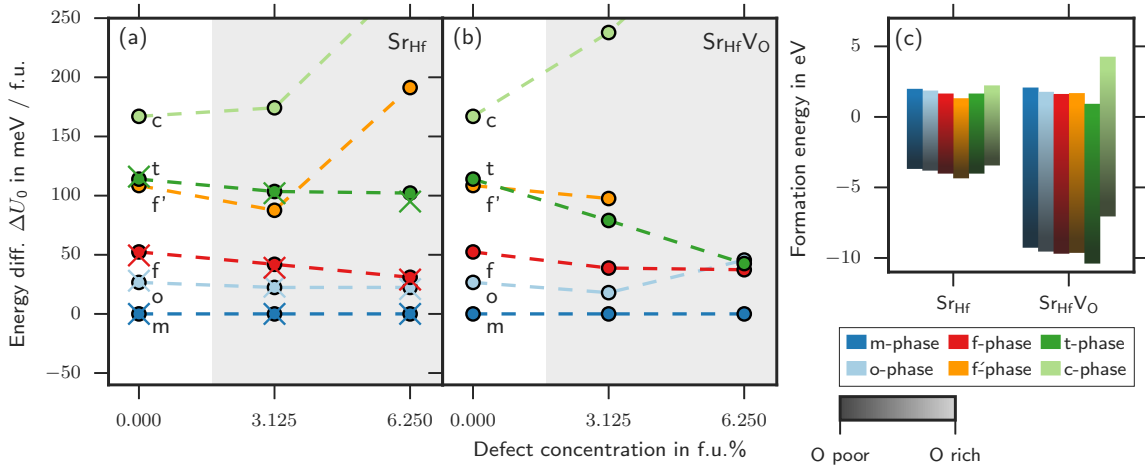


FIG. 5.15: Effect of Sr-doping on the total energy difference ΔU_0 of the various HfO_2 polymorphs compared to the m-phase. The defects are (a) Sr_{Hf} and (b) $\text{Sr}_{\text{Hf}}\text{V}_{\text{O}}$. Subplot (c) shows the formation energy of those defects as a function of the oxygen chemical potential with the light color representing oxygen-rich and the dark color oxygen-poor conditions. The dopant concentration range for which ferroelectricity was experimentally observed (ALD and CSD) is highlighted in grey.

The o-phase does not react significantly to the presence of Sr_{Hf} defects over the investigated concentration range. However, in $\text{Sr}_{\text{Hf}}\text{V}_{\text{O}}$ doped HfO_2 , there is a small non-linear effect on the total energy of the o-phase. The f-phase is favored by Sr-doping in general, but the effect is more pronounced for the Sr_{Hf} defect than the $\text{Sr}_{\text{Hf}}\text{V}_{\text{O}}$ defect. The Sr_{Hf} defect leads to a reduction in the total energy difference from 52.38 meV to 27.74 meV at a doping

⁵The data points for a dopant concentration of 6.25 f.u.% are calculated with a 48-atomic supercell. There are up to 3 different possibilities (orientations) to construct a 48-atomic supercell: $2 \times 2 \times 1$, $2 \times 1 \times 2$, and $1 \times 2 \times 2$. The depicted data for the Sr_{Hf} defect is the average of those three orientations. The depicted data for the $\text{Sr}_{\text{Hf}}\text{V}_{\text{O}}$ defect is for the $2 \times 1 \times 2$ only due to the associated calculation effort necessary to calculate all 3 orientations for all vacancy positions. All other dopants are treated in the same manner.

concentration of 6.25 f.u. % compared to the m-phase. However, the effect is too small to explain the observed ferroelectric process window on its own. Additional effects like interface and surface energy, or entropy are necessary to explain the stabilization of the f-phase. The f-phase is not only in competition with the m- and o-phase, but also with the energetically less favorable t-phase. In particular, this is the case for the $\text{Sr}_{\text{Hf}}\text{V}_\text{O}$ defect, where the total energy difference of the t-phase drops from originally 113.95 meV to 42.51 meV at 6.25 f.u. % doping concentration and is therefore on par with the f-phase. This limits the ferroelectric process window significantly to below 6.25 f.u. %, particularly when taking the free energy into account as well. This is in contrast with experimental results which find the upper edge of the ferroelectric process window at 7.9 mol % for ALD layers[60] and at 15 mol % for CSD layers[59]. The stabilizing effect on the t-phase is much weaker for the Sr_{Hf} defect, which suggests that Sr-doped ferroelectric HfO_2 thin films predominantly contain Sr_{Hf} defects rather than $\text{Sr}_{\text{Hf}}\text{V}_\text{O}$ defects. The f'-phase is destabilized by the Sr_{Hf} defect, but declines in total energy when doped with the $\text{Sr}_{\text{Hf}}\text{V}_\text{O}$ defect. The c-phase raises strongly in total energy by either defect and is therefore strongly destabilized.

Figure 5.15 (a) and (b) contain results from ABINIT (O-symbol) and FHI-AIMS (X-symbol). Both methods produce consistent results, therefore validating our choice of pseudopotentials.

The formation energies of the Sr_{Hf} and $\text{Sr}_{\text{Hf}}\text{V}_\text{O}$ defects are depicted in figure 5.15 (c) as a function of the oxygen chemical potential for all six phases. The underlying DFT calculations were performed in charge neutral 96-atomic supercells. In the oxygen-rich case, both defects are roughly equal in formation energy. There is a small dependency on the phase determining which defect is favored. The Sr_{Hf} defect is favored over the $\text{Sr}_{\text{Hf}}\text{V}_\text{O}$ defect in the f- and f'-phase, while the opposite is true for the t-phase. oxygen-poor conditions strongly favor the $\text{Sr}_{\text{Hf}}\text{V}_\text{O}$ defect over the Sr_{Hf} defect in all phases.

In conclusion, Sr-doping stabilizes the f-phase in Sr-doped HfO_2 . The effect is small compared to the energy difference between the m- and the f-phase. Other effects are therefore needed in addition to doping in order to explain the observed ferroelectricity. One such effect might be the grain size effect caused by an interface energy. Regardless, the competing t-phase is stabilized by Sr-doping as well. Sr_{Hf} defects favor the f-phase more than the t-phase. However, $\text{Sr}_{\text{Hf}}\text{V}_\text{O}$ defects favor the t-phase much more than the f-phase. This causes the total energy of the t-phase to become lower than the total energy of the f-phase within the observed ferroelectric process window, therefore prohibiting ferroelectricity. The energetic equivalency of the f- and t-phase would also suggest field-induced ferroelectric behavior, which has not been observed in experiments. From this discrepancy, it follows, that the observed ferroelectricity must be caused by the Sr_{Hf} defect. This, however, requires that the manufacture of ferroelectric thin films occurs at oxygen-rich conditions.

5.7.3 Be-Doping

Figure 5.16 depicts the influence of the (a) Be_{Hf} and (b) $\text{Be}_{\text{Hf}}\text{V}_\text{O}$ defects on the total energy differences U_0 between the various HfO_2 polymorphs and the m-phase. The associated formation energies are depicted in (c).

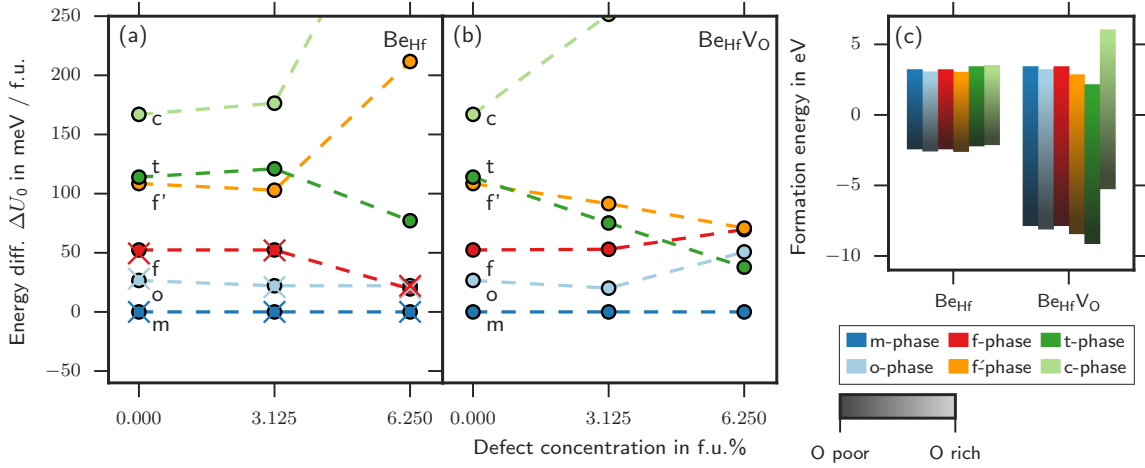


FIG. 5.16: Effect of Be-doping on the total energy difference ΔU_0 of the various HfO_2 polymorphs compared to the m-phase. The defects are (a) Be_{Hf} and (b) $\text{Be}_{\text{Hf}}\text{V}_\text{O}$. Subplot (c) shows the formation energy of those defects as a function of the oxygen chemical potential with the light color representing oxygen-rich and the dark color oxygen-poor conditions.

The o-phase does not react significantly to the presence of Be_{Hf} defects over the investigated concentration range, in $\text{Be}_{\text{Hf}}\text{V}_\text{O}$ doped HfO_2 there is a small non-linear effect on the total energy. The total energy of the f-phase remains constant between 0 f.u.% and 3.125 f.u.% Be_{Hf} , for a larger dopant concentration, a significant drop from 52.39 meV to 19.42 meV can be observed. This makes Be-doping a candidate for stabilizing ferroelectricity in HfO_2 . However, with an associated vacancy the stabilizing effect disappears. The f'-phase behaves in an opposite manner to the f-phase. A strong increase in total energy is observed for dopant concentrations above 3.125 f.u.% for the Be_{Hf} defect. The $\text{Be}_{\text{Hf}}\text{V}_\text{O}$ defect leads to a decrease in total energy, however, this effect is too small to compete with the t-phase. The c-phase shows a strong increase in total energy for both kinds of defects. Based on the depicted data, Be_{Hf} -doped HfO_2 should be ferroelectric, $\text{Be}_{\text{Hf}}\text{V}_\text{O}$ -doped HfO_2 should be tetragonal. Due to the small size of the Be atom, Be might be incorporated on an interstitial position into HfO_2 . However, interstitial doping has not been evaluated for Be in this work. The formation energies depicted in (c) show a weak dependency of the formation energy of the Be_{Hf} defect from the phase. In contrast, the $\text{Be}_{\text{Hf}}\text{V}_\text{O}$ defect requires a particularly low formation energy in the t-phase and a particularly high formation energy in the c-phase. Comparing the formation energies of the two types of defects with each other leads to the conclusion, that the incorporation of Be in HfO_2 likely leads to the formation of $\text{Be}_{\text{Hf}}\text{V}_\text{O}$ -doped t-phase HfO_2 since this defect has the lowest of all formation energies, even under oxygen-rich conditions.

The formation energies of the other phases, with exception of the c-phase, vary only slightly between the two defect types for oxygen-rich conditions. At oxygen-poor conditions, the $\text{Be}_{\text{Hf}}\text{V}_\text{O}$ defect is as expected clearly favored over Be_{Hf} . In conclusion, the effect of the Be_{Hf} defect on the total energy of the f-phase makes Be-doping initially a promising candidate for ferroelectric HfO_2 . However, the low formation energy of the $\text{Be}_{\text{Hf}}\text{V}_\text{O}$ in t-phase HfO_2 likely causes the material to stabilize in the tetragonal configuration.

5.7.4 Mg-Doping

Figure 5.17 depicts the influence of the (a) Mg_{Hf} and (b) $\text{Mg}_{\text{Hf}}\text{V}_\text{O}$ defects on the total energy differences U_0 between the various HfO_2 polymorphs and the m-phase. The associated formation energies are depicted in (c).

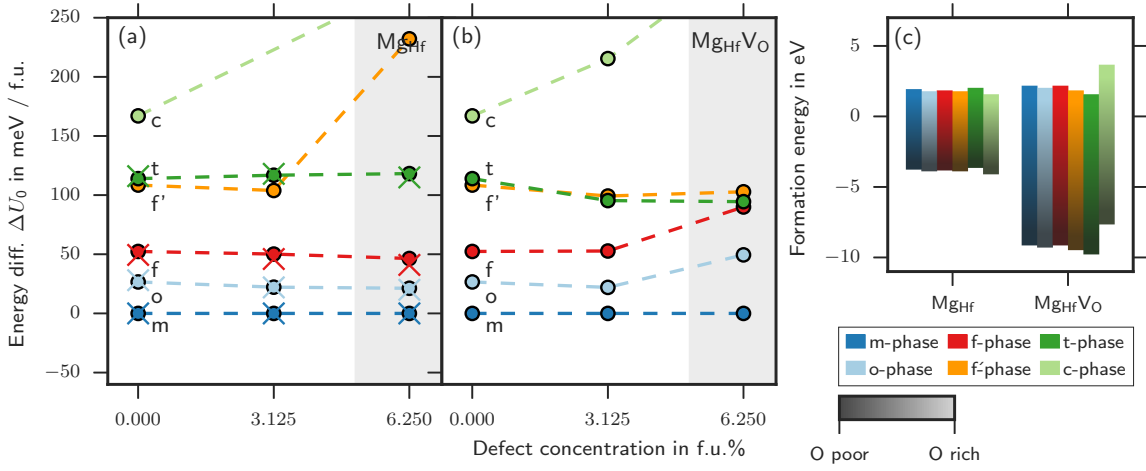


FIG. 5.17: Effect of Mg-doping on the total energy difference ΔU_0 of the various HfO_2 polymorphs compared to the m-phase. The defects are (a) Mg_{Hf} and (b) $\text{Mg}_{\text{Hf}}\text{V}_\text{O}$. Subplot (c) shows the formation energy of those defects as a function of the oxygen chemical potential with the light color representing oxygen-rich and the dark color oxygen-poor conditions. The dopant concentration range for which ferroelectricity was experimentally observed (ALD and CSD) is highlighted in grey.

The depicted results in Fig. 5.17 show, that Mg-doping of HfO_2 does not lead to the stabilization of any phase other than the m-phase. This is true for both the Mg_{Hf} - and the $\text{Mg}_{\text{Hf}}\text{V}_\text{O}$ defects. For the Mg_{Hf} defect, the total energy differences of the o-, f-, and the t-phase remain constant in respect to the m-phase, regardless of doping concentration. The f'- and c-phase show a significant increase in total energy for a doping concentration of 6.25 f.u.%. The $\text{Mg}_{\text{Hf}}\text{V}_\text{O}$ defect causes a slight increase in total energy for the o- and f-phase and a slight decrease for the f'- and t-phase. The c-phase retains the strong increase in total energy. The near constant energy difference between the f- and t-phase in respect to the m-phase is unique to Mg-doping, as these two phases usually display a stronger change in total energy when doped. This trend can also be observed in the FHI-AIMS results. An explanation of this behavior might be found in the atomic/ionic radii of Hf and Mg, which are almost identical

for both elements. Hf has an ionic radius of 58 pm for $\text{Hf}^{+4}(\text{IV})$ and 83 pm for $\text{Hf}^{+4}(\text{VIII})$ [38]. The corresponding values for Mg^{+2} are 57 pm and 89 pm [38]. Why ferroelectricity was observed in CSD deposited Mg-doped HfO_2 by Starschich et al. [59] remains unanswered in light of the results presented here.

Since the c-phase of the 3.125 f.u.% Mg_{Hf} structure transformed into the tetragonal phase, the formation energy was interpolated from 0 f.u.% and 6.25 f.u.% dopant concentration. The formation energy varies little with phase with the exception of the c-phase, where Mg related defects have a higher formation energy. For oxygen-rich conditions, the Mg_{Hf} defect is slightly favored over the $\text{Mg}_{\text{Hf}}\text{V}_\text{O}$ defect, for oxygen-poor conditions the $\text{Mg}_{\text{Hf}}\text{V}_\text{O}$ defect dominates.

To summarize the results for Mg-doping, Mg related defects do not significantly alter the energy differences between the various polymorphs, with the exception of the f'- and c-phase phase. They are destabilized by a significant increase in total energy. Therefore, no phase transitions are expected to occur from doping. This is true for both ABINIT and FHI-AIMS calculations. This unique behavior of Mg-doped Hf might be related to the almost identical size of both the Mg and Hf ions. The experimentally observed ferroelectricity by Starschich et al. [59] can therefore not be explained by the ab initio calculations presented here. A possible solution for this conundrum might be, that Mg changes the crystallization properties of the doped HfO_2 and that the ferroelectricity is caused by a size effect.

5.7.5 Ca-Doping

Figure 5.18 depicts the influence of the (a) Ca_{Hf} and (b) $\text{Ca}_{\text{Hf}}\text{V}_\text{O}$ defects on the total energy differences U_0 between the various HfO_2 polymorphs and the m-phase. The associated formation energies are depicted in (c).

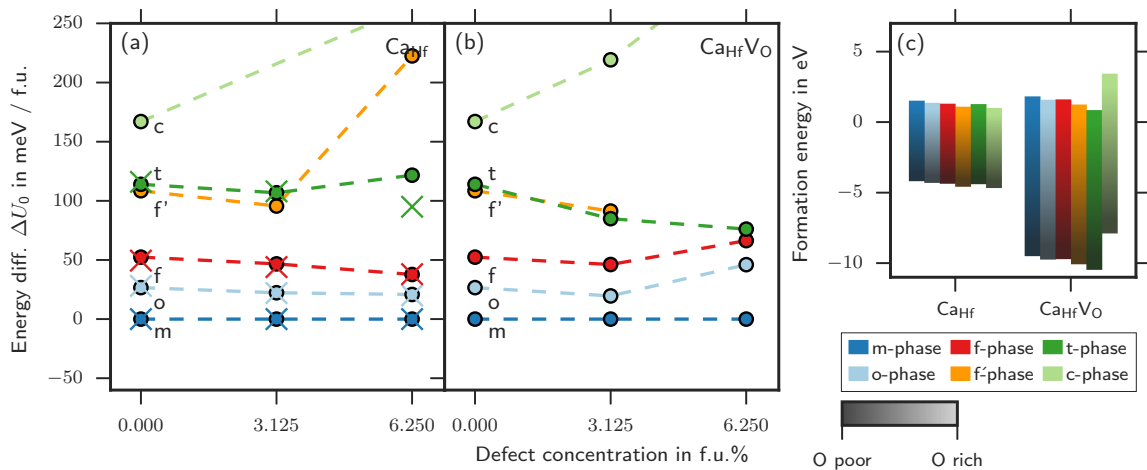


FIG. 5.18: Effect of Ca-doping on the total energy difference ΔU_0 of the various HfO_2 polymorphs compared to the m-phase. The defects are (a) Ca_{Hf} and (b) $\text{Ca}_{\text{Hf}}\text{V}_\text{O}$. Subplot (c) shows the formation energy of those defects as a function of the oxygen chemical potential with the light color representing oxygen-rich and the dark color oxygen-poor conditions.

The Ca_{Hf} defect causes the o- and f-phase to slightly decline in total energy relative to the monoclinic ground state phase. The f'-phase declines at first as well, but increases in total energy at a doping concentration of 6.25 f.u.%. The total energy of the t-phase remains largely unaffected by the Ca_{Hf} defect, while the c-phase shows a strong increase in total energy for both the Ca_{Hf} and $\text{Ca}_{\text{Hf}}\text{V}_{\text{O}}$ defect. For $\text{Ca}_{\text{Hf}}\text{V}_{\text{O}}$ -doped HfO_2 , a small upward trend can be observed for the o- and f-phase. However, the f'- and t-phase experience a significant drop in total energy due to the presence of the $\text{Ca}_{\text{Hf}}\text{V}_{\text{O}}$ defect. Unfortunately, the CSD study on the effects of dopants on the ferroelectric properties of HfO_2 by Starschich et al.[59] did not include Ca. The ferroelectric properties of Ca-doped HfO_2 are therefore not known and can not be compared to the ab initio results. Given the results presented here, it may seem unlikely that Ca-doped HfO_2 can become ferroelectric as the f-phase experiences only a very small drop in total energy of 14.7 meV at a Ca_{Hf} -doping concentration of 6.25 f.u.% and an overall increase in total energy from $\text{Ca}_{\text{Hf}}\text{V}_{\text{O}}$ -doping. However, Mg-doped HfO_2 was found to be ferroelectric[59] for reasons yet unknown even though the ab initio energies were less favorable for the f-phase than it is the case for Ca-doped HfO_2 . Therefore, given the chemical similarities between Mg and Ca, ferroelectricity of Ca-doped HfO_2 cannot be ruled out from the ab initio data presented here.

Since the c-phase of the 3.125 f.u.% Ca_{Hf} structure transformed into the tetragonal phase, the formation energy was interpolated from 0 f.u.% and 6.25 f.u.% dopant concentration. The formation energies depicted in (c) indicate that the $\text{Ca}_{\text{Hf}}\text{V}_{\text{O}}$ defect dominates at oxygen-poor conditions, while the Ca_{Hf} defect is favored at oxygen-rich conditions. This, in combination with the decline in total energy of the f-phase caused by the Ca_{Hf} defect, should make Ca a more viable dopant for ferroelectricity than Mg, unfortunately, no experimental data exist for this dopant to support this claim. Regardless, Sr seems to be superior to either dopant.

5.7.6 Ba-Doping

Figure 5.19 depicts the influence of the (a) Ba_{Hf} and (b) $\text{Ba}_{\text{Hf}}\text{V}_{\text{O}}$ defects on the total energy differences U_0 between the various HfO_2 polymorphs and the m-phase. The associated formation energies are depicted in (c).

The behavior of Ba-doped HfO_2 is different from HfO_2 doped with other II-valent dopants, particularly when it comes to the o-phase. The Be_{Hf} defect causes a significant drop in total energy of o-phase HfO_2 . As a result, the m- and o-phase become energetically indistinguishable. This, however, is not caused by a phase transition, as most ions in the converged supercells keep their original orthorhombic positions. Ions in close proximity to the dopant do experience some lattice deformation, but the o-phase structure remains intact. The same type of defect was unable to affect the o-phase for other II-valent dopants. The presence of an oxygen vacancy negates the effect and the o-phase behaves as it did for the other II-valent

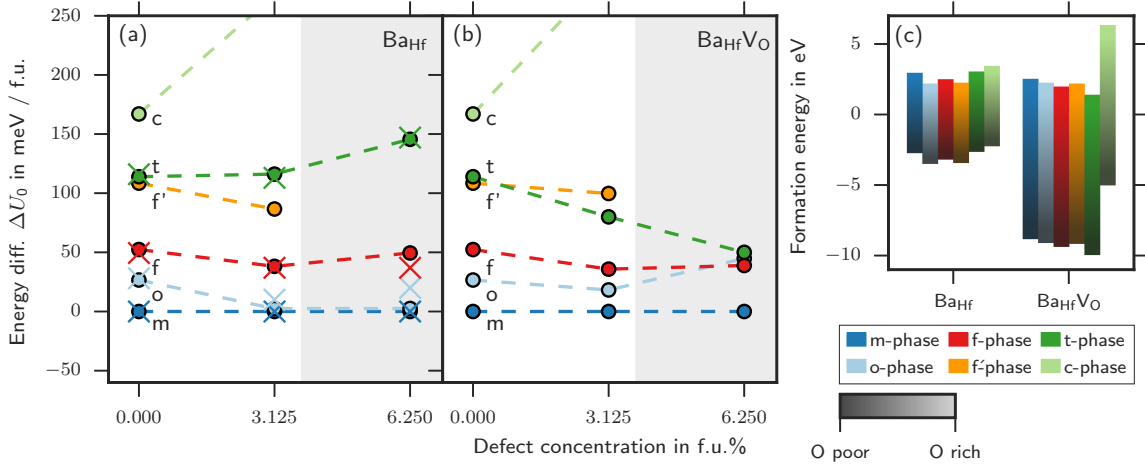


FIG. 5.19: Effect of Ba-doping on the total energy difference ΔU_0 of the various HfO_2 polymorphs compared to the m-phase. The defects are (a) Ba_{Hf} and (b) Ba_{HfV_O} . Subplot (c) shows the formation energy of those defects as a function of the oxygen chemical potential with the light color representing oxygen-rich and the dark color oxygen-poor conditions. The dopant concentration range for which ferroelectricity was experimentally observed (ALD and CSD) is highlighted in grey.

dopants. The f-phase experiences a minor drop in total energy from originally 52.38 meV to 49.43 meV at a Ba_{Hf} -doping concentration of 6.25 f.u.%. The behavior is basically identical with an oxygen vacancy. The f'-phase also experiences a drop in total energy for both types of defects, however, the effect is more pronounced in Ba_{Hf} -doped HfO_2 than in Ba_{HfV_O} -doped HfO_2 . The t-phase energy increases slightly for the Ba_{Hf} defect but decreases for Ba_{HfV_O} defects. At a doping concentration of 6.25 f.u.% the total energies of the t- and f-phase are almost equal. Therefore, the presence of vacancies inhibits ferroelectricity. This is in contrast to the observed ferroelectric window from 3.75 f.u.% to 11 f.u.%[59]. This indicates that the observed ferroelectricity is caused by the Ba_{Hf} defect instead. Similar to the other II-valent dopants, the c-phase is strongly disadvantaged by a strong increase in total energy for both kinds of defects.

The formation energies depicted in (c) seem to slightly favor the Ba_{HfV_O} defect under oxygen-rich and poor conditions for most phases. Exceptions are the o-phase and f'-phase, which favor the Ba_{Hf} defect at oxygen-rich conditions. Given, that the Ba_{HfV_O} defect strongly favors the t-phase, the observed ferroelectricity might be caused by the f'-phase, which would single out Ba from other II-valent dopants.

5.7.7 Al-Doping

Figure 5.20 depicts the influence of the (a) Al_{Hf} , (b) Al_{HfV_O} , and (c) $(2\text{Al}_{\text{Hf}})\text{V}_O$ defects on the total energy differences U_0 between the various HfO_2 polymorphs and the m-phase. The associated formation energies are depicted in (d).

The most noticeable feature of Al-doped HfO_2 is the strong stabilization of the t-phase

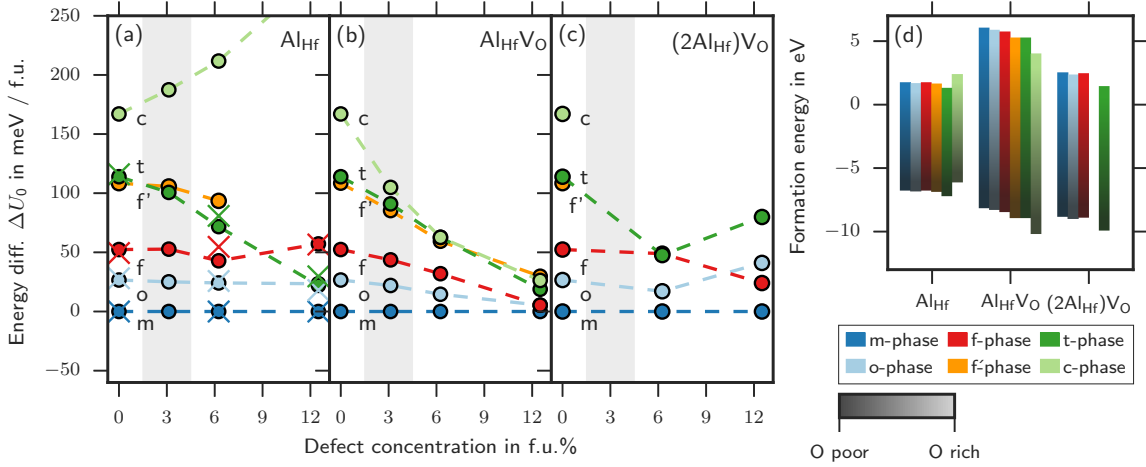


FIG. 5.20: Effect of Al-doping on the total energy difference ΔU_0 of the various HfO_2 polymorphs compared to the m-phase. The defects are (a) Al_{Hf} , (b) $\text{Al}_{\text{Hf}}\text{V}_{\text{O}}$, and (c) $(2\text{Al}_{\text{Hf}})\text{V}_{\text{O}}$. Subplot (d) shows the formation energy of those defects as a function of the oxygen chemical potential with the light color representing oxygen-rich and the dark color oxygen-poor conditions. The O-symbols represent ABINIT results, X-symbols those of FHI-AIMS. The dopant concentration range for which ferroelectricity was experimentally observed (ALD and CSD) is highlighted in grey.

for all three defects depicted in figure 5.20. The effect is particularly strong for the Al_{Hf} defect. This is consistent with experimental observations, since Al-doped HfO_2 has a tendency of showing pinched hysteresis, especially in the dopant concentration range of 7 f.u.% to 10 f.u.%[159].

The $\text{Al}_{\text{Hf}}\text{V}_{\text{O}}$ defect favors all three orthorhombic phases, particularly the two ferroelectric ones. However, within the observed process window for ferroelectricity from 1.5 f.u.% to 4.5 f.u.% the decrease in total energy is insufficient. At a dopant concentration >12 f.u.% the f-phase falls below the m-phase. However, at this point, the f-phase is in competition with the strongly favored t-phase. Therefore, the t-phase is likely to dominate at higher dopant concentrations. The other two types of defects are less conducive for ferroelectricity, as the f-phase is less favored than in $\text{Al}_{\text{Hf}}\text{V}_{\text{O}}$. The behavior of the c-phase is inconsistent for the three defects. In Al_{Hf} -doped HfO_2 , the c-phase increases in total energy and is therefore disadvantaged, while in Al_{Hf} -doped HfO_2 the total energy decreases to the point, where it becomes energetically indistinguishable from the t-phase. In $(2\text{Al}_{\text{Hf}})\text{V}_{\text{O}}$ -doped HfO_2 , the c-phase did not converge, neither did the f'-phase.

The comparison of the formation energy of III-valent dopants is not as simple as it is for II-valent dopants due to the additional dopant atom of the $(2\text{Al}_{\text{Hf}})\text{V}_{\text{O}}$ defect. The formation energies in (d) are therefore referenced to the number of dopant atoms in the 3.125 f.u.% structure for the Al_{Hf} and $\text{Al}_{\text{Hf}}\text{V}_{\text{O}}$ defects and to the 6.25 f.u.% structure for the $(2\text{Al}_{\text{Hf}})\text{V}_{\text{O}}$ defects. The formation energies of the $(2\text{Al}_{\text{Hf}})\text{V}_{\text{O}}$ defects have therefore been divided by a factor of 2 in order to obtain comparable values. The Al_{Hf} defect has the lowest formation

energy at oxygen-rich conditions, followed by the $(2\text{Al}_{\text{Hf}})\text{V}_{\text{O}}$ defect. At oxygen-poor conditions, the Al_{Hf} has the highest formation energy, whereas $\text{Al}_{\text{Hf}}\text{V}_{\text{O}}$ and $(2\text{Al}_{\text{Hf}})\text{V}_{\text{O}}$ defects are approximately equal. For Al, additional defect types were considered, due to the small size of the dopant atom compared to the Hf-atom. These include Al on an oxygen site (Al_{O}), Al on an interstitial site (Al_{I}), two interstitial Al with a Hf-vacancy ($(2\text{Al}_{\text{I}})\text{V}_{\text{Hf}}$), and two interstitial Al with an O- and a Hf-vacancy ($(2\text{Al}_{\text{I}})\text{V}_{\text{Hf}}\text{V}_{\text{O}}$). The results can be found in figure 5.21.

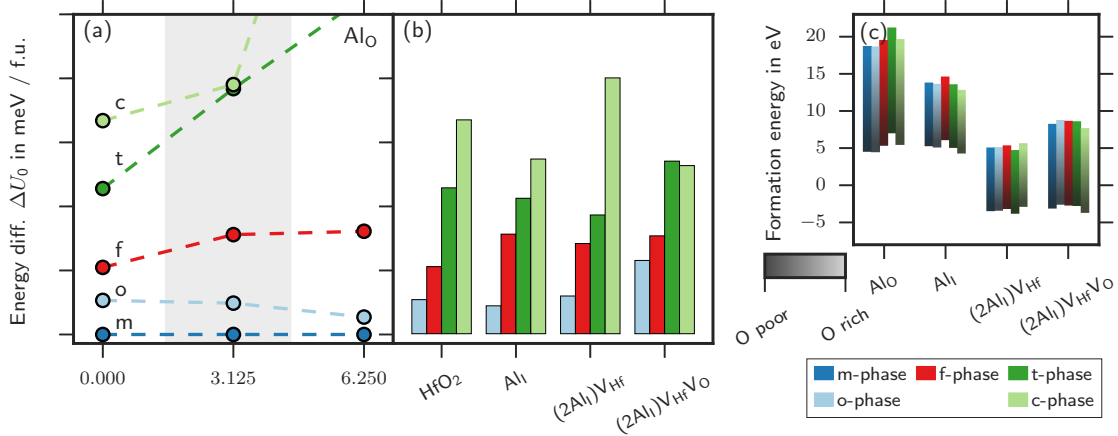


FIG. 5.21: (a) Effect of Al_{O} -doping on the total energy difference ΔU_0 of the various HfO_2 polymorphs compared to the m-phase. (b) Total energies for one- and two-atomic defects interstitial defects in 96-atomic supercells. Therefore, the doping concentration differs for the different defects. (c) shows the formation energy of those defects as a function of the oxygen chemical potential with the light color representing oxygen-rich and the dark color oxygen-poor conditions. The dopant concentration range for which ferroelectricity was experimentally observed (ALD and CSD) is highlighted in grey.

Figure 5.21 (a) depicts the effect of the Al_{O} defect on the total energy of HfO_2 as a function of dopant concentration. The f-, t-, and c-phase are all energetically disadvantaged by the presence of this defect, while the o-phase is slightly stabilized. However, the formation energy of this defect depicted in (c) is by far the highest of all Al defects. Therefore, it is very unlikely that Al_{O} defects can form in HfO_2 . A high formation energy of 18 eV was also found in a study by Hou et al.[171]. Figure 5.21 (b) depict the total energies of undoped, Al_{I} -doped, $(2\text{Al}_{\text{I}})\text{V}_{\text{Hf}}$ -doped, and $(2\text{Al}_{\text{I}})\text{V}_{\text{Hf}}\text{V}_{\text{O}}$ -doped HfO_2 . Each of these defects was calculated with a 96-atomic supercell with one defect. Since the defects have a different amount of dopant atoms, the doping concentration is different for the defects as well (Al_{I} : 3.03 f.u.%, $(2\text{Al}_{\text{I}})\text{V}_{\text{Hf}}$, and $(2\text{Al}_{\text{I}})\text{V}_{\text{Hf}}\text{V}_{\text{O}}$: 6.06 f.u.%). Only one dopant concentration was calculated for each defect. The f-phase is disadvantaged by a rise in total energy by all three types of defects, therefore neither Al_{O} nor interstitial Al defects can account for the observed ferroelectric behavior of Al-doped HfO_2 . The o-phase remains largely unaffected by Al_{I} - and $(2\text{Al}_{\text{I}})\text{V}_{\text{Hf}}$ defects, but gains in total energy from $(2\text{Al}_{\text{I}})\text{V}_{\text{Hf}}\text{V}_{\text{O}}$ defects. The t-phase gains a small energetic

advantage from the Al_{I} - and $(2\text{Al}_{\text{I}})\text{V}_{\text{Hf}}$ defects, but is likewise destabilized by $(2\text{Al}_{\text{I}})\text{V}_{\text{Hf}}\text{V}_{\text{O}}$. The c-phase increases in total energy due to $(2\text{Al}_{\text{I}})\text{V}_{\text{Hf}}$ -doping, but decreases in total energy from the other two types of defects. The f'-phase was excluded from this examination due to convergence issues. The formation energies for $(2\text{Al}_{\text{I}})\text{V}_{\text{Hf}}$ and $(2\text{Al}_{\text{I}})\text{V}_{\text{Hf}}\text{V}_{\text{O}}$ depicted in (c) are divided by a factor of two in order to account for the higher dopant concentration. Of the three types, $(2\text{Al}_{\text{I}})\text{V}_{\text{Hf}}$ is the most favorable defect at oxygen-rich conditions and equal or lower in formation energy to the $(2\text{Al}_{\text{I}})\text{V}_{\text{Hf}}\text{V}_{\text{O}}$ defect at oxygen-poor conditions depending on phase. Comparing the formation energies of the interstitial defect with those of the substitutive defects, one notices that Al_{Hf} - and $(2\text{Al}_{\text{Hf}})\text{V}_{\text{O}}$ defects are always favored over interstitial defects, regardless of oxygen chemical potential. The $\text{Al}_{\text{Hf}}\text{V}_{\text{O}}$ is also favored over all interstitial defects at oxygen-poor conditions but is comparable to the energetically most favorable interstitial defect at oxygen-rich conditions. Therefore it is unlikely that interstitial defects of Al can form in doped HfO_2 . On the other hand, the strong stabilization of the t-phase by substitutional defects would explain the observed field induced ferroelectricity in Al-doped HfO_2 . However, the observed ferroelectricity at lower dopant concentration cannot be explained by either kind of defects in a satisfying manner.

5.7.8 Y-Doping

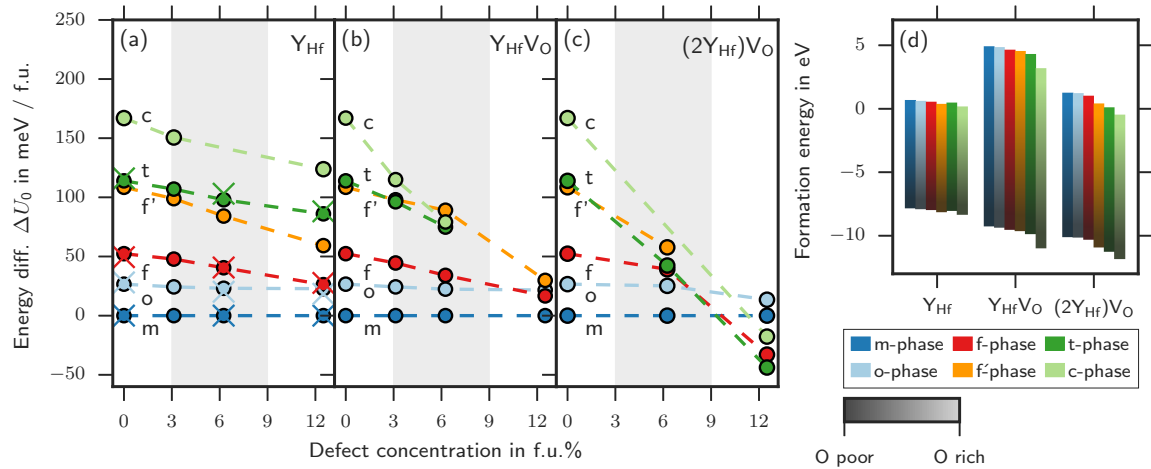


FIG. 5.22: Effect of Y-doping on the total energy difference ΔU_0 of the various HfO_2 polymorphs compared to the m-phase. The defects are (a) Y_{Hf} , (b) $\text{Y}_{\text{Hf}}\text{V}_{\text{O}}$, and (c) $(2\text{Y}_{\text{Hf}})\text{V}_{\text{O}}$. Subplot (d) shows the formation energy of those defects as a function of the oxygen chemical potential with the light color representing oxygen-rich and the dark color oxygen-poor conditions. The O-symbols represent ABINIT results, X-symbols those of FHI-AIMS. The dopant concentration range for which ferroelectricity was experimentally observed (ALD and CSD) is highlighted in grey.

Figure 5.22 depicts the influence of Y_{Hf} , $\text{Y}_{\text{Hf}}\text{V}_{\text{O}}$, and $(2\text{Y}_{\text{Hf}})\text{V}_{\text{O}}$ defects on the total energy difference ΔU_0 of HfO_2 . It is noteworthy, that the results in subplot (a) obtained with ABINIT (O-symbol) line up perfectly with those obtained with FHI-AIMS (X-symbols),

therefore validating the results. The total energy of the o-phase is not affected in respect to the total energy of the m-phase by the presence of either of the three defects. In contrast, both the t- and c-phase show a significant drop in total energy. The effect is particularly pronounced for the $(2Y_{\text{Hf}})V_{\text{O}}$ defect. This is expected behavior, as $(2Y_{\text{Hf}})V_{\text{O}}$ defects are commonly used in the production of partially and fully stabilized Hafnia ceramics. The strong stabilization of the t- and c-phase by the $(2Y_{\text{Hf}})V_{\text{O}}$ defect may explain the experimental results by Kita et al.[65], who found the c-phase at 4 at% dopant concentration in rf-co-sputtered (radiofrequency-co-sputtered) films of HfO_2 and Y_2O_3 . Both ferroelectric phases descend in total energy compared with the monoclinic phases. This is true for all three defects. However, only the Y_{Hf} causes the ferroelectric phases to descend faster in total energy than the t- and c-phase. The ferroelectric phases are therefore likely suppressed by the $(2Y_{\text{Hf}})V_{\text{O}}$ defect, which means only the Y_{Hf} and $Y_{\text{Hf}}V_{\text{O}}$ defects can be used to explain the experimentally observed promotion of ferroelectricity in Y-doped HfO_2 . However, neither defect can favor the f-phase below the m-phase in terms of total energy. This means that the remaining energy difference must be overcome by surface/interface energies in combination with entropy. Unfortunately, the calculations of 12.5 f.u.% $Y_{\text{Hf}}V_{\text{O}}$ -doped t- and c-phase did not converge properly. This is likely caused by trying to fit the large dopant atom into the particularly small cell volumes of the t- and c-phase. Nonetheless, extrapolating these lines in subplot (b) would cause them to intersect the f-phase between 9 f.u.% to 12 f.u.%. This happens to coincide with the upper edge of the observed ferroelectric process window (highlighted in grey, see section 2.3.2 and 2.3.5). In a study by Müller et al.[64] it was found that in 10 nm thin Y-doped HfO_2 films produced by ALD, the f-phase is replaced by the c-phase at a doping concentration in range from 8 mol% to 10 mol%⁶, which is consistent with the results shown here in figure 5.22 (b). CSD experiments by Starschich et al.[66] place the upper edge of the ferroelectric process window between 7.5 mol to 11 mol. From the subplots (b) and (c) it seems that the occurrence of the c-phase requires the presence of associated oxygen vacancies, since the Y_{Hf} defect depicted in (a) does not promote the c-phase as vigorously. This means, that it is probably possible to extend the ferroelectric process window beyond 9 f.u.% by decreasing the amount of oxygen vacancies. The formation energies depicted in figure 5.22 (d) show that the Y_{Hf} defect can form under sufficiently oxygen-rich conditions, while the $Y_{\text{Hf}}V_{\text{O}}$ and $(2Y_{\text{Hf}})V_{\text{O}}$ defects are preferred at lower oxygen supplies. The formation energies in (d) are referenced to the number of dopant atoms in the 3.125 f.u.% structure for the Y_{Hf} and $Y_{\text{Hf}}V_{\text{O}}$ defects and to the 6.25 f.u.% structure for the $(2Y_{\text{Hf}})V_{\text{O}}$ defects. The formation energies of the $(2Y_{\text{Hf}})V_{\text{O}}$ defects have therefore been divided by a factor of 2. Since the c-phase of the 6.25 f.u.% $(2Y_{\text{Hf}})V_{\text{O}}$ structure did not converge, the

⁶Both Müller et al.[64] and Starschich et al.[66] used mol% in reference to $\text{YO}_{1.5}$. The unit mol% is therefore directly comparable to the at% of Kita et al.[65] and f.u.% used throughout this work

formation energy was interpolated from 0 f.u.% and 12.5 f.u.% dopant concentration.

To conclude, Y-doping, in particular the Y_{Hf} and $Y_{\text{Hf}}V_{\text{O}}$ defects, can promote ferroelectricity in HfO_2 , but is insufficient to do so without the help of surface / interface energies. The $Y_{\text{Hf}}V_{\text{O}}$ seems to restrict the ferroelectric process window to below 9 f.u.% due to a phase change into the c-phase, which is consistent with experiments. The Y_{Hf} does not restrict the ferroelectric process window. This could allow for further improvement of the ferroelectric properties and an extension of the ferroelectric process window by reducing the amount of oxygen vacancies within the thin film. The $(2Y_{\text{Hf}})V_{\text{O}}$ causes the t- and c-phase to dominate over the f-phase, which is again consistent with experiments.

5.7.9 La-Doping

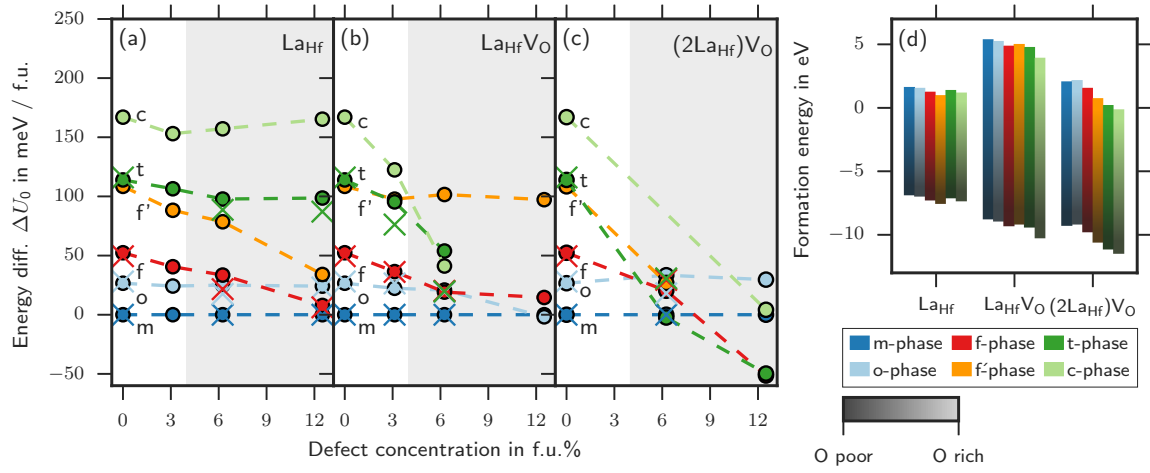


FIG. 5.23: Effect of La-doping on the total energy difference ΔU_0 of the various HfO_2 polymorphs compared to the m-phase. The defects are (a) La_{Hf} , (b) $\text{La}_{\text{Hf}}V_{\text{O}}$, and (c) $(2\text{La}_{\text{Hf}})V_{\text{O}}$. Subplot (d) shows the formation energy of those defects as a function of the oxygen chemical potential with the light color representing oxygen-rich and the dark color oxygen-poor conditions. The O-symbols represent ABINIT results, X-symbols those of FHI-AIMS. The dopant concentration range for which ferroelectricity was experimentally observed (ALD and CSD) is highlighted in grey.

Figure 5.23 depicts the influence of (a) La_{Hf} , (b) $\text{La}_{\text{Hf}}V_{\text{O}}$, and (c) $(2\text{La}_{\text{Hf}})V_{\text{O}}$ defects on the total energy difference ΔU_0 of HfO_2 . It is noteworthy, that the results in subplot (a) obtained with ABINIT (O-symbol) line up perfectly with those obtained with FHI-AIMS (X-symbols), therefore validating the results. The o-phase shows little effect from the La_{Hf} and $(2\text{La}_{\text{Hf}})V_{\text{O}}$ defects. However, at a dopant concentration of 12.5 f.u.% $\text{La}_{\text{Hf}}V_{\text{O}}$ defects, the o-phase drops below the total energy of m-phase. The behavior of both tetragonal and cubic La-doped HfO_2 is very similar to that of Y-doped HfO_2 . While the La_{Hf} defect has little to no effect on the total energy of either of the two phases, the $\text{La}_{\text{Hf}}V_{\text{O}}$ and $(2\text{La}_{\text{Hf}})V_{\text{O}}$ defects lead to a strong stabilization of the t- and c-phase. The effect is stronger in La-doped than in Y-doped HfO_2 . The t-phase becomes bulk stable around a dopant concentration of 6 f.u.% when doped with

the $(2\text{La}_{\text{Hf}})\text{V}_{\text{O}}$ defect. Like in Y-doping, the occurrence of t- and c-phase seems to depend on the existence of oxygen vacancies in La-doped HfO_2 . The f-phase is favored by all three defects but is in strong competition with the t- and c-phase for the $\text{La}_{\text{Hf}}\text{V}_{\text{O}}$ and $(2\text{La}_{\text{Hf}})\text{V}_{\text{O}}$ defects. This rules out ferroelectricity as a consequence of the $(2\text{La}_{\text{Hf}})\text{V}_{\text{O}}$ defect and the ferroelectric process window is truncated in $\text{La}_{\text{Hf}}\text{V}_{\text{O}}$ doped HfO_2 in the range of 6 f.u.% to 9 f.u.%. The La_{Hf} defect does not restrict the ferroelectric process window. This difference might be the cause of the contradicting reports for the location of the upper edge of the ferroelectric process window. Chernikova et al.[71] reported ferroelectricity for 2.1 at % and 3.7 at % La-dopant concentration, but a complete loss of ferroelectricity and the formation of a cubic phase at a dopant concentration of 5.8 at % in ALD deposited thin films of 10 nm thickness. This is in concordance with the DFT results of the $\text{La}_{\text{Hf}}\text{V}_{\text{O}}$ defect. However, a recent publication of Schröder et al.[72] successfully achieved to extend the ferroelectric process window to 20 at %. This is only explainable with the La_{Hf} defect, but not with the $\text{La}_{\text{Hf}}\text{V}_{\text{O}}$ and $(2\text{La}_{\text{Hf}})\text{V}_{\text{O}}$ defects. Like in Y-doped HfO_2 , ferroelectricity seems to benefit from oxygen-rich production conditions, since the formation energies favor the La_{Hf} defect under these conditions (see figure 5.23 (d)). The stabilizing effect of defects on the f-phase is stronger for La-doped HfO_2 than for Y-doped HfO_2 . Nonetheless, the effect from dopants is insufficient to overcome the m-phase. Additional help from surface interface energies is needed to explain the observed ferroelectric behavior. The f'-phase behaves similarly to the f-phase for the La_{Hf} and $(2\text{La}_{\text{Hf}})\text{V}_{\text{O}}$ defects but does not react to $\text{La}_{\text{Hf}}\text{V}_{\text{O}}$ defects. The formation energies in (d) are referenced to the number of dopant atoms in the 3.125 f.u.% structure for the La_{Hf} and $\text{La}_{\text{Hf}}\text{V}_{\text{O}}$ defects and to the 6.25 f.u.% structure for the $(2\text{La}_{\text{Hf}})\text{V}_{\text{O}}$ defects. The formation energies of the $(2\text{La}_{\text{Hf}})\text{V}_{\text{O}}$ defects have therefore been divided by a factor of 2. Since the c-phase of the 6.25 f.u.% $(2\text{La}_{\text{Hf}})\text{V}_{\text{O}}$ structure did not converge, the formation energy was interpolated from 0 f.u.% and 12.5 f.u.% dopant concentration.

To conclude, La-doping is the most promising candidate under the III-valent dopants investigated within this work for stabilizing the f-phase. In particular, the La_{Hf} defect seems promising, as it allows for a wide ferroelectric process window which has been experimentally observed. The $\text{La}_{\text{Hf}}\text{V}_{\text{O}}$ and $(2\text{La}_{\text{Hf}})\text{V}_{\text{O}}$ defects are inconsistent with such a wide ferroelectric process window, as the t- and c-phase start to dominate at higher dopant concentrations according to the DFT results. Beneficial for the generation of the La_{Hf} defects are the low formation energies under oxygen-rich production conditions.

6 Summary and Conclusion

In this thesis, effects leading to the stabilization of ferroelectric HZO were studied with DFT methods. To that end, six phases, two of them ferroelectric, were investigated. At first, the influence of mixing HfO_2 and ZrO_2 was explored, as $\text{Hf}_{0.5}\text{Zr}_{0.5}\text{O}_2$ was experimentally found to be ferroelectric, while pure HfO_2 and ZrO_2 were not[26]. The total energies of the phases changed mostly linear with Zr-content. Therefore, the monoclinic, non-ferroelectric ground state remained the energetic minimum for all stoichiometries.

Next, the influence of temperature on phase stability was investigated with DFPT. It was found, that the ferroelectric f-phase is reduced slightly in free energy compared to the m-phase with increasing temperature. However, this cannot explain the observed ferroelectricity, as a tetragonal high-temperature phase which starts above the f-phase will become energetically favorable to both the m-phase and f-phase with increasing temperature.

Stress was likewise found to be an inadequate explanation of ferroelectricity in HZO. While it is possible to destabilize the m-phase in favor of other phases, including the f-phase with some stress conditions, the stress values required to do so are in the range of 10 GPa or even higher. Such large values should surely have been noted within the experimental literature. However, this reasoning assumes a monoclinic initial state which might not correspond to experimental conditions. Plotting the results of the stress calculations over strain or lattice parameters reveals, that some strain conditions are capable to stabilize the f-phase at very low strain values. The corresponding stress values are therefore equally low. The difference between the stress and strain results are different interpretations of the available data. The first interpretation assumes a monoclinic initial state and asks the question of how much stress needs to be applied to that initial state before the monoclinic phase is no longer stable. The second interpretation assumes, that HZO is in some manner constrained and asks two questions: How much stress needs to be applied to a hypothetical phase for it to fit in this constraint? And which phase is the energetically most favorable under these stress conditions? Given appropriate initial conditions, stress values in the range of 1 GPa might be sufficient to explain the occurrence of ferroelectricity in HZO. Such constraints may arise from a lattice mismatch between HZO and the substrate or from the production process due to Ostwald's step rule[165] leading to the c-phase or t-phase crystallizing first. These two phases have particular small unit cell sizes, therefore freezing the film into a state of limited spatial availability. This prevents the film from assuming the monoclinic ground state as this phase is particularly large. The film can then relax into a state of similar size, like the f-phase. Re-melting or diffusion processes might allow the film to overcome these constraints[167].

An alternative explanation for the occurrence of ferroelectricity in HZO was developed in the form of a thermodynamic model taking into account the coherent interface energy between different phases in different regions within a single grain. Experimental results suggest, that HZO grains have a tetragonal interlayer surrounding the bulk of the grain[139, 140]. The interface energy between the two different phases within the core and interlayer of the grain can stabilize phases with an higher total energy, but with a more favorable surface energy than the m-phase. A model based on DFT data was developed which contains the specific interface energies at room temperature as fit parameters. This model was then fitted to experimental data from Park et al.[143] Using the film thickness and stoichiometry as input parameters, the model is able to predict the ferroelectricity of a film at room temperature, assuming the same production process. Therefore, interface energy is a viable explanation for the ferroelectricity of HZO. This explanation does not exclude or contradict the explanation invoking strain, as both effects may occur simultaneously.

Several II- and III-valent dopants were tested for their potential to stabilize the f-phase in HfO₂. II-valent dopants were Be, Mg, Ca, Sr, and Ba, III-valent dopants were Al, Y, and La. Electronically compensated, ionically compensated, and mixed compensated defects were considered. La and Y proved the most effective in stabilizing the f-phase. Among the II-valent dopants, Sr was the most promising. Al doping was found to stabilize the t-phase, which explains the observed field induced ferroelectricity of Al-doped HfO₂. All dopants have common, that vacancies associated with the dopant atoms favor the t-phase over the f-phase. The formation energies of these unwanted defects become unfavorable in comparison to the vacancy free defects at sufficiently oxygen-rich process conditions.

In conclusion, three effects contributing to the ferroelectricity of HZO were identified in this work: strains, interface energies, and dopants. All three stabilization mechanisms are dependent on the production and crystallization process of the ferroelectric film. Favorable strain conditions can occur, when the film crystallizes in phases with small unit cells, like the c-or t-phase, constraining the films. Therefore, conditions allowing the film to overcome these constraints, like prolonged exposure to high temperatures should be avoided. The coherent interface energy effect is dependent on a large surface to volume ratio of the grains. Conditions, favorable to the formation of large grains are therefore counterproductive.

The formation of large grains is usually supported by long exposure time to high temperatures. A high supply of oxygen during film deposition can help to avoid the formation of unwanted oxygen vacancies, which could otherwise negatively affect the ferroelectric properties. Conditions favorable to the formation of ferroelectricity are therefore:

- 1. Doping with appropriate dopants (La, Y, Sr).**
- 2. High supply of oxygen during film deposition.**
- 3. Optimization of the thermal budget during the thermal annealing/crystallization process (High enough to ensure sufficient crystallization but low enough to minimize excessive grain growth and diffusion).**

While the results presented in this work will hopefully help to advance our understanding of the ferroelectric $\text{Hf}_{1-x}\text{Zr}_x\text{O}_2$ system, further research is necessary. Particular attention should be paid to kinetic models of the crystallization and phase transition process, since these processes seem to play a vital role during the manufacture of ferroelectric thin films.

Bibliography

- [1] G. E. Moore. Cramming more components onto integrated circuits. *Electronics*, pages 114–117, 1965. Reprint.
- [2] M. T. Bohr, R. S. Chau, T. Ghani, and K. Mistry. The High-k Solution. *IEEE Spectrum*, 44(10):29–35, Oct 2007.
- [3] ITRS. International Technology Roadmap for Semiconductors 2.0 2015 Edition Executive Report. Technical report, ITRS, 2017. <http://www.itrs2.net/itrs-reports.html>.
- [4] Samsung. Samsung Now Mass Producing Industry’s First 2nd-generation, 10-Nanometer Class DRAM, 2017. <https://news.samsung.com/global/samsung-now-mass-producing-industrys-first-2nd-generation-10-nanometer-class-dram> (Access date: 2018-05-01).
- [5] Samsung. Samsung Begins Mass Production of 10nm-class 16Gb LPDDR4X DRAM for Automobiles, 2018. <https://news.samsung.com/global/samsung-begins-mass-production-of-10nm-class-16gb-lpddr4x-dram-for-automobiles> (Access date: 2018-05-01).
- [6] W. K. Cheng, R. Y. Wang, and X. L. Li. 3D architecture exploration on thermal effect of DRAM refresh. In *2016 11th International Microsystems, Packaging, Assembly and Circuits Technology Conference (IMPACT)*, pages 285–288, Oct 2016.
- [7] Rambus. Part 1: DRAM goes cryogenic, 2017. <https://www.rambus.com/blogs/part-1-dram-goes-cryogenic/> (Access date: 2018-05-01).
- [8] G. I. Meijer. Cooling Energy-Hungry Data Centers. *Science*, 328(5976):318–319, 2010.
- [9] Z. Li and S. G. Kandlikar. Current Status and Future Trends in Data-Center Cooling Technologies. *Heat Transfer Engineering*, 36(6):523–538, 2015.
- [10] I. G. Baek, M. S. Lee, S. Seo, M. J. Lee, D. H. Seo, D. S. Suh, J. C. Park, S. O. Park, H. S. Kim, I. K. Yoo, U. I. Chung, and J. T. Moon. Highly scalable nonvolatile resistive memory using simple binary oxide driven by asymmetric unipolar voltage pulses. In *IEDM Technical Digest. IEEE International Electron Devices Meeting, 2004.*, pages 587–590, Dec 2004.

- [11] H. Y. Lee, P. S. Chen, T. Y. Wu, Y. S. Chen, C. C. Wang, P. J. Tzeng, C. H. Lin, F. Chen, C. H. Lien, and M. J. Tsai. Low power and high speed bipolar switching with a thin reactive Ti buffer layer in robust HfO₂ based RRAM. In *2008 IEEE International Electron Devices Meeting*, pages 1–4, Dec 2008.
- [12] A. Pohm, C. Sie, R. Uttecht, V. Kao, and O. Agrawal. Chalcogenide glass bistable resistivity (Ovonic) memories. *IEEE Transactions on Magnetics*, 6(3):592–592, Sep 1970.
- [13] H. S. P. Wong, S. Raoux, S. Kim, J. Liang, J. P. Reifenberg, B. Rajendran, M. Asheghi, and K. E. Goodson. Phase Change Memory. *Proceedings of the IEEE*, 98(12):2201–2227, Dec 2010.
- [14] A. Chanthbouala, A. Crassous, V. Garcia, K. Bouzehouane, S. Fusil, X. Moya, J. Allibe, B. Dlubak, J. Grollier, S. Xavier, C. Deranlot, A. Moshar, R. Proksch, N. D. Mathur, M. Bibes, and A. Barthélémy. Solid-state memories based on ferroelectric tunnel junctions. *Nature Nanotechnology*, 7:101, dec 2011.
- [15] T. Mikolajick, C. Dehm, W. Hartner, I. Kasko, M. Kastner, N. Nagel, M. Moert, and C. Mazure. FeRAM technology for high density applications. *Microelectronics Reliability*, 41(7):947 – 950, 2001.
- [16] H. Ishiwara. Ferroelectric Random Access Memories. *Journal of Nanoscience and Nanotechnology*, 12(10):7619–7627, 2012.
- [17] S. R. Summerfelt, T. S. Moise, K. R. Udayakumar, K. Boku, K. Remack, J. Rodriguez, J. Gertas, H. McAdams, S. Madan, J. Eliason, J. Groat, D. Kim, P. Staubs, M. Depner, and R. Bailey. High-Density 8Mb 1T-1C Ferroelectric Random Access Memory Embedded Within a Low-Power 130nm Logic Process. In *2007 Sixteenth IEEE International Symposium on the Applications of Ferroelectrics*, pages 9–10, May 2007.
- [18] S. Slesazeck, U. Schroeder, and T. Mikolajick. Embedding hafnium oxide based FeFETs in the memory landscape. In *2018 International Conference on IC Design Technology (ICICDT)*, pages 121–124, June 2018.
- [19] E. M. Philofsky. FRAM-the ultimate memory. In *Proceedings of Nonvolatile Memory Technology Conference*, pages 99–104, June 1996.
- [20] Fujitsu Semiconductor Limited. FUJITSU Semiconductor FRAM, 2017. <http://www.fujitsu.com/global/documents/products/devices/semiconductor/fram/overview/brochure/AD05-00033-10E.pdf> (Access date: 2018-05-01).

- [21] Texas Instruments. FRAM – New Generation of Non-Volatile Memory, 2009. <http://www.ti.com/lit/ml/szzt014a/szzt014a.pdf> (Access date: 2018-05-01).
- [22] R. E. Jones Jr., P. D. Maniar, A. C. Campbell, R. Moazzami, J. L. Dupuie, R. B. Gregory, M. L. Kottke, M. L. Bozack, J. R. Williams, and J. M. Ferrero. Materials interactions in the integration of PZT ferroelectric capacitors. *Integrated Ferroelectrics*, 6(1-4):81–92, 1995.
- [23] J. Rodriguez, K. Remack, J. Gertas, L. Wang, C. Zhou, K. Boku, J. Rodriguez-Latorre, K. R. Udayakumar, S. Summerfelt, T. Moise, D. Kim, J. Groat, J. Eliason, M. Depner, and F. Chu. Reliability of Ferroelectric Random Access memory embedded within 130nm CMOS. In *2010 IEEE International Reliability Physics Symposium*, pages 750–758, May 2010.
- [24] T. S. Böscke, J. Müller, D. Bräuhaus, U. Schröder, and U. Böttger. Ferroelectricity in hafnium oxide thin films. *Applied Physics Letters*, 99(10):102903, 2011.
- [25] S. Starschich, T. Schenk, U. Schroeder, and U. Boettger. Ferroelectric and piezoelectric properties of $\text{Hf}_{1-x}\text{Zr}_x\text{O}_2$ and pure ZrO_2 films. *Applied Physics Letters*, 110(18):182905, 2017.
- [26] J. Müller, T. S. Böscke, U. Schröder, S. Mueller, D. Bräuhaus, U. Böttger, L. Frey, and T. Mikolajick. Ferroelectricity in Simple Binary ZrO_2 and HfO_2 . *Nano Letters*, 12(8):4318–4323, 2012. PMID: 22812909.
- [27] T. Mikolajick, S. Slesazeck, M. H. Park, and U. Schroeder. Ferroelectric hafnium oxide for ferroelectric random-access memories and ferroelectric field-effect transistors. *MRS Bulletin*, 43(5):340–346, 2018.
- [28] M. Trentzsch, S. Flachowsky, R. Richter, J. Paul, B. Reimer, D. Utess, S. Jansen, H. Mulaosmanovic, S. Müller, S. Slesazeck, J. Ocker, M. Noack, J. Müller, P. Polakowski, J. Schreiter, S. Beyer, T. Mikolajick, and B. Rice. A 28nm HKMG super low power embedded NVM technology based on ferroelectric FETs. In *2016 IEEE International Electron Devices Meeting (IEDM)*, pages 11.5.1–11.5.4, Dec 2016.
- [29] J. Wilks. *The Third Law of Thermodynamics*. Oxford Library of the Physical Sciences. Oxford University Press, 1963.
- [30] J. Vidal. *Thermodynamics*, chapter Thermodynamic Function: Internal Energy, Enthalpy, Entropy, Helmholtz Energy, and Gibbs Energy, page 19. Editions Technip, Paris, France, 2003.

- [31] U. Böttger. *Dielectric Properties of Polar Oxides*, chapter 1, pages 11–38. Wiley-Blackwell, 2005.
- [32] V. M. Fridkin and S. Ducharme. *Ferroelectricity at the nanoscale*, volume 1 of *NanoScience and Technology*. Springer, 2014.
- [33] H. Lueken. *Magnetochemie: Eine Einführung in Theorie und Anwendung*. Teubner Studienbücher Chemie. Vieweg+Teubner Verlag, 2013.
- [34] R. Ruh, H. J. Garrett, R. F. Domagala, and N. M. Tallan. The System Zirconia-Hafnia. *Journal of the American Ceramic Society*, 51(1):23–28, 1968.
- [35] J. Wang, H. P. Li, and R. Stevens. Hafnia and hafnia-toughened ceramics. *Journal of Materials Science*, 27(20):5397–5430, 1992.
- [36] J. Meija, T. B. Coplen, M. Berglund, W. A. Brand, P. De Bièvre, M. Gröning, N. E. Holden, J. Irrgeher, R. D. Loss, T. Walczyk, and T. Prohaska. Atomic weights of the elements 2013 (IUPAC Technical Report). *Pure and Applied Chemistry*, 88:265–291, 2016.
- [37] J. C. Slater. Atomic Radii in Crystals. *The Journal of Chemical Physics*, 41(10):3199–3204, 1964.
- [38] R. D. Shannon. Revised effective ionic radii and systematic studies of interatomic distances in halides and chalcogenides. *Acta Crystallographica Section A*, 32(5):751–767, Sep 1976.
- [39] V. Goldschmidt and T. Barth. *Geochemische Verteilungsgesetze der Elemente: Isomorphie und Polymorphie des Sesquioxide : die Lanthaniden-Kontraktion und ihre Konsequenzen*. Number Bd. 5 in Skrifter. Ja. Dybwad, 1925.
- [40] J. Adam and M. D. Rogers. The crystal structure of ZrO_2 and HfO_2 . *Acta Crystallographica*, 12(11):951, Nov 1959.
- [41] D. Panda and T.-Y. Tseng. Growth, dielectric properties, and memory device applications of ZrO_2 thin films. *Thin Solid Films*, 531:1 – 20, 2013.
- [42] C. Wang, M. Zinkevich, and F. Aldinger. The Zirconia–Hafnia System: DTA Measurements and Thermodynamic Calculations. *Journal of the American Ceramic Society*, 89(12):3751–3758, 2006.
- [43] R. C. Garvie, R. H. Hannink, and R. T. Pascoe. Ceramic steel? *Nature*, 258:703–704, 1975.

- [44] R. H. J. Hannink, P. M. Kelly, and B. C. Muddle. Transformation Toughening in Zirconia-Containing Ceramics. *Journal of the American Ceramic Society*, 83(3):461–487, 2000.
- [45] E. H. Kisi and C. Howard. Crystal Structures of Zirconia Phases and their Inter-Relation. In *Zirconia Engineering Ceramics*, volume 153 of *Key Engineering Materials*, pages 1–36. Trans Tech Publications, 2 1998.
- [46] K. Parlinski, Z. Q. Li, and Y. Kawazoe. First-Principles Determination of the Soft Mode in Cubic ZrO_2 . *Phys. Rev. Lett.*, 78:4063–4066, May 1997.
- [47] T. D. Huan, V. Sharma, G. A. Rossetti, and R. Ramprasad. Pathways towards ferroelectricity in hafnia. *Phys. Rev. B*, 90:064111, Aug 2014.
- [48] S. E. Reyes-Lillo, K. F. Garrity, and K. M. Rabe. Antiferroelectricity in thin-film ZrO_2 from first principles. *Phys. Rev. B*, 90:140103, Oct 2014.
- [49] Q. Zeng, A. R. Oganov, A. O. Lyakhov, C. Xie, X. Zhang, J. Zhang, Q. Zhu, B. Wei, I. Grigorenko, L. Zhang, and L. Cheng. Evolutionary search for new high-k dielectric materials: methodology and applications to hafnia-based oxides. *Acta Crystallographica Section C*, 70(2):76–84, Feb 2014.
- [50] R. Materlik, C. Künneth, and A. Kersch. The origin of ferroelectricity in $\text{Hf}_{1-x}\text{Zr}_x\text{O}_2$: A computational investigation and a surface energy model. *Journal of Applied Physics*, 117(13):134109, 2015.
- [51] C. Künneth, R. Materlik, and A. Kersch. Modeling ferroelectric film properties and size effects from tetragonal interlayer in $\text{Hf}_{1-x}\text{Zr}_x\text{O}_2$ grains. *Journal of Applied Physics*, 121(20):205304, 2017.
- [52] X. Sang, E. D. Grimley, T. Schenk, U. Schroeder, and J. M. LeBeau. On the structural origins of ferroelectricity in HfO_2 thin films. *Applied Physics Letters*, 106(16):162905, 2015.
- [53] O. Ohtaka, T. Yamanaka, S. Kume, N. Hara, H. Asano, and F. Izumi. Structural Analysis of Orthorhombic ZrO_2 by High Resolution Neutron Powder Diffraction. *Proceedings of the Japan Academy, Series B*, 66(10):193–196, 1990.
- [54] O. Ohtaka, T. Yamanaka, S. Kume, N. Hara, H. Asano, and F. Izumi. Structural Analysis of Orthorhombic Hafnia by Neutron Powder Diffraction. *Journal of the American Ceramic Society*, 78(1):233–237, 1995.
- [55] Y. Al-Khatatbeh, K. K. M. Lee, and B. Kiefer. Phase relations and hardness trends of ZrO_2 phases at high pressure. *Phys. Rev. B*, 81:214102, Jun 2010.

- [56] Y. Al-Khatatbeh, K. K. M. Lee, and B. Kiefer. Phase diagram up to 105 GPa and mechanical strength of HfO₂. *Phys. Rev. B*, 82:144106, Oct 2010.
- [57] C. Richter, T. Schenk, M. H. Park, F. A. Tschardtke, E. D. Grimley, J. M. LeBeau, C. Zhou, C. M. Fancher, J. L. Jones, T. Mikolajick, and U. Schroeder. Si Doped Hafnium Oxide—A “Fragile” Ferroelectric System. *Advanced Electronic Materials*, 3(10):1700131–n/a, 2017. 1700131.
- [58] S. Jachalke, T. Schenk, M. H. Park, U. Schroeder, T. Mikolajick, H. Stöcker, E. Mehner, and D. C. Meyer. Pyroelectricity of silicon-doped hafnium oxide thin films. *Applied Physics Letters*, 112(14):142901, 2018.
- [59] S. Starschich and U. Boettger. An extensive study of the influence of dopants on the ferroelectric properties of HfO₂. *J. Mater. Chem. C*, 5:333–338, 2017.
- [60] T. Schenk, S. Mueller, U. Schroeder, R. Materlik, A. Kersch, M. Popovici, C. Adelman, S. V. Elshocht, and T. Mikolajick. Strontium doped hafnium oxide thin films: Wide process window for ferroelectric memories. In *2013 Proceedings of the European Solid-State Device Research Conference (ESSDERC)*, pages 260–263, Sept 2013.
- [61] S. Mueller, J. Mueller, A. Singh, S. Riedel, J. Sundqvist, U. Schroeder, and T. Mikolajick. Incipient Ferroelectricity in Al-Doped HfO₂ Thin Films. *Advanced Functional Materials*, 22(11):2412–2417, 2012.
- [62] M. H. Park, T. Schenk, C. M. Fancher, E. D. Grimley, C. Zhou, C. Richter, J. M. LeBeau, J. L. Jones, T. Mikolajick, and U. Schroeder. A comprehensive study on the structural evolution of HfO₂ thin films doped with various dopants. *Journal of Materials Chemistry C*, 5:4677, 2017.
- [63] Y. W. Yoo, W. Jeon, W. Lee, C. H. An, S. K. Kim, and C. S. Hwang. Structure and Electrical Properties of Al-Doped HfO₂ and ZrO₂ Films Grown via Atomic Layer Deposition on Mo Electrodes. *Applied Materials and Interfaces*, 6:22474, 2014.
- [64] J. Müller, U. Schröder, T. S. Böske, I. Müller, U. Böttger, L. Wilde, J. Sundqvist, M. Lemberger, P. Kücher, T. Mikolajick, , and L. Frey. Ferroelectricity in yttrium-doped hafnium oxide. *Journal of Applied Physics*, 110(11):114113, 2011.
- [65] K. Kita, K. Kyuno, and A. Toriumi. Permittivity increase of yttrium-doped HfO₂ through structural phase transformation. *Applied Physics Letters*, 86(10):102906, 2005.
- [66] S. Starschich, D. Griesche, T. Schneller, and U. Böttger. Chemical Solution Deposition of Ferroelectric Hafnium Oxide for Future Lead Free Ferroelectric Devices. *ECS Journal of Solid State Science and Technology*, 4(12):P419, 2015.

- [67] T. Shimizu, K. Katayama, T. Kiguchi, A. Akama, T. J. Konno, and H. Funakubo. Growth of epitaxial orthorhombic $\text{YO}_{1.5}$ -substituted HfO_2 thin film. *Applied Physics Letters*, 107(3):032910, 2015.
- [68] T. Shimizu, K. Katayama, T. Kiguchi, A. Akama, T. J. Konno, O. Sakata, and H. Funakubo. The demonstration of significant ferroelectricity in epitaxial Y-doped HfO_2 film. *Scientific Reports*, 6(32931), 2016.
- [69] T. Olsen, U. Schröder, S. Müller, A. Krause, D. Martin, A. Singh, J. Müller, M. Geidel, and T. Mikolajick. Co-sputtering yttrium into hafnium oxide thin films to produce ferroelectric properties. *Applied Physics Letters*, 101(8):082905, 2012.
- [70] J. Müller, T. S. Böske, S. Müller, E. Yurchuk, P. Polakowski, J. Paul, D. Martin, T. Schenk, K. Khullar, A. Kersch, W. Weinreich, S. Riedel, K. Seidel, A. Kumar, T. M. Arruda, S. V. Kalinin, T. Schlösser, R. Boschke, R. van Bentum, U. Schröder, and T. Mikolajick. Ferroelectric hafnium oxide: A CMOS-compatible and highly scalable approach to future ferroelectric memories. In *2013 IEEE International Electron Devices Meeting*, pages 10.8.1–10.8.4, Dec 2013.
- [71] A. G. Chernikova, D. S. Kuzmichev, D. V. Negrov, M. G. Kozodaev, S. N. Polyakov, and A. M. Markeev. Ferroelectric properties of full plasma-enhanced ALD $\text{TiN/La:HfO}_2/\text{TiN}$ stacks. *Applied Physics Letters*, 108(24):242905, 2016.
- [72] U. Schroeder, C. Richter, M. H. Park, T. Schenk, M. Pešić, M. Hoffmann, F. P. G. Fengler, D. Pohl, B. Rellinghaus, C. Zhou, C.-C. Chung, J. L. Jones, and T. Mikolajick. Lanthanum-Doped Hafnium Oxide: A Robust Ferroelectric Material. *Inorganic Chemistry*, 2018. PMID: 29446630.
- [73] L. Xu, S. Shibayama, K. Izukashi, T. Nishimura, T. Yajima, S. Migita, and A. Toriumi. General relationship for cation and anion doping effects on ferroelectric HfO_2 formation. In *2016 IEEE International Electron Devices Meeting (IEDM)*, pages 25.2.1–25.2.4, Dec 2016.
- [74] S. Mueller, C. Adelman, A. Singh, S. Van Elshocht, U. Schroeder, and T. Mikolajick. Ferroelectricity in Gd-Doped HfO_2 Thin Films. *ECS Journal of Solid State Science and Technology*, 1(6):N123–N126, 2012.
- [75] S. Starschich and U. Böttger. Doped ZrO_2 for future lead free piezoelectric devices. *Journal of Applied Physics*, 123(4):044101, 2018.
- [76] M. H. Park, H. J. Kim, Y. J. Kim, W. Lee, T. Moon, and C. S. Hwang. Evolution of phases and ferroelectric properties of thin $\text{Hf}_{0.5}\text{Zr}_{0.5}\text{O}_2$ films according to the thickness and annealing temperature. *Applied Physics Letters*, 102(24):242905, 2013.

- [77] M. Pešić, C. Künneth, M. Hoffmann, H. Mulaosmanovic, S. Müller, E. T. Breyer, U. Schroeder, A. Kersch, T. Mikolajick, and S. Slesazek. A computational study of hafnia-based ferroelectric memories: from ab initio via physical modeling to circuit models of ferroelectric device. *Journal of Computational Electronics*, 16(4):1236–1256, Dec 2017.
- [78] M. H. Park, H. Joon Kim, Y. Jin Kim, T. Moon, and C. Seong Hwang. The effects of crystallographic orientation and strain of thin $\text{Hf}_{0.5}\text{Zr}_{0.5}\text{O}_2$ film on its ferroelectricity. *Applied Physics Letters*, 104(7):072901, 2014.
- [79] H. J. Kim, M. H. Park, Y. J. Kim, Y. H. Lee, W. Jeon, T. Gwon, T. Moon, K. D. Kim, and C. S. Hwang. Grain size engineering for ferroelectric $\text{Hf}_{0.5}\text{Zr}_{0.5}\text{O}_2$ films by an insertion of Al_2O_3 interlayer. *Applied Physics Letters*, 105(19):192903, 2014.
- [80] R. C. Garvie. The Occurrence of Metastable Tetragonal Zirconia as a Crystallite Size Effect. *The Journal of Physical Chemistry*, 69(4):1238–1243, 1965.
- [81] S. Riedel, P. Polakowski, and J. Müller. A thermally robust and thickness independent ferroelectric phase in laminated hafnium zirconium oxide. *AIP Advances*, 6(9):095123, 2016.
- [82] P. Polakowski and J. Müller. Ferroelectricity in undoped hafnium oxide. *Applied Physics Letters*, 106(23):232905, 2015.
- [83] P. Hohenberg and W. Kohn. Inhomogeneous Electron Gas. *Phys. Rev.*, 136:B864–B871, Nov 1964.
- [84] W. Kohn and L. J. Sham. Self-Consistent Equations Including Exchange and Correlation Effects. *Phys. Rev.*, 140:A1133–A1138, Nov 1965.
- [85] E. Schrödinger. An Undulatory Theory of the Mechanics of Atoms and Molecules. *Phys. Rev.*, 28:1049–1070, Dec 1926.
- [86] M. Born and R. Oppenheimer. Zur Quantentheorie der Molekeln. *Annalen der Physik*, 389(20):457–484, 1927.
- [87] R. P. Feynman. Forces in Molecules. *Phys. Rev.*, 56:340–343, Aug 1939.
- [88] L. H. Thomas. The calculation of atomic fields. *Mathematical Proceedings of the Cambridge Philosophical Society*, 23(5):542–548, 1927.
- [89] D. C. Langreth and M. J. Mehl. Beyond the local-density approximation in calculations of ground-state electronic properties. *Phys. Rev. B*, 28:1809–1834, Aug 1983.

- [90] A. D. Becke. Density-functional exchange-energy approximation with correct asymptotic behavior. *Phys. Rev. A*, 38:3098–3100, Sep 1988.
- [91] J. P. Perdew, J. A. Chevary, S. H. Vosko, K. A. Jackson, M. R. Pederson, D. J. Singh, and C. Fiolhais. Atoms, molecules, solids, and surfaces: Applications of the generalized gradient approximation for exchange and correlation. *Phys. Rev. B*, 46:6671–6687, Sep 1992.
- [92] J. P. Perdew, K. Burke, and M. Ernzerhof. Generalized Gradient Approximation Made Simple. *Phys. Rev. Lett.*, 77:3865–3868, Oct 1996.
- [93] A. D. Becke. A new mixing of Hartreefunctional theories. *The Journal of Chemical Physics*, 98(2):1372–1377, 1993.
- [94] J. P. Perdew, M. Ernzerhof, and K. Burke. Rationale for mixing exact exchange with density functional approximations. *The Journal of Chemical Physics*, 105(22):9982–9985, 1996.
- [95] D. M. Ceperley and B. J. Alder. Ground State of the Electron Gas by a Stochastic Method. *Phys. Rev. Lett.*, 45:566–569, Aug 1980.
- [96] J. P. Perdew and A. Zunger. Self-interaction correction to density-functional approximations for many-electron systems. *Phys. Rev. B*, 23:5048–5079, May 1981.
- [97] J. P. Perdew and Y. Wang. Accurate and simple analytic representation of the electron-gas correlation energy. *Phys. Rev. B*, 45:13244–13249, Jun 1992.
- [98] W. Ritz. Über eine neue Methode zur Lösung gewisser Variationsprobleme der mathematischen Physik. *Journal für die reine und angewandte Mathematik*, 135:1–61, 1909.
- [99] N. J. v. N. L. Hilbert, D. Über die Grundlagen der Quantenmechanik. *Mathematische Annalen*, 98:1–30, 1928.
- [100] J. v. Neumann. Allgemeine Eigenwerttheorie Hermitescher Funktionaloperatoren. *Mathematische Annalen*, 102:49–131, 1930.
- [101] V. Blum, R. Gehrke, F. Hanke, P. Havu, V. Havu, X. Ren, K. Reuter, and M. Scheffler. Ab initio molecular simulations with numeric atom-centered orbitals. *Computer Physics Communications*, 180(11):2175 – 2196, 2009.
- [102] F. Bloch. Über die Quantenmechanik der Elektronen in Kristallgittern. *Zeitschrift für Physik*, 52(7):555–600, Jul 1929.

- [103] M. R. Hestenes and E. Stiefel. Methods of Conjugate Gradients for Solving Linear Systems. *Journal of Research of the National Bureau of Standards*, 49(6):409–436, December 1952.
- [104] A. V. Knyazev. Toward the Optimal Preconditioned Eigensolver: Locally Optimal Block Preconditioned Conjugate Gradient Method. *SIAM Journal on Scientific Computing*, 23(2):517–541, 2001.
- [105] H. Hellmann. A New Approximation Method in the Problem of Many Electrons. *The Journal of Chemical Physics*, 3(1):61–61, 1935.
- [106] D. R. Hamann, M. Schlüter, and C. Chiang. Norm-Conserving Pseudopotentials. *Phys. Rev. Lett.*, 43:1494–1497, Nov 1979.
- [107] D. Vanderbilt. Soft self-consistent pseudopotentials in a generalized eigenvalue formalism. *Phys. Rev. B*, 41:7892–7895, Apr 1990.
- [108] O. K. Andersen. Linear methods in band theory. *Phys. Rev. B*, 12:3060–3083, Oct 1975.
- [109] P. E. Blöchl. Projector augmented-wave method. *Phys. Rev. B*, 50:17953–17979, Dec 1994.
- [110] S. Baroni, S. de Gironcoli, A. Dal Corso, and P. Giannozzi. Phonons and related crystal properties from density-functional perturbation theory. *Rev. Mod. Phys.*, 73:515–562, Jul 2001.
- [111] S. Baroni, P. Giannozzi, and A. Testa. Green’s-function approach to linear response in solids. *Phys. Rev. Lett.*, 58:1861–1864, May 1987.
- [112] X. Gonze. Perturbation expansion of variational principles at arbitrary order. *Phys. Rev. A*, 52:1086–1095, Aug 1995.
- [113] R. D. King-Smith and D. Vanderbilt. Theory of polarization of crystalline solids. *Phys. Rev. B*, 47:1651–1654, Jan 1993.
- [114] R. Resta. Macroscopic polarization in crystalline dielectrics: the geometric phase approach. *Rev. Mod. Phys.*, 66:899–915, Jul 1994.
- [115] R. Resta and D. Vanderbilt. *Theory of Polarization: A Modern Approach*, pages 31–68. Springer Berlin Heidelberg, Berlin, Heidelberg, 2007.
- [116] X. Gonze, J.-M. Beuken, R. Caracas, F. Detraux, M. Fuchs, G.-M. Rignanese, L. Sindic, M. Verstraete, G. Zerah, F. Jollet, M. Torrent, A. Roy, M. Mikami, P. Ghosez, J.-Y.

Raty, and D. Allan. First-principles computation of material properties: the ABINIT software project. *Computational Materials Science*, 25(3):478 – 492, 2002.

- [117] X. Gonze, B. Amadon, P.-M. Anglade, J.-M. Beuken, F. Bottin, P. Boulanger, F. Bruneval, D. Caliste, R. Caracas, M. Côté, T. Deutsch, L. Genovese, P. Ghosez, M. Giantomassi, S. Goedecker, D. Hamann, P. Hermet, F. Jollet, G. Jomard, S. Leroux, M. Mancini, S. Mazevet, M. Oliveira, G. Onida, Y. Pouillon, T. Rangel, G.-M. Rignanese, D. Sangalli, R. Shaltaf, M. Torrent, M. Verstraete, G. Zerah, and J. Zwanziger. ABINIT: First-principles approach to material and nanosystem properties. *Computer Physics Communications*, 180(12):2582 – 2615, 2009. 40 YEARS OF CPC: A celebratory issue focused on quality software for high performance, grid and novel computing architectures.
- [118] X. Gonze, F. Jollet, F. A. Araujo, D. Adams, B. Amadon, T. Applencourt, C. Audouze, J.-M. Beuken, J. Bieder, A. Bokhanchuk, E. Bousquet, F. Bruneval, D. Caliste, M. Côté, F. Dahm, F. D. Pieve, M. Delaveau, M. D. Gennaro, B. Dorado, C. Espejo, G. Geneste, L. Genovese, A. Gerossier, M. Giantomassi, Y. Gillet, D. Hamann, L. He, G. Jomard, J. L. Janssen, S. L. Roux, A. Levitt, A. Lherbier, F. Liu, I. Lukačević, A. Martin, C. Martins, M. Oliveira, S. Poncé, Y. Pouillon, T. Rangel, G.-M. Rignanese, A. Romero, B. Rousseau, O. Rubel, A. Shukri, M. Stankovski, M. Torrent, M. V. Setten, B. V. Troeye, M. Verstraete, D. Waroquiers, J. Wiktor, B. Xu, A. Zhou, and J. Zwanziger. Recent developments in the ABINIT software package. *Computer Physics Communications*, 205:106 – 131, 2016.
- [119] F. Bottin, S. Leroux, A. Knyazev, and G. Zerah. Large-scale ab initio calculations based on three levels of parallelization. *Computational Materials Science*, 42(2):329 – 336, 2008.
- [120] X. Gonze. First-principles responses of solids to atomic displacements and homogeneous electric fields: Implementation of a conjugate-gradient algorithm. *Phys. Rev. B*, 55:10337–10354, Apr 1997.
- [121] X. Gonze and C. Lee. Dynamical matrices, Born effective charges, dielectric permittivity tensors, and interatomic force constants from density-functional perturbation theory. *Phys. Rev. B*, 55:10355–10368, Apr 1997.
- [122] M. Torrent, F. Jollet, F. Bottin, G. Zerah, and X. Gonze. Implementation of the projector augmented-wave method in the ABINIT code: Application to the study of iron under pressure. *Computational Materials Science*, 42(2):337 – 351, 2008.

- [123] K. F. Garrity, J. W. Bennett, K. M. Rabe, and D. Vanderbilt. GBRV high-throughput pseudopotentials (Website), 2017. <https://www.physics.rutgers.edu/gbrv/> (Access date: 18.06.2017).
- [124] K. F. Garrity, J. W. Bennett, K. M. Rabe, and D. Vanderbilt. Pseudopotentials for high-throughput DFT calculations. *Computational Materials Science*, 81:446 – 452, 2014.
- [125] P. Pulay. Convergence acceleration of iterative sequences. the case of scf iteration. *Chemical Physics Letters*, 73(2):393 – 398, 1980.
- [126] P. Pulay. Improved SCF convergence acceleration. *Journal of Computational Chemistry*, 3(4):556–560, 1982.
- [127] C. G. Broyden. The Convergence of a Class of Double-rank Minimization Algorithms 1. General Considerations. *IMA Journal of Applied Mathematics*, 6(1):76–90, 1970.
- [128] R. Fletcher. A new approach to variable metric algorithms. *The Computer Journal*, 13(3):317–322, 1970.
- [129] D. Goldfarb. A Family of Variable-Metric Methods Derived by Variational Means. *Mathematics of Computation*, 24(109):23–26, 1970.
- [130] D. F. Shanno. Conditioning of Quasi-Newton Methods for Function Minimization. *Mathematics of Computation*, 24(111):647–656, 1970.
- [131] H. J. Monkhorst and J. D. Pack. Special points for Brillouin-zone integrations. *Phys. Rev. B*, 13:5188–5192, Jun 1976.
- [132] D. R. Hamann, X. Wu, K. M. Rabe, and D. Vanderbilt. Metric tensor formulation of strain in density-functional perturbation theory. *Phys. Rev. B*, 71:035117, Jan 2005.
- [133] M. A. Parkes, K. Refson, M. d’Avezac, G. J. Offer, N. P. Brandon, and N. M. Harrison. Chemical Descriptors of Yttria-Stabilized Zirconia at Low Defect Concentration: An ab Initio Study. *The Journal of Physical Chemistry A*, 119(24):6412–6420, 2015. PMID: 25973648.
- [134] M. A. Parkes, D. A. Tompsett, M. d’Avezac, G. J. Offer, N. P. Brandon, and N. M. Harrison. The atomistic structure of yttria stabilised zirconia at 6.7 mol%: an ab initio study. *Phys. Chem. Chem. Phys.*, 18:31277–31285, 2016.
- [135] G. Makov and M. C. Payne. Periodic boundary conditions in ab initio calculations. *Phys. Rev. B*, 51:4014–4022, Feb 1995.

- [136] F. Bruneval, J.-P. Crocombette, X. Gonze, B. Dorado, M. Torrent, and F. Jollet. Consistent treatment of charged systems within periodic boundary conditions: The projector augmented-wave and pseudopotential methods revisited. *Phys. Rev. B*, 89:045116, Jan 2014.
- [137] N. Umezawa. Effects of barium incorporation into HfO₂ gate dielectrics on reduction in charged defects: First-principles study. *Applied Physics Letters*, 94(2):022903, 2009.
- [138] E. D. Grimley, T. Schenk, T. Mikolajick, U. Schroeder, and J. M. LeBeau. Atomic Structure of Domain and Interphase Boundaries in Ferroelectric HfO₂. *Advanced Materials Interfaces*, 5(5):1701258, 2018.
- [139] E. D. Grimley, T. Schenk, X. Sang, M. Pešić, U. Schroeder, T. Mikolajick, and J. M. LeBeau. Structural Changes Underlying Field-Cycling Phenomena in Ferroelectric HfO₂ Thin Films. *Advanced Electronic Materials*, 2(9):1600173–n/a, 2016. 1600173.
- [140] M. Pešić, F. P. G. Fengler, L. Larcher, A. Padovani, T. Schenk, E. D. Grimley, X. Sang, J. M. LeBeau, S. Slesazek, U. Schroeder, and T. Mikolajick. Physical Mechanisms behind the Field-Cycling Behavior of HfO₂-Based Ferroelectric Capacitors. *Advanced Functional Materials*, 26(25):4601–4612, 2016.
- [141] M. Hoffmann, U. Schroeder, T. Schenk, T. Shimizu, H. Funakubo, O. Sakata, D. Pohl, M. Drescher, C. Adelman, R. Materlik, A. Kersch, and T. Mikolajick. Stabilizing the ferroelectric phase in doped hafnium oxide. *Journal of Applied Physics*, 118(7):072006, 2015.
- [142] M. Hoffmann, U. Schroeder, C. Künneth, A. Kersch, S. Starschich, U. Böttger, and T. Mikolajick. Ferroelectric phase transitions in nanoscale HfO₂ films enable giant pyroelectric energy conversion and highly efficient supercapacitors. *Nano Energy*, 18:154 – 164, 2015.
- [143] M. H. Park, Y. H. Lee, H. J. Kim, T. Schenk, W. Lee, K. D. Kim, F. P. G. Fengler, T. Mikolajick, U. Schroeder, and C. S. Hwang. Surface and grain boundary energy as the key enabler of ferroelectricity in nanoscale hafnia-zirconia: a comparison of model and experiment. *Nanoscale*, 9:9973–9986, 2017.
- [144] C. Künneth, R. Materlik, and A. Kersch. Supplemental Materials of Modeling ferroelectric film properties and size effects from tetragonal interlayer in Hf_{1-x}Zr_xO₂ grains. *Journal of Applied Physics*, 121(20), 2017.
- [145] C. Künneth, R. Materlik, M. Falkowski, and A. Kersch. Impact of Four-Valent Doping on the Crystallographic Phase Formation for Ferroelectric HfO₂ from First-Principles:

Implications for Ferroelectric Memory and Energy-Related Applications. *ACS Applied Nano Materials*, 1(1):254–264, 2018.

- [146] V. N. Staroverov, G. E. Scuseria, J. Tao, and J. P. Perdew. Tests of a ladder of density functionals for bulk solids and surfaces. *Phys. Rev. B*, 69:075102, Feb 2004.
- [147] J. E. Jaffe, R. A. Bachorz, and M. Gutowski. Low-temperature polymorphs of ZrO_2 and HfO_2 : A density-functional theory study. *Phys. Rev. B*, 72:144107, Oct 2005.
- [148] R. Ruh and P. W. R. Corfield. Crystal Structure of Monoclinic Hafnia and Comparison with Monoclinic Zirconia. *Journal of the American Ceramic Society*, 53(3):126–129, 1970.
- [149] I. A. El-Shanshoury, V. A. Rudenko, and I. A. Ibrahim. Polymorphic Behavior of Thin Evaporated Films of Zirconium and Hafnium Oxides. *Journal of the American Ceramic Society*, 53(5):264–268, 1970.
- [150] R. Suyama, H. Takubo, and S. Kume. Synthesis of $\text{Hf}_{1-x}\text{Zr}_x\text{O}_2$ ($0 < x < 1$) with Orthorhombic Symmetry. *Journal of the American Ceramic Society*, 68(9):Page C–237, 1985.
- [151] I. MacLaren, T. Ras, M. MacKenzie, A. J. Craven, D. W. McComb, and S. De Gendt. Texture, Twinning, and Metastable “Tetragonal” Phase in Ultrathin Films of HfO_2 on a Si Substrate. *Journal of The Electrochemical Society*, 156(8):G103–G108, 2009.
- [152] G. Fadda, G. Zanzotto, and L. Colombo. First-principles study of the effect of pressure on the five zirconia polymorphs. I. Structural, vibrational, and thermoelastic properties. *Phys. Rev. B*, 82:064105, Aug 2010.
- [153] E. H. Kisi, C. J. Howard, and R. J. Hill. Crystal Structure of Orthorhombic Zirconia in Partially Stabilized Zirconia. *Journal of the American Ceramic Society*, 72(9):1757–1760, 1989.
- [154] F. Namavar, G. Wang, C. L. Cheung, R. F. Sabirianov, X. C. Zeng, W. N. Mei, J. Bai, J. R. Brewer, H. Haider, and K. L. Garvin. Thermal stability of nanostructurally stabilized zirconium oxide. *Nanotechnology*, 18(41):415702, 2007.
- [155] J. Robertson. High dielectric constant gate oxides for metal oxide Si transistors. *Reports on Progress in Physics*, 69(2):327, 2006.
- [156] H. Ledbetter, H. Ogi, and N. Nakamura. Elastic, anelastic, piezoelectric coefficients of monocrystal lithium niobate. *Mechanics of Materials*, 36(10):941 – 947, 2004. Active Materials.

- [157] J. Yang and G. Maugin. *Mechanics of Electromagnetic Solids*, page 117. Advances in Mechanics and Mathematics. Springer US, 2013.
- [158] F. P. G. Fengler, M. Hoffmann, S. Slesazek, T. Mikolajick, and U. Schroeder. On the relationship between field cycling and imprint in ferroelectric $\text{Hf}_{0.5}\text{Zr}_{0.5}\text{O}_2$. *Journal of Applied Physics*, 123(20):204101, 2018.
- [159] U. Schroeder, E. Yurchuk, J. Müller, D. Martin, T. Schenk, P. Polakowski, C. Adelman, M. I. Popovici, S. V. Kalinin, and T. Mikolajick. Impact of different dopants on the switching properties of ferroelectric hafniumoxide. *Japanese Journal of Applied Physics*, 53(8S1):08LE02, 2014.
- [160] M. H. Park, Y. H. Lee, H. J. Kim, Y. J. Kim, T. Moon, K. D. Kim, J. Müller, A. Kersch, U. Schroeder, T. Mikolajick, and C. S. Hwang. Ferroelectricity and Antiferroelectricity of Doped Thin HfO_2 -Based Films. *Advanced Materials*, 27(11):1811–1831, 2015.
- [161] M. W. Hooker. Properties of PZT-Based Piezoelectric Ceramics Between -150 and 250 C. *NASA/CR-1998-208708*, Sep 1998.
- [162] R. Batra, T. D. Huan, J. L. Jones, G. Rossetti, and R. Ramprasad. Factors Favoring Ferroelectricity in Hafnia: A First-Principles Computational Study. *The Journal of Physical Chemistry C*, 121(8):4139–4145, 2017.
- [163] T. Böske. *Crystalline Hafnia and Zirconia Based Dielectrics for Memory Applications*. PhD thesis, Technische Universität Hamburg-Harburg, 01 2010.
- [164] M. H. Park, C.-C. Chung, T. Schenk, C. Richter, M. Hoffmann, S. Wirth, J. L. Jones, T. Mikolajick, and U. Schroeder. Origin of Temperature-Dependent Ferroelectricity in Si-Doped HfO_2 . *Advanced Electronic Materials*, 4(4):1700489, 2018.
- [165] R. A. Van Santen. The Ostwald step rule. *The Journal of Physical Chemistry*, 88(24):5768–5769, 1984.
- [166] T. S. Böske, J. Müller, D. Bräuhäus, U. Schröder, and U. Böttger. Ferroelectricity in hafnium oxide: CMOS compatible ferroelectric field effect transistors. In *2011 International Electron Devices Meeting*, pages 24.5.1–24.5.4, Dec 2011.
- [167] M. H. Park, C.-C. Chung, T. Schenk, C. Richter, K. Opsomer, C. Detavernier, C. Adelman, J. L. Jones, T. Mikolajick, and U. Schroeder. Effect of Annealing Ferroelectric HfO_2 Thin Films: In Situ, High Temperature X-Ray Diffraction. *Advanced Electronic Materials*, 4(7):1800091, 2018.

- [168] R. Materlik, C. Künneth, T. Mikolajick, and A. Kersch. The impact of charge compensated and uncompensated strontium defects on the stabilization of the ferroelectric phase in HfO_2 . *Applied Physics Letters*, 111(8):082902, 2017.
- [169] R. Materlik, C. Künneth, M. Falkowski, T. Mikolajick, and A. Kersch. Al-, Y-, and La-doping effects favoring intrinsic and field induced ferroelectricity in HfO_2 : A first principles study. *Journal of Applied Physics*, 123(16):164101, 2018.
- [170] M. Falkowski, C. Künneth, R. Materlik, and A. Kersch. Unexpectedly large energy variations from dopant interactions in ferroelectric HfO_2 from high-throughput ab initio calculations. *npj Computational Materials*, 4(1):2057–3960, 2018.
- [171] Z. F. Hou, X. G. Gong, and Q. Li. Energetics and electronic structure of aluminum point defects in HfO_2 : A first-principles study. *Journal of Applied Physics*, 106(1):014104, 2009.

Appendix A

Wyckoff positions

Table 6.1 displays the Multiplicity, Wyckoff letter, and Wyckoff positions of common HfO₂ phases. The same Wyckoff positions can be used to generate ZrO₂ phases but may require further relaxation.

TABLE 6.1: Multiplicity, Wyckoff letter, and Wyckoff positions of common HfO₂ phases.

		Multiplicity	Wyckoff letter	x	y	z
m-phase	Hf1	4	e	-0.22309	0.45872	0.20806
	O1	4	e	-0.42903	0.16384	0.34216
	O2	4	e	0.05192	0.24233	0.01878
o-phase	Hf1	8	c	-0.36193	-0.45921	-0.15654
	O1	8	c	0.03176	-0.17534	-0.16042
	O2	8	c	-0.22499	-0.25169	0.08934
f-phase	Hf1	4	a	0.26700	0.03200	0.25700
	O1	4	a	0.06800	0.38900	0.11200
	O2	4	a	0.53700	0.26700	0.50800
f'-phase	Hf1	2	a	0.00000	-0.26306	-0.24442
	O1	2	a	0.00000	0.07198	0.41230
	O2	2	a	0.00000	-0.44299	0.26207
t-phase	Hf1	2	a			
	O1	4	d			0.29439
c-phase	Hf1	1	a			
	O1	2	c			

Ion position

This section displays the HfO₂ input ion positions of 96 atomic supercells in relative coordinates. Smaller cells can be easily be constructed from these basic cells. Hf may be replaced by Zr for ZrO₂ and Hf_{1-x}Zr_xO₂.

TABLE 6.2: Ion positions of the m-phase

Ion	index	x	y	z
Hf	1	0.0000000000E+00	0.0000000000E+00	0.0000000000E+00
Hf	2	0.0000000000E+00	2.0872077280E-01	2.5000000000E-01
Hf	3	2.2308854445E-01	2.5000000000E-01	4.5806126062E-01
Hf	4	2.2308854445E-01	4.5872077280E-01	2.0806126062E-01
O	5	3.9703086583E-01	1.4743789620E-01	4.3295141269E-01
O	6	3.9703086583E-01	6.1282876602E-02	1.8295141269E-01
O	7	3.2605767863E-01	3.9743789620E-01	2.5109847935E-02
O	8	3.2605767863E-01	3.1128287660E-01	2.7510984794E-01
O	9	1.3750673137E-01	1.0819504156E-01	9.4640671990E-02
O	10	1.3750673137E-01	1.0052573124E-01	3.4464067199E-01
O	11	8.5581813085E-02	3.5819504156E-01	3.6342058863E-01
O	12	8.5581813085E-02	3.5052573124E-01	1.1342058863E-01
Hf	13	0.0000000000E+00	0.0000000000E+00	5.0000000000E-01
Hf	14	0.0000000000E+00	2.0872077280E-01	7.5000000000E-01
Hf	15	2.2308854445E-01	2.5000000000E-01	9.5806126062E-01
Hf	16	2.2308854445E-01	4.5872077280E-01	7.0806126062E-01
O	17	3.9703086583E-01	1.4743789620E-01	9.3295141269E-01
O	18	3.9703086583E-01	6.1282876602E-02	6.8295141269E-01
O	19	3.2605767863E-01	3.9743789620E-01	5.2510984794E-01
O	20	3.2605767863E-01	3.1128287660E-01	7.7510984794E-01
O	21	1.3750673137E-01	1.0819504156E-01	5.9464067199E-01
O	22	1.3750673137E-01	1.0052573124E-01	8.4464067199E-01
O	23	8.5581813085E-02	3.5819504156E-01	8.6342058863E-01
O	24	8.5581813085E-02	3.5052573124E-01	6.1342058863E-01
Hf	25	0.0000000000E+00	5.0000000000E-01	0.0000000000E+00
Hf	26	0.0000000000E+00	7.0872077280E-01	2.5000000000E-01
Hf	27	2.2308854445E-01	7.5000000000E-01	4.5806126062E-01
Hf	28	2.2308854445E-01	9.5872077280E-01	2.0806126062E-01
O	29	3.9703086583E-01	6.4743789620E-01	4.3295141269E-01
O	30	3.9703086583E-01	5.6128287660E-01	1.8295141269E-01
O	31	3.2605767863E-01	8.9743789620E-01	2.5109847935E-02
O	32	3.2605767863E-01	8.1128287660E-01	2.7510984794E-01
O	33	1.3750673137E-01	6.0819504156E-01	9.4640671990E-02
O	34	1.3750673137E-01	6.0052573124E-01	3.4464067199E-01
O	35	8.5581813085E-02	8.5819504156E-01	3.6342058863E-01
O	36	8.5581813085E-02	8.5052573124E-01	1.1342058863E-01
Hf	37	0.0000000000E+00	5.0000000000E-01	5.0000000000E-01
Hf	38	0.0000000000E+00	7.0872077280E-01	7.5000000000E-01
Hf	39	2.2308854445E-01	7.5000000000E-01	9.5806126062E-01
Hf	40	2.2308854445E-01	9.5872077280E-01	7.0806126062E-01
O	41	3.9703086583E-01	6.4743789620E-01	9.3295141269E-01
O	42	3.9703086583E-01	5.6128287660E-01	6.8295141269E-01
O	43	3.2605767863E-01	8.9743789620E-01	5.2510984794E-01
O	44	3.2605767863E-01	8.1128287660E-01	7.7510984794E-01
O	45	1.3750673137E-01	6.0819504156E-01	5.9464067199E-01
O	46	1.3750673137E-01	6.0052573124E-01	8.4464067199E-01
O	47	8.5581813085E-02	8.5819504156E-01	8.6342058863E-01
O	48	8.5581813085E-02	8.5052573124E-01	6.1342058863E-01

Ion	index	x	y	z
Hf	49	5.0000000000E-01	0.0000000000E+00	0.0000000000E+00
Hf	50	5.0000000000E-01	2.0872077280E-01	2.5000000000E-01
Hf	51	7.2308854445E-01	2.5000000000E-01	4.5806126062E-01
Hf	52	7.2308854445E-01	4.5872077280E-01	2.0806126062E-01
O	53	8.9703086583E-01	1.4743789620E-01	4.3295141269E-01
O	54	8.9703086583E-01	6.1282876602E-02	1.8295141269E-01
O	55	8.2605767863E-01	3.9743789620E-01	2.5109847935E-02
O	56	8.2605767863E-01	3.1128287660E-01	2.7510984794E-01
O	57	6.3750673137E-01	1.0819504156E-01	9.4640671990E-02
O	58	6.3750673137E-01	1.0052573124E-01	3.4464067199E-01
O	59	5.8558181309E-01	3.5819504156E-01	3.6342058863E-01
O	60	5.8558181309E-01	3.5052573124E-01	1.1342058863E-01
Hf	61	5.0000000000E-01	0.0000000000E+00	5.0000000000E-01
Hf	62	5.0000000000E-01	2.0872077280E-01	7.5000000000E-01
Hf	63	7.2308854445E-01	2.5000000000E-01	9.5806126062E-01
Hf	64	7.2308854445E-01	4.5872077280E-01	7.0806126062E-01
O	65	8.9703086583E-01	1.4743789620E-01	9.3295141269E-01
O	66	8.9703086583E-01	6.1282876602E-02	6.8295141269E-01
O	67	8.2605767863E-01	3.9743789620E-01	5.2510984794E-01
O	68	8.2605767863E-01	3.1128287660E-01	7.7510984794E-01
O	69	6.3750673137E-01	1.0819504156E-01	5.9464067199E-01
O	70	6.3750673137E-01	1.0052573124E-01	8.4464067199E-01
O	71	5.8558181309E-01	3.5819504156E-01	8.6342058863E-01
O	72	5.8558181309E-01	3.5052573124E-01	6.1342058863E-01
Hf	73	5.0000000000E-01	5.0000000000E-01	0.0000000000E+00
Hf	74	5.0000000000E-01	7.0872077280E-01	2.5000000000E-01
Hf	75	7.2308854445E-01	7.5000000000E-01	4.5806126062E-01
Hf	76	7.2308854445E-01	9.5872077280E-01	2.0806126062E-01
O	77	8.9703086583E-01	6.4743789620E-01	4.3295141269E-01
O	78	8.9703086583E-01	5.6128287660E-01	1.8295141269E-01
O	79	8.2605767863E-01	8.9743789620E-01	2.5109847935E-02
O	80	8.2605767863E-01	8.1128287660E-01	2.7510984794E-01
O	81	6.3750673137E-01	6.0819504156E-01	9.4640671990E-02
O	82	6.3750673137E-01	6.0052573124E-01	3.4464067199E-01
O	83	5.8558181309E-01	8.5819504156E-01	3.6342058863E-01
O	84	5.8558181309E-01	8.5052573124E-01	1.1342058863E-01
Hf	85	5.0000000000E-01	5.0000000000E-01	5.0000000000E-01
Hf	86	5.0000000000E-01	7.0872077280E-01	7.5000000000E-01
Hf	87	7.2308854445E-01	7.5000000000E-01	9.5806126062E-01
Hf	88	7.2308854445E-01	9.5872077280E-01	7.0806126062E-01
O	89	8.9703086583E-01	6.4743789620E-01	9.3295141269E-01
O	90	8.9703086583E-01	5.6128287660E-01	6.8295141269E-01
O	91	8.2605767863E-01	8.9743789620E-01	5.2510984794E-01
O	92	8.2605767863E-01	8.1128287660E-01	7.7510984794E-01
O	93	6.3750673137E-01	6.0819504156E-01	5.9464067199E-01
O	94	6.3750673137E-01	6.0052573124E-01	8.4464067199E-01
O	95	5.8558181309E-01	8.5819504156E-01	8.6342058863E-01
O	96	5.8558181309E-01	8.5052573124E-01	6.1342058863E-01

TABLE 6.3: Ion positions of the f-phase

Ion	index	x	y	z
Hf	1	0.0000000000E+00	0.0000000000E+00	0.0000000000E+00
Hf	2	0.0000000000E+00	2.1858414750E-01	2.5000000000E-01
Hf	3	2.3246872962E-01	2.5000000000E-01	5.0000000000E-01
Hf	4	2.3246872962E-01	4.6858414750E-01	2.5000000000E-01
O	5	4.0154124444E-01	1.6784920737E-01	4.3083064090E-01
O	6	4.0154124444E-01	5.0734940134E-02	1.8083064090E-01
O	7	3.3092748518E-01	3.0073494013E-01	1.8083064090E-01
O	8	3.3092748518E-01	4.1784920737E-01	4.3083064090E-01
O	9	1.3556014234E-01	1.1766924689E-01	1.2654485446E-01
O	10	1.3556014234E-01	1.0091490062E-01	3.7654485445E-01
O	11	9.6908587280E-02	3.5091490062E-01	3.7654485445E-01
O	12	9.6908587280E-02	3.6766924689E-01	1.2654485446E-01
Hf	13	0.0000000000E+00	0.0000000000E+00	5.0000000000E-01
Hf	14	0.0000000000E+00	2.1858414750E-01	7.5000000000E-01
Hf	15	2.3246872962E-01	2.5000000000E-01	1.0000000000E+00
Hf	16	2.3246872962E-01	4.6858414750E-01	7.5000000000E-01
O	17	4.0154124444E-01	1.6784920737E-01	9.3083064090E-01
O	18	4.0154124444E-01	5.0734940134E-02	6.8083064090E-01
O	19	3.3092748518E-01	3.0073494013E-01	6.8083064090E-01
O	20	3.3092748518E-01	4.1784920737E-01	9.3083064090E-01
O	21	1.3556014234E-01	1.1766924689E-01	6.2654485446E-01
O	22	1.3556014234E-01	1.0091490062E-01	8.7654485445E-01
O	23	9.6908587280E-02	3.5091490062E-01	8.7654485445E-01
O	24	9.6908587280E-02	3.6766924689E-01	6.2654485446E-01
Hf	25	0.0000000000E+00	5.0000000000E-01	0.0000000000E+00
Hf	26	0.0000000000E+00	7.1858414750E-01	2.5000000000E-01
Hf	27	2.3246872962E-01	7.5000000000E-01	5.0000000000E-01
Hf	28	2.3246872962E-01	9.6858414750E-01	2.5000000000E-01
O	29	4.0154124444E-01	6.6784920737E-01	4.3083064090E-01
O	30	4.0154124444E-01	5.5073494013E-01	1.8083064090E-01
O	31	3.3092748518E-01	8.0073494013E-01	1.8083064090E-01
O	32	3.3092748518E-01	9.1784920737E-01	4.3083064090E-01
O	33	1.3556014234E-01	6.1766924689E-01	1.2654485446E-01
O	34	1.3556014234E-01	6.0091490062E-01	3.7654485445E-01
O	35	9.6908587280E-02	8.5091490062E-01	3.7654485445E-01
O	36	9.6908587280E-02	8.6766924689E-01	1.2654485446E-01
Hf	37	0.0000000000E+00	5.0000000000E-01	5.0000000000E-01
Hf	38	0.0000000000E+00	7.1858414750E-01	7.5000000000E-01
Hf	39	2.3246872962E-01	7.5000000000E-01	1.0000000000E+00
Hf	40	2.3246872962E-01	9.6858414750E-01	7.5000000000E-01
O	41	4.0154124444E-01	6.6784920737E-01	9.3083064090E-01
O	42	4.0154124444E-01	5.5073494013E-01	6.8083064090E-01
O	43	3.3092748518E-01	8.0073494013E-01	6.8083064090E-01
O	44	3.3092748518E-01	9.1784920737E-01	9.3083064090E-01
O	45	1.3556014234E-01	6.1766924689E-01	6.2654485446E-01
O	46	1.3556014234E-01	6.0091490062E-01	8.7654485445E-01
O	47	9.6908587280E-02	8.5091490062E-01	8.7654485445E-01
O	48	9.6908587280E-02	8.6766924689E-01	6.2654485446E-01

Ion	index	x	y	z
Hf	49	5.0000000000E-01	0.0000000000E+00	0.0000000000E+00
Hf	50	5.0000000000E-01	2.1858414750E-01	2.5000000000E-01
Hf	51	7.3246872962E-01	2.5000000000E-01	5.0000000000E-01
Hf	52	7.3246872962E-01	4.6858414750E-01	2.5000000000E-01
O	53	9.0154124444E-01	1.6784920737E-01	4.3083064090E-01
O	54	9.0154124444E-01	5.0734940134E-02	1.8083064090E-01
O	55	8.3092748518E-01	3.0073494013E-01	1.8083064090E-01
O	56	8.3092748518E-01	4.1784920737E-01	4.3083064090E-01
O	57	6.3556014234E-01	1.1766924689E-01	1.2654485446E-01
O	58	6.3556014234E-01	1.0091490062E-01	3.7654485445E-01
O	59	5.9690858728E-01	3.5091490062E-01	3.7654485445E-01
O	60	5.9690858728E-01	3.6766924689E-01	1.2654485446E-01
Hf	61	5.0000000000E-01	0.0000000000E+00	5.0000000000E-01
Hf	62	5.0000000000E-01	2.1858414750E-01	7.5000000000E-01
Hf	63	7.3246872962E-01	2.5000000000E-01	1.0000000000E+00
Hf	64	7.3246872962E-01	4.6858414750E-01	7.5000000000E-01
O	65	9.0154124444E-01	1.6784920737E-01	9.3083064090E-01
O	66	9.0154124444E-01	5.0734940134E-02	6.8083064090E-01
O	67	8.3092748518E-01	3.0073494013E-01	6.8083064090E-01
O	68	8.3092748518E-01	4.1784920737E-01	9.3083064090E-01
O	69	6.3556014234E-01	1.1766924689E-01	6.2654485446E-01
O	70	6.3556014234E-01	1.0091490062E-01	8.7654485445E-01
O	71	5.9690858728E-01	3.5091490062E-01	8.7654485445E-01
O	72	5.9690858728E-01	3.6766924689E-01	6.2654485446E-01
Hf	73	5.0000000000E-01	5.0000000000E-01	0.0000000000E+00
Hf	74	5.0000000000E-01	7.1858414750E-01	2.5000000000E-01
Hf	75	7.3246872962E-01	7.5000000000E-01	5.0000000000E-01
Hf	76	7.3246872962E-01	9.6858414750E-01	2.5000000000E-01
O	77	9.0154124444E-01	6.6784920737E-01	4.3083064090E-01
O	78	9.0154124444E-01	5.5073494013E-01	1.8083064090E-01
O	79	8.3092748518E-01	8.0073494013E-01	1.8083064090E-01
O	80	8.3092748518E-01	9.1784920737E-01	4.3083064090E-01
O	81	6.3556014234E-01	6.1766924689E-01	1.2654485446E-01
O	82	6.3556014234E-01	6.0091490062E-01	3.7654485445E-01
O	83	5.9690858728E-01	8.5091490062E-01	3.7654485445E-01
O	84	5.9690858728E-01	8.6766924689E-01	1.2654485446E-01
Hf	85	5.0000000000E-01	5.0000000000E-01	5.0000000000E-01
Hf	86	5.0000000000E-01	7.1858414750E-01	7.5000000000E-01
Hf	87	7.3246872962E-01	7.5000000000E-01	1.0000000000E+00
Hf	88	7.3246872962E-01	9.6858414750E-01	7.5000000000E-01
O	89	9.0154124444E-01	6.6784920737E-01	9.3083064090E-01
O	90	9.0154124444E-01	5.5073494013E-01	6.8083064090E-01
O	91	8.3092748518E-01	8.0073494013E-01	6.8083064090E-01
O	92	8.3092748518E-01	9.1784920737E-01	9.3083064090E-01
O	93	6.3556014234E-01	6.1766924689E-01	6.2654485446E-01
O	94	6.3556014234E-01	6.0091490062E-01	8.7654485445E-01
O	95	5.9690858728E-01	8.5091490062E-01	8.7654485445E-01
O	96	5.9690858728E-01	8.6766924689E-01	6.2654485446E-01

TABLE 6.4: Ion positions of the f¹-phase

Ion	index	x	y	z
Hf	1	0.0000000000E+00	0.0000000000E+00	0.0000000000E+00
Hf	2	2.5000000000E-01	2.6306000350E-01	0.0000000000E+00
Hf	3	2.5000000000E-01	0.0000000000E+00	2.5000000000E-01
Hf	4	0.0000000000E+00	2.6306000350E-01	2.5000000000E-01
O	5	4.1418001050E-01	1.6751998650E-01	4.1418001050E-01
O	6	4.1418001050E-01	9.5540002000E-02	1.6417999550E-01
O	7	3.7662249800E-01	4.1003501400E-01	3.7662249800E-01
O	8	3.7662249800E-01	3.5302501900E-01	1.2662249800E-01
O	9	1.6417999550E-01	1.6751998650E-01	1.6417999550E-01
O	10	1.6417999550E-01	9.5540002000E-02	4.1418001050E-01
O	11	1.2662249800E-01	4.1003501400E-01	1.2662249800E-01
O	12	1.2662249800E-01	3.5302501900E-01	3.7662249800E-01
Hf	13	0.0000000000E+00	0.0000000000E+00	5.0000000000E-01
Hf	14	2.5000000000E-01	2.6306000350E-01	5.0000000000E-01
Hf	15	2.5000000000E-01	0.0000000000E+00	7.5000000000E-01
Hf	16	0.0000000000E+00	2.6306000350E-01	7.5000000000E-01
O	17	4.1418001050E-01	1.6751998650E-01	9.1418001050E-01
O	18	4.1418001050E-01	9.5540002000E-02	6.6417999550E-01
O	19	3.7662249800E-01	4.1003501400E-01	8.7662249800E-01
O	20	3.7662249800E-01	3.5302501900E-01	6.2662249800E-01
O	21	1.6417999550E-01	1.6751998650E-01	6.6417999550E-01
O	22	1.6417999550E-01	9.5540002000E-02	9.1418001050E-01
O	23	1.2662249800E-01	4.1003501400E-01	6.2662249800E-01
O	24	1.2662249800E-01	3.5302501900E-01	8.7662249800E-01
Hf	25	0.0000000000E+00	5.0000000000E-01	0.0000000000E+00
Hf	26	2.5000000000E-01	7.6306000350E-01	0.0000000000E+00
Hf	27	2.5000000000E-01	5.0000000000E-01	2.5000000000E-01
Hf	28	0.0000000000E+00	7.6306000350E-01	2.5000000000E-01
O	29	4.1418001050E-01	6.6751998650E-01	4.1418001050E-01
O	30	4.1418001050E-01	5.9554000200E-01	1.6417999550E-01
O	31	3.7662249800E-01	9.1003501400E-01	3.7662249800E-01
O	32	3.7662249800E-01	8.5302501900E-01	1.2662249800E-01
O	33	1.6417999550E-01	6.6751998650E-01	1.6417999550E-01
O	34	1.6417999550E-01	5.9554000200E-01	4.1418001050E-01
O	35	1.2662249800E-01	9.1003501400E-01	1.2662249800E-01
O	36	1.2662249800E-01	8.5302501900E-01	3.7662249800E-01
Hf	37	0.0000000000E+00	5.0000000000E-01	5.0000000000E-01
Hf	38	2.5000000000E-01	7.6306000350E-01	5.0000000000E-01
Hf	39	2.5000000000E-01	5.0000000000E-01	7.5000000000E-01
Hf	40	0.0000000000E+00	7.6306000350E-01	7.5000000000E-01
O	41	4.1418001050E-01	6.6751998650E-01	9.1418001050E-01
O	42	4.1418001050E-01	5.9554000200E-01	6.6417999550E-01
O	43	3.7662249800E-01	9.1003501400E-01	8.7662249800E-01
O	44	3.7662249800E-01	8.5302501900E-01	6.2662249800E-01
O	45	1.6417999550E-01	6.6751998650E-01	6.6417999550E-01
O	46	1.6417999550E-01	5.9554000200E-01	9.1418001050E-01
O	47	1.2662249800E-01	9.1003501400E-01	6.2662249800E-01
O	48	1.2662249800E-01	8.5302501900E-01	8.7662249800E-01

Ion	index	x	y	z
Hf	49	5.0000000000E-01	0.0000000000E+00	0.0000000000E+00
Hf	50	7.5000000000E-01	2.6306000350E-01	0.0000000000E+00
Hf	51	7.5000000000E-01	0.0000000000E+00	2.5000000000E-01
Hf	52	5.0000000000E-01	2.6306000350E-01	2.5000000000E-01
O	53	9.1418001050E-01	1.6751998650E-01	4.1418001050E-01
O	54	9.1418001050E-01	9.5540002000E-02	1.6417999550E-01
O	55	8.7662249800E-01	4.1003501400E-01	3.7662249800E-01
O	56	8.7662249800E-01	3.5302501900E-01	1.2662249800E-01
O	57	6.6417999550E-01	1.6751998650E-01	1.6417999550E-01
O	58	6.6417999550E-01	9.5540002000E-02	4.1418001050E-01
O	59	6.2662249800E-01	4.1003501400E-01	1.2662249800E-01
O	60	6.2662249800E-01	3.5302501900E-01	3.7662249800E-01
Hf	61	5.0000000000E-01	0.0000000000E+00	5.0000000000E-01
Hf	62	7.5000000000E-01	2.6306000350E-01	5.0000000000E-01
Hf	63	7.5000000000E-01	0.0000000000E+00	7.5000000000E-01
Hf	64	5.0000000000E-01	2.6306000350E-01	7.5000000000E-01
O	65	9.1418001050E-01	1.6751998650E-01	9.1418001050E-01
O	66	9.1418001050E-01	9.5540002000E-02	6.6417999550E-01
O	67	8.7662249800E-01	4.1003501400E-01	8.7662249800E-01
O	68	8.7662249800E-01	3.5302501900E-01	6.2662249800E-01
O	69	6.6417999550E-01	1.6751998650E-01	6.6417999550E-01
O	70	6.6417999550E-01	9.5540002000E-02	9.1418001050E-01
O	71	6.2662249800E-01	4.1003501400E-01	6.2662249800E-01
O	72	6.2662249800E-01	3.5302501900E-01	8.7662249800E-01
Hf	73	5.0000000000E-01	5.0000000000E-01	0.0000000000E+00
Hf	74	7.5000000000E-01	7.6306000350E-01	0.0000000000E+00
Hf	75	7.5000000000E-01	5.0000000000E-01	2.5000000000E-01
Hf	76	5.0000000000E-01	7.6306000350E-01	2.5000000000E-01
O	77	9.1418001050E-01	6.6751998650E-01	4.1418001050E-01
O	78	9.1418001050E-01	5.9554000200E-01	1.6417999550E-01
O	79	8.7662249800E-01	9.1003501400E-01	3.7662249800E-01
O	80	8.7662249800E-01	8.5302501900E-01	1.2662249800E-01
O	81	6.6417999550E-01	6.6751998650E-01	1.6417999550E-01
O	82	6.6417999550E-01	5.9554000200E-01	4.1418001050E-01
O	83	6.2662249800E-01	9.1003501400E-01	1.2662249800E-01
O	84	6.2662249800E-01	8.5302501900E-01	3.7662249800E-01
Hf	85	5.0000000000E-01	5.0000000000E-01	5.0000000000E-01
Hf	86	7.5000000000E-01	7.6306000350E-01	5.0000000000E-01
Hf	87	7.5000000000E-01	5.0000000000E-01	7.5000000000E-01
Hf	88	5.0000000000E-01	7.6306000350E-01	7.5000000000E-01
O	89	9.1418001050E-01	6.6751998650E-01	9.1418001050E-01
O	90	9.1418001050E-01	5.9554000200E-01	6.6417999550E-01
O	91	8.7662249800E-01	9.1003501400E-01	8.7662249800E-01
O	92	8.7662249800E-01	8.5302501900E-01	6.2662249800E-01
O	93	6.6417999550E-01	6.6751998650E-01	6.6417999550E-01
O	94	6.6417999550E-01	5.9554000200E-01	9.1418001050E-01
O	95	6.2662249800E-01	9.1003501400E-01	6.2662249800E-01
O	96	6.2662249800E-01	8.5302501900E-01	8.7662249800E-01

TABLE 6.5: Ion positions of the o-phase

Ion	index	x	y	z
Hf	1	0.0000000000E+00	0.0000000000E+00	0.0000000000E+00
Hf	2	0.0000000000E+00	2.0920989349E-01	2.5000000000E-01
Hf	3	2.2386978589E-01	2.5000000000E-01	5.0000000000E-01
Hf	4	2.2386978589E-01	4.5920989349E-01	2.5000000000E-01
O	5	3.9369973390E-01	1.4193717359E-01	4.9806087819E-01
O	6	3.9369973390E-01	6.7272719905E-02	2.4806087819E-01
O	7	3.3017005199E-01	3.1727271991E-01	1.5848108456E-01
O	8	3.3017005199E-01	3.9193717359E-01	4.0848108456E-01
O	9	1.3694956969E-01	1.0375826031E-01	1.2294234625E-01
O	10	1.3694956969E-01	1.0545163318E-01	3.7294234625E-01
O	11	8.6920216193E-02	3.5545163318E-01	3.7294234625E-01
O	12	8.6920216193E-02	3.5375826031E-01	1.2294234625E-01
Hf	13	0.0000000000E+00	0.0000000000E+00	5.0000000000E-01
Hf	14	0.0000000000E+00	2.0920989349E-01	7.5000000000E-01
Hf	15	2.2386978589E-01	2.5000000000E-01	1.0000000000E+00
Hf	16	2.2386978589E-01	4.5920989349E-01	7.5000000000E-01
O	17	3.9369973390E-01	1.4193717359E-01	9.9806087819E-01
O	18	3.9369973390E-01	6.7272719905E-02	7.4806087819E-01
O	19	3.3017005199E-01	3.1727271991E-01	6.5848108456E-01
O	20	3.3017005199E-01	3.9193717359E-01	9.0848108456E-01
O	21	1.3694956969E-01	1.0375826031E-01	6.2294234625E-01
O	22	1.3694956969E-01	1.0545163318E-01	8.7294234625E-01
O	23	8.6920216193E-02	3.5545163318E-01	8.7294234625E-01
O	24	8.6920216193E-02	3.5375826031E-01	6.2294234625E-01
Hf	25	0.0000000000E+00	5.0000000000E-01	0.0000000000E+00
Hf	26	0.0000000000E+00	7.0920989349E-01	2.5000000000E-01
Hf	27	2.2386978589E-01	7.5000000000E-01	5.0000000000E-01
Hf	28	2.2386978589E-01	9.5920989349E-01	2.5000000000E-01
O	29	3.9369973390E-01	6.4193717359E-01	4.9806087819E-01
O	30	3.9369973390E-01	5.6727271991E-01	2.4806087819E-01
O	31	3.3017005199E-01	8.1727271991E-01	1.5848108456E-01
O	32	3.3017005199E-01	8.9193717359E-01	4.0848108456E-01
O	33	1.3694956969E-01	6.0375826031E-01	1.2294234625E-01
O	34	1.3694956969E-01	6.0545163318E-01	3.7294234625E-01
O	35	8.6920216193E-02	8.5545163318E-01	3.7294234625E-01
O	36	8.6920216193E-02	8.5375826031E-01	1.2294234625E-01
Hf	37	0.0000000000E+00	5.0000000000E-01	5.0000000000E-01
Hf	38	0.0000000000E+00	7.0920989349E-01	7.5000000000E-01
Hf	39	2.2386978589E-01	7.5000000000E-01	1.0000000000E+00
Hf	40	2.2386978589E-01	9.5920989349E-01	7.5000000000E-01
O	41	3.9369973390E-01	6.4193717359E-01	9.9806087819E-01
O	42	3.9369973390E-01	5.6727271991E-01	7.4806087819E-01
O	43	3.3017005199E-01	8.1727271991E-01	6.5848108456E-01
O	44	3.3017005199E-01	8.9193717359E-01	9.0848108456E-01
O	45	1.3694956969E-01	6.0375826031E-01	6.2294234625E-01
O	46	1.3694956969E-01	6.0545163318E-01	8.7294234625E-01
O	47	8.6920216193E-02	8.5545163318E-01	8.7294234625E-01
O	48	8.6920216193E-02	8.5375826031E-01	6.2294234625E-01

Ion	index	x	y	z
Hf	49	5.0000000000E-01	0.0000000000E+00	4.0654196275E-01
Hf	50	5.0000000000E-01	2.0920989349E-01	1.5654196275E-01
Hf	51	7.2386978589E-01	2.5000000000E-01	4.0654196275E-01
Hf	52	7.2386978589E-01	4.5920989349E-01	1.5654196275E-01
O	53	8.9369973390E-01	1.4193717359E-01	4.0848108456E-01
O	54	8.9369973390E-01	6.7272719905E-02	1.5848108456E-01
O	55	8.3017005199E-01	3.1727271991E-01	2.4806087819E-01
O	56	8.3017005199E-01	3.9193717359E-01	4.9806087819E-01
O	57	6.3694956969E-01	1.0545163318E-01	3.3599616507E-02
O	58	6.3694956969E-01	1.0375826031E-01	2.8359961651E-01
O	59	5.8692021619E-01	3.5375826031E-01	2.8359961651E-01
O	60	5.8692021619E-01	3.5545163318E-01	3.3599616507E-02
Hf	61	5.0000000000E-01	0.0000000000E+00	9.0654196275E-01
Hf	62	5.0000000000E-01	2.0920989349E-01	6.5654196275E-01
Hf	63	7.2386978589E-01	2.5000000000E-01	9.0654196275E-01
Hf	64	7.2386978589E-01	4.5920989349E-01	6.5654196275E-01
O	65	8.9369973390E-01	1.4193717359E-01	9.0848108456E-01
O	66	8.9369973390E-01	6.7272719905E-02	6.5848108456E-01
O	67	8.3017005199E-01	3.1727271991E-01	7.4806087819E-01
O	68	8.3017005199E-01	3.9193717359E-01	9.9806087819E-01
O	69	6.3694956969E-01	1.0545163318E-01	5.3359961651E-01
O	70	6.3694956969E-01	1.0375826031E-01	7.8359961651E-01
O	71	5.8692021619E-01	3.5375826031E-01	7.8359961651E-01
O	72	5.8692021619E-01	3.5545163318E-01	5.3359961651E-01
Hf	73	5.0000000000E-01	5.0000000000E-01	4.0654196275E-01
Hf	74	5.0000000000E-01	7.0920989349E-01	1.5654196275E-01
Hf	75	7.2386978589E-01	7.5000000000E-01	4.0654196275E-01
Hf	76	7.2386978589E-01	9.5920989349E-01	1.5654196275E-01
O	77	8.9369973390E-01	6.4193717359E-01	4.0848108456E-01
O	78	8.9369973390E-01	5.6727271991E-01	1.5848108456E-01
O	79	8.3017005199E-01	8.1727271991E-01	2.4806087819E-01
O	80	8.3017005199E-01	8.9193717359E-01	4.9806087819E-01
O	81	6.3694956969E-01	6.0545163318E-01	3.3599616507E-02
O	82	6.3694956969E-01	6.0375826031E-01	2.8359961651E-01
O	83	5.8692021619E-01	8.5375826031E-01	2.8359961651E-01
O	84	5.8692021619E-01	8.5545163318E-01	3.3599616507E-02
Hf	85	5.0000000000E-01	5.0000000000E-01	9.0654196275E-01
Hf	86	5.0000000000E-01	7.0920989349E-01	6.5654196275E-01
Hf	87	7.2386978589E-01	7.5000000000E-01	9.0654196275E-01
Hf	88	7.2386978589E-01	9.5920989349E-01	6.5654196275E-01
O	89	8.9369973390E-01	6.4193717359E-01	9.0848108456E-01
O	90	8.9369973390E-01	5.6727271991E-01	6.5848108456E-01
O	91	8.3017005199E-01	8.1727271991E-01	7.4806087819E-01
O	92	8.3017005199E-01	8.9193717359E-01	9.9806087819E-01
O	93	6.3694956969E-01	6.0545163318E-01	5.3359961651E-01
O	94	6.3694956969E-01	6.0375826031E-01	7.8359961651E-01
O	95	5.8692021619E-01	8.5375826031E-01	7.8359961651E-01
O	96	5.8692021619E-01	8.5545163318E-01	5.3359961651E-01

TABLE 6.6: Ion positions of the t-phase

Ion	index	x	y	z
Hf	1	0.0000000000E+00	0.0000000000E+00	0.0000000000E+00
Hf	2	0.0000000000E+00	2.5000000000E-01	2.5000000000E-01
Hf	3	2.5000000000E-01	2.5000000000E-01	5.0000000000E-01
Hf	4	2.5000000000E-01	5.0000000000E-01	2.5000000000E-01
O	5	3.7500000000E-01	1.2500000000E-01	3.5280306220E-01
O	6	3.7500000000E-01	1.2500000000E-01	1.0280306220E-01
O	7	3.7500000000E-01	3.7500000000E-01	1.4719693780E-01
O	8	3.7500000000E-01	3.7500000000E-01	3.9719693780E-01
O	9	1.2500000000E-01	1.2500000000E-01	1.4719693780E-01
O	10	1.2500000000E-01	1.2500000000E-01	3.9719693780E-01
O	11	1.2500000000E-01	3.7500000000E-01	3.5280306220E-01
O	12	1.2500000000E-01	3.7500000000E-01	1.0280306220E-01
Hf	13	0.0000000000E+00	0.0000000000E+00	5.0000000000E-01
Hf	14	0.0000000000E+00	2.5000000000E-01	7.5000000000E-01
Hf	15	2.5000000000E-01	2.5000000000E-01	1.0000000000E+00
Hf	16	2.5000000000E-01	5.0000000000E-01	7.5000000000E-01
O	17	3.7500000000E-01	1.2500000000E-01	8.5280306220E-01
O	18	3.7500000000E-01	1.2500000000E-01	6.0280306220E-01
O	19	3.7500000000E-01	3.7500000000E-01	6.4719693780E-01
O	20	3.7500000000E-01	3.7500000000E-01	8.9719693780E-01
O	21	1.2500000000E-01	1.2500000000E-01	6.4719693780E-01
O	22	1.2500000000E-01	1.2500000000E-01	8.9719693780E-01
O	23	1.2500000000E-01	3.7500000000E-01	8.5280306220E-01
O	24	1.2500000000E-01	3.7500000000E-01	6.0280306220E-01
Hf	25	0.0000000000E+00	5.0000000000E-01	0.0000000000E+00
Hf	26	0.0000000000E+00	7.5000000000E-01	2.5000000000E-01
Hf	27	2.5000000000E-01	7.5000000000E-01	5.0000000000E-01
Hf	28	2.5000000000E-01	1.0000000000E+00	2.5000000000E-01
O	29	3.7500000000E-01	6.2500000000E-01	3.5280306220E-01
O	30	3.7500000000E-01	6.2500000000E-01	1.0280306220E-01
O	31	3.7500000000E-01	8.7500000000E-01	1.4719693780E-01
O	32	3.7500000000E-01	8.7500000000E-01	3.9719693780E-01
O	33	1.2500000000E-01	6.2500000000E-01	1.4719693780E-01
O	34	1.2500000000E-01	6.2500000000E-01	3.9719693780E-01
O	35	1.2500000000E-01	8.7500000000E-01	3.5280306220E-01
O	36	1.2500000000E-01	8.7500000000E-01	1.0280306220E-01
Hf	37	0.0000000000E+00	5.0000000000E-01	5.0000000000E-01
Hf	38	0.0000000000E+00	7.5000000000E-01	7.5000000000E-01
Hf	39	2.5000000000E-01	7.5000000000E-01	1.0000000000E+00
Hf	40	2.5000000000E-01	1.0000000000E+00	7.5000000000E-01
O	41	3.7500000000E-01	6.2500000000E-01	8.5280306220E-01
O	42	3.7500000000E-01	6.2500000000E-01	6.0280306220E-01
O	43	3.7500000000E-01	8.7500000000E-01	6.4719693780E-01
O	44	3.7500000000E-01	8.7500000000E-01	8.9719693780E-01
O	45	1.2500000000E-01	6.2500000000E-01	6.4719693780E-01
O	46	1.2500000000E-01	6.2500000000E-01	8.9719693780E-01
O	47	1.2500000000E-01	8.7500000000E-01	8.5280306220E-01
O	48	1.2500000000E-01	8.7500000000E-01	6.0280306220E-01

Ion	index	x	y	z
Hf	49	5.000000000E-01	0.000000000E+00	0.000000000E+00
Hf	50	5.000000000E-01	2.500000000E-01	2.500000000E-01
Hf	51	7.500000000E-01	2.500000000E-01	5.000000000E-01
Hf	52	7.500000000E-01	5.000000000E-01	2.500000000E-01
O	53	8.750000000E-01	1.250000000E-01	3.5280306220E-01
O	54	8.750000000E-01	1.250000000E-01	1.0280306220E-01
O	55	8.750000000E-01	3.750000000E-01	1.4719693780E-01
O	56	8.750000000E-01	3.750000000E-01	3.9719693780E-01
O	57	6.250000000E-01	1.250000000E-01	1.4719693780E-01
O	58	6.250000000E-01	1.250000000E-01	3.9719693780E-01
O	59	6.250000000E-01	3.750000000E-01	3.5280306220E-01
O	60	6.250000000E-01	3.750000000E-01	1.0280306220E-01
Hf	61	5.000000000E-01	0.000000000E+00	5.000000000E-01
Hf	62	5.000000000E-01	2.500000000E-01	7.500000000E-01
Hf	63	7.500000000E-01	2.500000000E-01	1.000000000E+00
Hf	64	7.500000000E-01	5.000000000E-01	7.500000000E-01
O	65	8.750000000E-01	1.250000000E-01	8.5280306220E-01
O	66	8.750000000E-01	1.250000000E-01	6.0280306220E-01
O	67	8.750000000E-01	3.750000000E-01	6.4719693780E-01
O	68	8.750000000E-01	3.750000000E-01	8.9719693780E-01
O	69	6.250000000E-01	1.250000000E-01	6.4719693780E-01
O	70	6.250000000E-01	1.250000000E-01	8.9719693780E-01
O	71	6.250000000E-01	3.750000000E-01	8.5280306220E-01
O	72	6.250000000E-01	3.750000000E-01	6.0280306220E-01
Hf	73	5.000000000E-01	5.000000000E-01	0.000000000E+00
Hf	74	5.000000000E-01	7.500000000E-01	2.500000000E-01
Hf	75	7.500000000E-01	7.500000000E-01	5.000000000E-01
Hf	76	7.500000000E-01	1.000000000E+00	2.500000000E-01
O	77	8.750000000E-01	6.250000000E-01	3.5280306220E-01
O	78	8.750000000E-01	6.250000000E-01	1.0280306220E-01
O	79	8.750000000E-01	8.750000000E-01	1.4719693780E-01
O	80	8.750000000E-01	8.750000000E-01	3.9719693780E-01
O	81	6.250000000E-01	6.250000000E-01	1.4719693780E-01
O	82	6.250000000E-01	6.250000000E-01	3.9719693780E-01
O	83	6.250000000E-01	8.750000000E-01	3.5280306220E-01
O	84	6.250000000E-01	8.750000000E-01	1.0280306220E-01
Hf	85	5.000000000E-01	5.000000000E-01	5.000000000E-01
Hf	86	5.000000000E-01	7.500000000E-01	7.500000000E-01
Hf	87	7.500000000E-01	7.500000000E-01	1.000000000E+00
Hf	88	7.500000000E-01	1.000000000E+00	7.500000000E-01
O	89	8.750000000E-01	6.250000000E-01	8.5280306220E-01
O	90	8.750000000E-01	6.250000000E-01	6.0280306220E-01
O	91	8.750000000E-01	8.750000000E-01	6.4719693780E-01
O	92	8.750000000E-01	8.750000000E-01	8.9719693780E-01
O	93	6.250000000E-01	6.250000000E-01	6.4719693780E-01
O	94	6.250000000E-01	6.250000000E-01	8.9719693780E-01
O	95	6.250000000E-01	8.750000000E-01	8.5280306220E-01
O	96	6.250000000E-01	8.750000000E-01	6.0280306220E-01

TABLE 6.7: Ion positions of the c-phase

Ion	index	x	y	z
Hf	1	0.0000000000E+00	0.0000000000E+00	0.0000000000E+00
Hf	2	0.0000000000E+00	2.5000000000E-01	2.5000000000E-01
Hf	3	2.5000000000E-01	2.5000000000E-01	5.0000000000E-01
Hf	4	2.5000000000E-01	5.0000000000E-01	2.5000000000E-01
O	5	3.7500000000E-01	1.2500000000E-01	3.7500000000E-01
O	6	3.7500000000E-01	1.2500000000E-01	1.2500000000E-01
O	7	3.7500000000E-01	3.7500000000E-01	1.2500000000E-01
O	8	3.7500000000E-01	3.7500000000E-01	3.7500000000E-01
O	9	1.2500000000E-01	1.2500000000E-01	1.2500000000E-01
O	10	1.2500000000E-01	1.2500000000E-01	3.7500000000E-01
O	11	1.2500000000E-01	3.7500000000E-01	3.7500000000E-01
O	12	1.2500000000E-01	3.7500000000E-01	1.2500000000E-01
Hf	13	0.0000000000E+00	0.0000000000E+00	5.0000000000E-01
Hf	14	0.0000000000E+00	2.5000000000E-01	7.5000000000E-01
Hf	15	2.5000000000E-01	2.5000000000E-01	1.0000000000E+00
Hf	16	2.5000000000E-01	5.0000000000E-01	7.5000000000E-01
O	17	3.7500000000E-01	1.2500000000E-01	8.7500000000E-01
O	18	3.7500000000E-01	1.2500000000E-01	6.2500000000E-01
O	19	3.7500000000E-01	3.7500000000E-01	6.2500000000E-01
O	20	3.7500000000E-01	3.7500000000E-01	8.7500000000E-01
O	21	1.2500000000E-01	1.2500000000E-01	6.2500000000E-01
O	22	1.2500000000E-01	1.2500000000E-01	8.7500000000E-01
O	23	1.2500000000E-01	3.7500000000E-01	8.7500000000E-01
O	24	1.2500000000E-01	3.7500000000E-01	6.2500000000E-01
Hf	25	0.0000000000E+00	5.0000000000E-01	0.0000000000E+00
Hf	26	0.0000000000E+00	7.5000000000E-01	2.5000000000E-01
Hf	27	2.5000000000E-01	7.5000000000E-01	5.0000000000E-01
Hf	28	2.5000000000E-01	1.0000000000E+00	2.5000000000E-01
O	29	3.7500000000E-01	6.2500000000E-01	3.7500000000E-01
O	30	3.7500000000E-01	6.2500000000E-01	1.2500000000E-01
O	31	3.7500000000E-01	8.7500000000E-01	1.2500000000E-01
O	32	3.7500000000E-01	8.7500000000E-01	3.7500000000E-01
O	33	1.2500000000E-01	6.2500000000E-01	1.2500000000E-01
O	34	1.2500000000E-01	6.2500000000E-01	3.7500000000E-01
O	35	1.2500000000E-01	8.7500000000E-01	3.7500000000E-01
O	36	1.2500000000E-01	8.7500000000E-01	1.2500000000E-01
Hf	37	0.0000000000E+00	5.0000000000E-01	5.0000000000E-01
Hf	38	0.0000000000E+00	7.5000000000E-01	7.5000000000E-01
Hf	39	2.5000000000E-01	7.5000000000E-01	1.0000000000E+00
Hf	40	2.5000000000E-01	1.0000000000E+00	7.5000000000E-01
O	41	3.7500000000E-01	6.2500000000E-01	8.7500000000E-01
O	42	3.7500000000E-01	6.2500000000E-01	6.2500000000E-01
O	43	3.7500000000E-01	8.7500000000E-01	6.2500000000E-01
O	44	3.7500000000E-01	8.7500000000E-01	8.7500000000E-01
O	45	1.2500000000E-01	6.2500000000E-01	6.2500000000E-01
O	46	1.2500000000E-01	6.2500000000E-01	8.7500000000E-01
O	47	1.2500000000E-01	8.7500000000E-01	8.7500000000E-01
O	48	1.2500000000E-01	8.7500000000E-01	6.2500000000E-01

Ion	index	x	y	z
Hf	49	5.000000000E-01	0.000000000E+00	0.000000000E+00
Hf	50	5.000000000E-01	2.500000000E-01	2.500000000E-01
Hf	51	7.500000000E-01	2.500000000E-01	5.000000000E-01
Hf	52	7.500000000E-01	5.000000000E-01	2.500000000E-01
O	53	8.750000000E-01	1.250000000E-01	3.750000000E-01
O	54	8.750000000E-01	1.250000000E-01	1.250000000E-01
O	55	8.750000000E-01	3.750000000E-01	1.250000000E-01
O	56	8.750000000E-01	3.750000000E-01	3.750000000E-01
O	57	6.250000000E-01	1.250000000E-01	1.250000000E-01
O	58	6.250000000E-01	1.250000000E-01	3.750000000E-01
O	59	6.250000000E-01	3.750000000E-01	3.750000000E-01
O	60	6.250000000E-01	3.750000000E-01	1.250000000E-01
Hf	61	5.000000000E-01	0.000000000E+00	5.000000000E-01
Hf	62	5.000000000E-01	2.500000000E-01	7.500000000E-01
Hf	63	7.500000000E-01	2.500000000E-01	1.000000000E+00
Hf	64	7.500000000E-01	5.000000000E-01	7.500000000E-01
O	65	8.750000000E-01	1.250000000E-01	8.750000000E-01
O	66	8.750000000E-01	1.250000000E-01	6.250000000E-01
O	67	8.750000000E-01	3.750000000E-01	6.250000000E-01
O	68	8.750000000E-01	3.750000000E-01	8.750000000E-01
O	69	6.250000000E-01	1.250000000E-01	6.250000000E-01
O	70	6.250000000E-01	1.250000000E-01	8.750000000E-01
O	71	6.250000000E-01	3.750000000E-01	8.750000000E-01
O	72	6.250000000E-01	3.750000000E-01	6.250000000E-01
Hf	73	5.000000000E-01	5.000000000E-01	0.000000000E+00
Hf	74	5.000000000E-01	7.500000000E-01	2.500000000E-01
Hf	75	7.500000000E-01	7.500000000E-01	5.000000000E-01
Hf	76	7.500000000E-01	1.000000000E+00	2.500000000E-01
O	77	8.750000000E-01	6.250000000E-01	3.750000000E-01
O	78	8.750000000E-01	6.250000000E-01	1.250000000E-01
O	79	8.750000000E-01	8.750000000E-01	1.250000000E-01
O	80	8.750000000E-01	8.750000000E-01	3.750000000E-01
O	81	6.250000000E-01	6.250000000E-01	1.250000000E-01
O	82	6.250000000E-01	6.250000000E-01	3.750000000E-01
O	83	6.250000000E-01	8.750000000E-01	3.750000000E-01
O	84	6.250000000E-01	8.750000000E-01	1.250000000E-01
Hf	85	5.000000000E-01	5.000000000E-01	5.000000000E-01
Hf	86	5.000000000E-01	7.500000000E-01	7.500000000E-01
Hf	87	7.500000000E-01	7.500000000E-01	1.000000000E+00
Hf	88	7.500000000E-01	1.000000000E+00	7.500000000E-01
O	89	8.750000000E-01	6.250000000E-01	8.750000000E-01
O	90	8.750000000E-01	6.250000000E-01	6.250000000E-01
O	91	8.750000000E-01	8.750000000E-01	6.250000000E-01
O	92	8.750000000E-01	8.750000000E-01	8.750000000E-01
O	93	6.250000000E-01	6.250000000E-01	6.250000000E-01
O	94	6.250000000E-01	6.250000000E-01	8.750000000E-01
O	95	6.250000000E-01	8.750000000E-01	8.750000000E-01
O	96	6.250000000E-01	8.750000000E-01	6.250000000E-01

Defect position

This section displays the positions of defects of the more complicated defect types. These are the $(2M_{\text{Hf}})V_{\text{O}}$, O_{I} , Al_{I} , $(2Al_{\text{I}})V_{\text{Hf}}$, and $(2Al_{\text{I}})V_{\text{Hf}}V_{\text{O}}$ defects. The defects were build in the standardized 96-atomic supercells from above. Substitutional defects and vacancies will be indicated by atom index, interstitial defects by coordinates. Tables 6.8 and 6.9 show the defect positions of 6.25 f.u.% and 12.5 f.u.% $(2M_{\text{Hf}})V_{\text{O}}$ defects.

TABLE 6.8: Atom index of dopants M and oxygen vacancy O of the 6.25 f.u.% $(2M_{\text{Hf}})V_{\text{O}}$ defect.

		ab	ac	ba	bc	ca	cb
m-phase	M1	25	13	25	13	13	13
	M2	49	49	49	25	49	25
	O1	9	22	53	9	9	36
o-phase	M1	25	13	25	13	13	13
	M2	61	61	61	25	61	25
	O1	9	22	54	9	9	36
f-phase	M1	25	13	25	13	13	13
	M2	49	49	49	25	49	25
	O1	9	22	54	9	9	36
f'-phase	M1	25	13	25	13	13	13
	M2	49	49	49	25	49	25
	O1	9	35	22	9	9	54
t-phase	M1	25	13	25	13	13	13
	M2	49	49	49	25	49	25
	O1	9	22	54	9	9	36
c-phase	M1	25					
	M2	49					
	O1	9					

TABLE 6.9: Atom index of dopants M and oxygen vacancies O of the 12.5 f.u.% $(2M_{\text{Hf}})V_{\text{O}}$ defect.

		ab	ac	ba	bc	ca	cb
m-phase	M1	13	25	13	4	13	13
	M2	14	38	25	25	25	27
	M3	49	49	52	49	51	49
	M4	50	62	88	76	87	87
	O1	54	65	79	36	54	47
	O2	69	94	90	81	77	96
o-phase	M1	13	25	13	4	13	13
	M2	14	38	25	25	25	27
	M3	49	49	52	49	51	49
	M4	50	62	88	76	87	87
	O1	54	65	79	36	54	47
	O2	69	94	90	81	77	96
f-phase	M1	13	25	13	4	13	13
	M2	10	38	25	25	25	27
	M3	49	49	52	49	51	49
	M4	50	62	88	76	87	87
	O1	54	65	79	36	54	47
	O2	69	94	90	81	77	96
f'-phase	M1	13	4	3	25	13	2
	M2	16	25	13	27	14	13
	M3	49	49	25	49	25	49
	M4	52	76	39	51	26	62
	O1	54	59	34	35	22	18
	O2	69	80	48	81	45	65
t-phase	M1	13	25	13	4	13	13
	M2	14	38	25	25	25	27
	M3	49	49	52	49	51	49
	M4	50	62	88	76	87	87
	O1	54	65	79	36	54	47
	O2	69	94	90	81	77	96
c-phase	M1	13					
	M2	14					
	M3	49					
	M4	50					
	O1	54					
	O2	69					

Table 6.10 shows the coordinates of interstitial O and Al in 96 atomic supercells. A 96 atomic cell contained one interstitial oxygen at one of the 5 sets of coordinates listed below.

TABLE 6.10: Coordinates of interstitial O and Al in 96 atomic supercells

x	y	z
2.5000000000E-01	2.5000000000E-01	7.5000000000E-01
5.0000000000E-01	2.5000000000E-01	5.0000000000E-01
2.5000000000E-01	0.0000000000E+00	1.0000000000E+00
0.0000000000E+00	2.5000000000E-01	1.0000000000E+00
0.0000000000E+00	0.0000000000E+00	7.5000000000E-01

Table 6.11 shows the coordinates of interstitial Al-atoms as well as the index of the Hf-vacancy in 96 atomic supercells.

TABLE 6.11: Coordinates of interstitial Al Atoms and atom index of Hf vacancy of the $(2Al_I)V_{Hf}$ and $(2Al_I)V_{Hf}V_O$ defects in 96 atomic supercells

Phase	V_{Hf} Index	Atom	x	y	z
m-phase	85	Al1	5.0000000000E-01	5.0000000000E-01	3.5000000000E-01
		Al2	5.0000000000E-01	5.0000000000E-01	6.5000000000E-01
o-phase	73	Al1	5.0000000000E-01	5.0000000000E-01	3.5654196275E-01
		Al2	5.0000000000E-01	5.0000000000E-01	6.5000000000E-01
f-phase	85	Al1	5.0000000000E-01	5.0000000000E-01	3.5000000000E-01
		Al2	5.0000000000E-01	5.0000000000E-01	6.5000000000E-01
t-phase	85	Al1	5.0000000000E-01	5.0000000000E-01	3.5000000000E-01
		Al2	5.0000000000E-01	5.0000000000E-01	6.5000000000E-01
c-phase	85	Al1	5.0000000000E-01	5.0000000000E-01	3.5000000000E-01
		Al2	5.0000000000E-01	5.0000000000E-01	6.5000000000E-01

Table 6.12 shows the index of possible oxygen vacancies of $(2Al_I)V_{Hf}V_O$ defects in 96 atomic supercells.

TABLE 6.12: Atom index of O vacancy of the $(2Al_I)V_{Hf}V_O$ defects in 96 atomic supercells

Phase	Vacancy										
m-phase	V_O	8	19	29	42	59	72	82	93		
o-phase	V_O	8	19	29	30	42	59	72	82	93	94
f-phase	V_O	8	19	29	30	42	59	72	82	93	
t-phase	V_O	8	19	29	42	59	72	82	93		
c-phase	V_O	8	19	29	42	59	72	82	93		

Appendix B

ABINIT input file

Example of a standard ABINIT input file:

```
##          Definition of cell          ##
acell      9.6850024E+00 9.7856534E+00 1.0000214E+01 Bohr # lattice constants
rprim     9.9640280446E-01 0.0000000000E+0 8.4743443735E-02 # lattice vector
          0.0000000000E+0 1.0000000000E+0 0.0000000000E+0
          8.4307631643E-02 0.0000000000E+0 9.9643977402E-01

##          Definition of atoms        ##
ntypat    2 # Number of species
znuc1     8.00000 72.00000 # Atomic number of atoms
natom     12 # Number of atoms

xred      0.0000000000E+0 0.0000000000E+0 0.0000000000E+0 # Hf
          0.0000000000E+0 4.1670724509E-01 5.0000000000E-01 # Hf
          4.4741397988E-01 5.0000000000E-01 9.1590884070E-01 # Hf
          4.4741397988E-01 9.1670724509E-01 4.1590884070E-01 # Hf
          7.9167831615E-01 2.8898042249E-01 8.6098185607E-01 # O
          7.9167831615E-01 1.2772682260E-01 3.6098185607E-01 # O
          6.5573566373E-01 7.8898042249E-01 5.4926984636E-02 # O
          6.5573566373E-01 6.2772682260E-01 5.5492698463E-01 # O
          2.7392988043E-01 2.1537216896E-01 1.8787334142E-01 # O
          2.7392988043E-01 2.0133507613E-01 6.8787334142E-01 # O
          1.7348409945E-01 7.1537216896E-01 7.2803549928E-01 # O
          1.7348409945E-01 7.0133507613E-01 2.2803549928E-01 # O

typat     2 2 2 2 1 1 1 1 1 1 1 1 # type of atom

##          Definition of k-points    ##
kptrlatt  4 0 0 # k-point grid
          0 4 0
          0 0 4

shiftk    0 0 0 # shift of the k-point grid
```



```

##          Definition of the basis set          ##
ecut       18.0                                # Maximal kinetic energy cut-off. in Hartree
pawecutdg  22                                  # PAW energy cutoff for the double grid

##          Exchange-correlation functional      ##
#ixc       7                                  # LDA Perdew-Wang 92 functional

##          Optimization of lattice             ##
ionmov     2                                  # optimization method of atom positions
optcell    2                                  # optimize cell
tolmxf     1e-5                               # max gradient on ion or stress in cell optimization
strfact    100                                # stopping criterion for cell optimization
iscf       17                                  # Self-consistent calculation, using algorithm 7
ntime      500                                # Max. number of ion/cell optimization steps
ecutsm     0.5                                # needed for variable cell
dilatmx    1.05                               # needed for variable cell

##          definition of the SCF procedure      ##
toldff     1.0d-6                             # SCF stopping criterion
nstep      150                                # Maximal number of SCF cycles
diemac     5.0                                # Dielectric constant for preconditioning
charge     0                                  # Electric charge

##          Spin and Smearing                   ##
nband      50                                  # Number of Bands
#occopt    3                                  # Smearing Algorithm
#tsmear    0.04                               # Strength of Smearing
#nspol     2                                  # Number of Spin Polarization
#nspden    2                                  # Number of Spin Density Components

##          parallelisation parameters          ##
#max_ncpus 1600                               # Display parallelisation options
autoparal  1                                  # Automatic parallelisation
paral_kgb  1                                  # k-Point parallelisation options
npband     10                                  # Number of Processors at the BAND level
npfft      3                                  # Number of Processors at the FFT level
#nspinor   2                                  # Number of Processors at the SPINOR level
npkpt      18                                  # Number of Processors at the k-Point level

##          Restart Option                      ##
restartxf   -2                                # Restart from lowest Etot

```

FHI-AIMS input file

Example of a standard FHI-AIMS control file. Definition of atom species excluded.

```
##                               Physical model settings  ##
xc                               pw-lda                 # LDA Perdew-Wang 92 functional
charge                           0                     # Charge
spin                              none                 # Spin
override_illconditioning         true
relativistic                     atomic_zora scalar   relativistic option

##                               SCF convergence settings ##

occupation_type                  gaussian 0.1
mixer                             pulay             # mixing option
n_max_pulay                      10               # mixing iterations
charge_mix_param                 0.2              # mixing parameter
sc_accuracy_rho                  1E-5             # SCF stopping criterion
sc_accuracy_eev                  1E-3             # SCF stopping criterion
sc_accuracy_etot                 1E-6             # SCF stopping criterion
sc_iter_limit                    100                # SCF number of iterations
k_grid                           2 2 2             # k-point grid

##                               For relaxation:         ##

relax_geometry                   bfgs 1e-3        # relaxation method
relax_unit_cell                  full              # relaxation option
sc_accuracy_forces               1e-4             # relaxation stopping criterion
```

Appendix C

Total Energy

TABLE 6.13: Total energy U_0 in meV of II-valent doped HfO₂ as well as values for oxygen defects.

	Concentration	m-phase	o-phase	f-phase	f'-phase	t-phase	c-phase
HfO ₂		0.00	26.62	52.38		113.95	167.01
V _O	3.125	0.00	27.67	46.83		106.21	161.64
	6.250	0.00	29.18	41.51		100.91	156.84
O _I	3.125	0.00	25.63	45.71	124.10	186.46	245.24
	6.250	0.00	159.94	53.16	269.76	260.64	462.87
Be _{Hf}	3.125	0.00	22.11	52.38	102.89	121.01	176.45
	6.250	0.00	22.17	19.44	211.68	77.10	389.01
Be _{Hf} V _O	3.125	0.00	20.11	52.93	91.52	75.19	251.61
	6.250	0.00	50.72	69.65	70.87	37.86	404.35
Mg _{Hf}	3.125	0.00	22.19	50.17	103.91	116.84	
	6.250	0.00	21.26	46.43	232.15	118.20	
Mg _{Hf} V _O	3.125	0.00	22.00	52.76	99.25	95.38	215.43
	6.250	0.00	49.50	89.97	102.82	94.49	300.67
Ca _{Hf}	3.125	0.00	22.28	46.68	95.58	106.80	
	6.250	0.00	20.81	37.70	222.51	121.66	
Ca _{Hf} V _O	3.125	0.00	19.59	46.14		84.90	219.21
	6.250	0.00	46.03	66.35		76.08	306.91
Sr _{Hf}	3.125	0.00	22.36	41.92	87.59	103.49	174.24
	6.250	0.00	22.39	30.95	191.33	102.16	285.49
Sr _{Hf} V _O	3.125	0.00	17.96	38.75		78.97	237.86
	6.250	0.00	45.51	37.34		42.55	342.52
Ba _{Hf}	3.125	0.00	2.47	38.18		116.16	
	6.250	0.00	2.55	49.49		145.58	
Ba _{Hf} V _O	3.125	0.00	18.22	35.83		80.00	288.30
	6.250	0.00	44.81	38.91		50.02	426.58

TABLE 6.14: Total energy U_0 in meV of III-valent doped HfO₂.

	Concentration	m-phase	o-phase	f-phase	f'-phase	t-phase	c-phase
HfO ₂		0.00	26.62	52.38	108.51	113.95	167.01
La _{Hf}	3.125	0.00	24.24	40.56	88.27	106.46	153.06
	6.250	0.00	25.00	33.50	78.57	97.79	157.15
	12.500	0.00	24.15	7.82	34.01	98.64	165.31
La _{Hf} V _O	3.125	0.00	22.34	36.43	97.70	95.38	122.45
	6.250	0.00	20.84	19.11	101.61	53.84	41.16
	12.500	0.00	-1.77	14.55	97.25	-4.61	81.28
(2La _{Hf})V _O	6.25	0.00	33.38	20.27		-2.39	
	12.50	0.00	29.66	-51.40		-49.73	
Y _{Hf}	3.125	0.00	24.32	47.79	98.90	106.97	150.60
	6.250	0.00	23.13	40.48	84.19	97.96	98.13
	12.500	0.00	22.79	26.19	59.18	86.06	123.81
Y _{Hf} V _O	3.125	0.00	24.32	44.51	97.96	96.24	
	6.250	0.00	22.41	34.04	89.10	74.87	
	12.500	0.00	21.65	16.68	29.81	5.68	
(2Y _{Hf})V _O	6.25	0.00	25.19	39.18		42.36	
	12.50	0.00	13.46	-32.91		-43.86	
Al _{Hf}	3.125	0.00	25.09	52.72		100.68	187.42
	6.250	0.00	24.15	42.86		71.77	211.74
	12.500	0.00	23.47	57.14		22.11	286.74
Al _{Hf} V _O	3.125	0.00	22.00	43.65	85.33	91.00	104.92
	6.250	0.00	14.59	31.96	59.40	62.70	62.70
	12.500	0.00	5.32	5.32	29.81	18.81	26.26
(2Al _{Hf})V _O	6.25	0.00	17.10	48.89		47.69	
	12.50	0.00	41.08	24.06		79.90	
Al _O	3.125	0.00	24.49	77.98		192.01	195.16
	6.250	0.00	13.61	80.61		263.44	498.65

Elastic tensor

TABLE 6.15: Elastic tensor in units of 100 GPa for HfO₂ and ZrO₂ in Voigt notation

HfO ₂						
m-phase	3.9496212	1.9738073	1.0921881	0.0038013	-0.4811520	-0.0050849
	1.9735797	4.9666597	1.7987688	0.0000643	0.1114399	0.0006053
	1.0919579	1.7987671	3.1405313	0.0071311	-0.1838027	-0.0063968
	0.0037715	0.0001507	0.0072409	1.2049098	0.0000376	0.1431602
	-0.4843915	0.1114407	-0.1870465	0.0000555	1.0966237	-0.0009260
	-0.0047120	0.0009781	-0.0065071	0.1415483	-0.0009741	1.6507540
f-phase	4.5587450	1.8918986	1.4928062	0.0000005	-0.0000227	-0.0002349
	1.8918096	4.8107014	1.5018142	0.0000012	-0.0000201	-0.0000670
	1.4928134	1.5019096	4.4467483	0.0000159	-0.0000230	-0.0012535
	0.0000005	0.0000028	0.0000156	1.1722913	0.0004713	-0.0000002
	-0.0000233	-0.0000191	-0.0000213	0.0004618	1.1045384	-0.0000020
	-0.0005826	-0.0002736	-0.0011870	-0.0000002	-0.0000020	1.6044061
t-phase	5.8067336	0.8877091	1.5210818	0.0000067	0.0000263	-0.0000087
	0.8877505	4.0767711	0.8876900	0.0000089	0.0000801	0.0000528
	1.5210795	0.8876460	5.8066775	-0.0000175	0.0000263	0.0000247
	0.0000019	0.0000049	0.0000019	0.5449754	-0.0000029	-0.0000044
	0.0000277	0.0000681	0.0000277	-0.0000029	0.9665828	-0.0000012
	0.0000189	0.0000464	0.0000189	-0.0000044	-0.0000012	0.5451889
ZrO ₂						
m-phase	3.6200055	1.8642033	1.0304722	0.0010025	-0.4748195	-0.0035980
	1.8641307	4.5701095	1.6307573	0.0011410	0.0602918	0.0024331
	1.0303027	1.6306577	2.8393802	0.0022359	-0.2030878	-0.0074054
	0.0009653	0.0012634	0.0023491	1.0841019	0.0001327	0.1354723
	-0.4750946	0.0602884	-0.2033570	0.0001356	0.9626815	-0.0010821
	-0.0032327	0.0028644	-0.0074565	0.1353349	-0.0011291	1.4920203
f-phase	4.2539218	1.7960583	1.4489391	-0.0004768	-0.0007888	-0.0036344
	1.7959370	4.4042365	1.4170873	-0.0002496	-0.0000777	-0.0044524
	1.4488531	1.4171248	4.0615346	-0.0011160	-0.0001379	-0.0043510
	-0.0004709	-0.0003003	-0.0011335	1.0604660	-0.0006838	-0.0007338
	-0.0007590	-0.0001022	-0.0002174	-0.0006814	0.9832363	0.0003212
	-0.0038637	-0.0045037	-0.0043074	-0.0007513	0.0003288	1.4303588
t-phase	5.3329043	0.8493628	1.4463094	-0.0000047	0.0008280	-0.0000057
	0.8491985	3.8419300	0.8492553	-0.0000307	0.0008262	-0.0000054
	1.4463093	0.8494257	5.3330156	-0.0000128	0.0008280	0.0000088
	-0.0000120	-0.0000282	-0.0000120	0.5788266	-0.0000026	0.0006270
	0.0008588	0.0008519	0.0008588	-0.0000026	0.9177416	-0.0000023
	-0.0000055	-0.0000128	-0.0000055	0.0006270	-0.0000023	0.5787983

Appendix D

List of Symbols

A	Area
A_i	Area
a	lattice constant
a_{MP}	Parameter of Makov-Payne correction
b	lattice constant
C	Constant
C_t	surface energy of interlayer
$C_{lm}^{\alpha\beta}$	inter-atomic force constant matrix
$\tilde{C}_{lm}^{\alpha\beta}$	Fourier transform of inter-atomic force constant matrix
c	lattice constant
c_2	2nd order term for Landau-Devonshire model
c_4	4th order term for Landau-Devonshire model
c_6	6th order term for Landau-Devonshire model
c_{MP}	Parameter of Makov-Payne correction
D_i	dielectric displacement
d_G	grain thickness
\tilde{d}_G	grain bulk thickness
d_{ikl}	piezoelectric coefficient
E	Energy
\mathbf{E}_c	coercive Field
E_{Corr}	Energy correction of Formation energy
E_f	Formation energy
E_i	electric Field
E_j	electric Field
E_k	electric Field
E_{MP}	Makov-Payne
e	electron charge
e_{ikl}	piezoelectric coefficient
F	Helmholtz Energy
F_i	Force vector
\vec{F}	Force vector

f_n	function
$f_{\alpha,\beta}$	grain size distribution function
G	Gibbs Energy
g	Gibbs Energy density
g_S	scale function
g_{ikl}	piezoelectric coefficient
H	Enthalpy
\hat{H}	Hamilton operator
h_{ikl}	piezoelectric coefficient
K_{ijkl}	elastic tensor
k	relative permittivity
k_{ik}	relative permittivity tensor
\vec{k}	wave vector
k_B	Boltzmann constant
L	Size of supercell in Makov-Payne correction
M	atomic mass
M_I	atomic mass
M_l	atomic mass
M_m	atomic mass
m_e	electron mass
m_i	number of defects
N	number of atoms
N_G	number of formula units in a grain
n	number of electrons
P	electric Polarisation
P_i	Polarisation vector
\mathbf{P}_r	remanent Polarisation
p	pressure
p_i	pyro coefficient
Q	heat
q	electric Charge
\vec{q}	phonon wave vector
\vec{R}	atom coordinates
R_i	atom coordinates
R_l	atom coordinates
R_m	atom coordinates
\vec{r}	electron coordinates

r_c	cutoff radius
r_G	grain radius
\tilde{r}_G	grain bulk radius
S	Entropy
s	weight factor for linear combination
s_n	weight factor for linear combination
T	Temperature
\hat{T}	kinetic energy operator
T_c	Curie Temperature
T_p	Phase transition Temperature
U	internal energy
U_0	total Energy
u_i	single electron eigenvalue
u_{i0}	single electron ground state eigenvalue
V	Volume
\hat{V}	Potential
V_{12}	Volume of 12 atomic cell
\hat{V}_c	correlation Potential
\hat{V}_{Ha}	Hartree Potential
\hat{V}_x	exchange Potential
\hat{V}_{xc}	exchange correlation Potential
ΔV	Band structure alignment
W	work
X	Defect type
x	Stoichiometry
Y	spherical harmonics
Y_{lm}	spherical harmonics
Z	nuclei charge
β	lattice angle
Γ	incomplete Gamma function
Γ_I	interface energy
Γ_S	surface energy
γ	specific surface energy
$\tilde{\gamma}$	specific interface energy
δ	interlayer thickness
δ_{ik}	Kronecker delta
ϵ	permittivity

ϵ_{ik}	permittivity tensor
ϵ_0	electric field constant
ϵ_F	Fermi energy
ϵ_{VB}	valence band edge
μ	chemical potential
μ_i	chemical potential
ρ_e	charge density
ρ_m	mass density
σ_{kl}	stress tensor
τ_{kl}	strain tensor
τ_{ij}	strain tensor
Φ	Phase
Φ	atomic Wavefunction
ϕ	single electron Wavefunction
ϕ_i	single electron Wavefunction
ϕ_{i0}	ground state eigenfunction
ϕ_n	single electron Wavefunction
χ	susceptibility
χ_{ik}	susceptibility tensor
$\chi_{ik(ionic)}$	ionic susceptibility tensor
$\chi_{ik(electronic)}$	electronic susceptibility tensor
χ_{jk}	susceptibility tensor
Ψ	Wavefunction
ψ	electronic Wavefunction
Ω	Number of micro states
ω	frequency

List of Figures

2.1	Example for separation of charge barycenters under mechanical stress. (a) relaxed solid, the charge barycenters overlap, no polarization. (b) strained solid with separation of charge barycenters resulting in a polarization	6
2.2	(a) Hysteresis loop of a ferroelectric. The Landau-Devonshire model predicts vertical edges, but experiments often produce sloped edges (sketched here). (b) double-well potential for the two polarization states of a ferroelectric without an external electric field, (c) double-well potential for the two polarization states of a ferroelectric with an external electric field favoring one polarization state.	7
2.3	(a)-(e) Landau-Devonshire model of a first order phase transition from paraelectric to ferroelectric in the various temperature ranges (explanation see text). (f) Resulting polarization as a function of temperature.	8
2.4	(a)-(c) Landau-Devonshire model of a second order phase transition from paraelectric to ferroelectric in the various temperature ranges (explanation see text). (d) Resulting polarization as a function of temperature.	10
2.5	Euler diagram depicting the structural relationship between dielectrics, piezoelectrics, pyroelectrics, and ferroelectrics.	10
2.6	The two polarization states of ferroelectric lead zirconate titanate.	11
2.7	(a) Hysteresis curve of field induced ferroelectricity. (b)-(e) Landau-Devonshire model of field induced ferroelectricity for various electric fields (explanation see text). The temperature is held constant.	12
2.8	The six polymorphs of the $\text{Hf}_{1-x}\text{Zr}_x\text{O}_2$ system. Depicted are (a) the monoclinic phase, (b) the orthorhombic phase, (c) the tetragonal phase, (d) the ferroelectric phase, (e) the second ferroelectric phase, and (f) the cubic phase. Blue ions are Hf or Zr ions, red are oxygen ions. The golden ions in (d) and (e) are oxygen ions, that are visibly displaced from centrosymmetric positions and therefore the cause of the polarization of the two ferroelectric phases . . .	13
2.9	The two polarization states of ferroelectric HfO_2	15
3.1	(a) M_{Hf} , (b) $\text{M}_{\text{Hf}}\text{V}_{\text{O}}$ and (c) $(2\text{M}_{\text{Hf}})\text{V}_{\text{O}}$ defects. Blue: Hf, red: O, green: dopant M, white: vacancy	31
3.2	(a) Al_{I} , (b) $(2\text{Al}_{\text{I}})\text{V}_{\text{Hf}}$ and (c) $(2\text{Al}_{\text{I}})\text{V}_{\text{Hf}}\text{V}_{\text{O}}$ defects. Blue: Hf, red: O, green: dopant M, white: vacancy	33

4.1	Model of a grain with grain radius r_G and grain thickness d_G . The grain thickness is assumed to be equal to the film thickness.	39
4.2	(a) Model of a single grain. (b) Model of multiple grains with a tetragonal interface layer, where the bulk phase is determined by the surface to volume ratio of the interface and the interface energy	41
5.1	The convergence of the total energy difference $ \Delta U_0 $ between the m- and f-phase as an absolute value. The most precise calculation serves as the reference point for the total energy. (a) depicts the total energy dependency from the energy cutoff, (b) from the k-point grid, and (c) from the PAW energy cutoff.	44
5.2	The convergence of the lattice constants $ \Delta a $, $ \Delta b $, $ \Delta c $, and $ \Delta V $ for f-phase as an absolute value. The most precise calculation serves as the reference point. (a) depicts the lattice constant dependency from the energy cutoff, (b) from the k-point grid, and (c) from the PAW energy cutoff.	45
5.3	Helmholtz free energy as a function of temperature for (a) HfO ₂ and (b) ZrO ₂ . Phase is marked by line color, pseudopotential library by line type. Results obtained with the PAW atomic data sets from the GBRV library are plotted with a continuous line, results obtained with the SM-pseudo potentials in dashed line. Results obtained with the all electron code FHI-AIMS are represented by a dash-dotted line.	53
5.4	Enthalpy as a function of applied uni-axial stress. (a) HfO ₂ , (b) Hf _{0.5} Zr _{0.5} O ₂ , and (c) ZrO ₂ . Phase is marked by line color, stress direction by line type.	56
5.5	Enthalpy as a function of applied uni-axial stress. (a)-(c) HfO ₂ , (d)-(f) Hf _{0.5} Zr _{0.5} O ₂ , and (g)-(i) ZrO ₂ . Phase is marked by line color, stress direction by line type. The spatial orientation of polymorphs relative to each other is fixed, the various phases compete with each other based on the E-module in a given crystallographic direction.	59
5.6	Enthalpy as a function of lattice constants. (a)-(c) HfO ₂ , (d)-(f) Hf _{0.5} Zr _{0.5} O ₂ , and (g)-(i) ZrO ₂ . Phase is marked by line color, strain direction by line type. The spatial orientation of polymorphs relative to each other is fixed, the various phases compete with each other based on the E-module in a given crystallographic direction.	61
5.7	Enthalpy as a function of applied bi-axial stress. (a) HfO ₂ , (b) Hf _{0.5} Zr _{0.5} O ₂ , and (c) ZrO ₂ . Phase is marked by line color, stress direction by line type.	62

5.8	Enthalpy as a function of applied bi-axial stress. (a)-(c) HfO ₂ , (d)-(f) Hf _{0.5} Zr _{0.5} O ₂ , and (g)-(i) ZrO ₂ . Phase is marked by line color, stress plane by line type. The spatial orientation of polymorphs relative to each other is fixed, the various phases compete with each other based on the sensitivity of the enthalpy to an external stress in a given crystallographic plane.	63
5.9	Enthalpy as a function of lattice plane area. (a)-(c) HfO ₂ , (d)-(f) Hf _{0.5} Zr _{0.5} O ₂ , and (g)-(i) ZrO ₂ . Phase is marked by line color, strain plane by line type. The spatial orientation of polymorphs relative to each other is fixed, the various phases compete with each other based on the sensitivity of the enthalpy to strain in a given crystallographic plane.	65
5.10	Enthalpy as a function of hydrostatic stress for (a) HfO ₂ , (b) Hf _{0.5} Zr _{0.5} O ₂ , and (c) ZrO ₂ . Enthalpy as a function of cell volume for (d) HfO ₂ , (e) Hf _{0.5} Zr _{0.5} O ₂ , and (f) ZrO ₂ . Phase is marked by line color.	66
5.11	Two possible mechanisms of stabilization of the ferroelectric phase in the Hf _{1-x} Zr _x O ₂ system. (a) and (b) depicts the stabilization by stress with the associated energies depicted in (a1) and (b1). The strain effect is depicted in (c)-(f) with the associated energies in (d1), (e1) and (f1).	68
5.12	Grain size distribution of (a) 7 nm and (b) 10 nm HfO ₂ films, with the corresponding phase diagram below in (c) and (d).	70
5.13	Grain size distribution of (a) 20 nm and (b) 40 nm Hf _{1-x} Zr _x O ₂ films, with the corresponding phase diagram below in (c) and (d).	72
5.14	Effect of oxygen vacancies (a) and interstitials (b) on the total energy difference ΔU_0 of the various HfO ₂ polymorphs compared to the m-phase. Subplot (c) shows the formation energy of those defects as a function of the oxygen chemical potential with the light color representing oxygen-rich and the dark color oxygen-poor conditions.	74
5.15	Effect of Sr-doping on the total energy difference ΔU_0 of the various HfO ₂ polymorphs compared to the m-phase. The defects are (a) Sr _{Hf} and (b) Sr _{Hf} V _O . Subplot (c) shows the formation energy of those defects as a function of the oxygen chemical potential with the light color representing oxygen-rich and the dark color oxygen-poor conditions. The dopant concentration range for which ferroelectricity was experimentally observed (ALD and CSD) is highlighted in grey.	75

5.16	Effect of Be-doping on the total energy difference ΔU_0 of the various HfO ₂ polymorphs compared to the m-phase. The defects are (a) Be _{Hf} and (b) Be _{Hf} V _O . Subplot (c) shows the formation energy of those defects as a function of the oxygen chemical potential with the light color representing oxygen-rich and the dark color oxygen-poor conditions.	77
5.17	Effect of Mg-doping on the total energy difference ΔU_0 of the various HfO ₂ polymorphs compared to the m-phase. The defects are (a) Mg _{Hf} and (b) Mg _{Hf} V _O . Subplot (c) shows the formation energy of those defects as a function of the oxygen chemical potential with the light color representing oxygen-rich and the dark color oxygen-poor conditions. The dopant concentration range for which ferroelectricity was experimentally observed (ALD and CSD) is highlighted in grey.	78
5.18	Effect of Ca-doping on the total energy difference ΔU_0 of the various HfO ₂ polymorphs compared to the m-phase. The defects are (a) Ca _{Hf} and (b) Ca _{Hf} V _O . Subplot (c) shows the formation energy of those defects as a function of the oxygen chemical potential with the light color representing oxygen-rich and the dark color oxygen-poor conditions.	79
5.19	Effect of Ba-doping on the total energy difference ΔU_0 of the various HfO ₂ polymorphs compared to the m-phase. The defects are (a) Ba _{Hf} and (b) Ba _{Hf} V _O . Subplot (c) shows the formation energy of those defects as a function of the oxygen chemical potential with the light color representing oxygen-rich and the dark color oxygen-poor conditions. The dopant concentration range for which ferroelectricity was experimentally observed (ALD and CSD) is highlighted in grey.	81
5.20	Effect of Al-doping on the total energy difference ΔU_0 of the various HfO ₂ polymorphs compared to the m-phase. The defects are (a) Al _{Hf} , (b) Al _{Hf} V _O , and (c) (2Al _{Hf})V _O . Subplot (d) shows the formation energy of those defects as a function of the oxygen chemical potential with the light color representing oxygen-rich and the dark color oxygen-poor conditions. The O-symbols represent ABINIT results, X-symbols those of FHI-AIMS. The dopant concentration range for which ferroelectricity was experimentally observed (ALD and CSD) is highlighted in grey.	82

5.21	(a) Effect of Al _O -doping on the total energy difference ΔU_0 of the various HfO ₂ polymorphs compared to the m-phase. (b) Total energies for one- and two-atomic defects interstitial defects in 96-atomic supercells. Therefore, the doping concentration differs for the different defects. (c) shows the formation energy of those defects as a function of the oxygen chemical potential with the light color representing oxygen-rich and the dark color oxygen-poor conditions. The dopant concentration range for which ferroelectricity was experimentally observed (ALD and CSD) is highlighted in grey.	83
5.22	Effect of Y-doping on the total energy difference ΔU_0 of the various HfO ₂ polymorphs compared to the m-phase. The defects are (a) Y _{Hf} , (b) Y _{Hf} V _O , and (c) (2Y _{Hf})V _O . Subplot (d) shows the formation energy of those defects as a function of the oxygen chemical potential with the light color representing oxygen-rich and the dark color oxygen-poor conditions. The O-symbols represent ABINIT results, X-symbols those of FHI-AIMS. The dopant concentration range for which ferroelectricity was experimentally observed (ALD and CSD) is highlighted in grey.	84
5.23	Effect of La-doping on the total energy difference ΔU_0 of the various HfO ₂ polymorphs compared to the m-phase. The defects are (a) La _{Hf} , (b) La _{Hf} V _O , and (c) (2La _{Hf})V _O . Subplot (d) shows the formation energy of those defects as a function of the oxygen chemical potential with the light color representing oxygen-rich and the dark color oxygen-poor conditions. The O-symbols represent ABINIT results, X-symbols those of FHI-AIMS. The dopant concentration range for which ferroelectricity was experimentally observed (ALD and CSD) is highlighted in grey.	86

List of Tables

5.1	Simulation and experimental results of the 6 HfO ₂ polymorphs. Values for cell volume and mass density are calculated from lattice constants if not provided in the original research. Lattice constants are for 12 atomic cells.	47
5.2	Simulation and experimental results of the 6 Hf _{0.5} Zr _{0.5} O ₂ polymorphs. Values for cell volume and mass density are calculated from lattice constants if not provided in the original research. Lattice constants are for 12 atomic cells. . .	49
5.3	Simulation and experimental results of the 6 ZrO ₂ polymorphs. Values for cell volume and mass density are calculated from lattice constants if not provided in the original research. Lattice constants are for 12 atomic cells.	51
5.4	Dielectric tensor elements and average dielectric constants for HfO ₂ and ZrO ₂ calculated with LDA DFPT with the GBRV library. The depicted values are the sum of the electronic dielectric tensor and the ion dielectric tensor.	54
5.5	Piezoelectric tensor elements e_{ikl} in C/m ² for HfO ₂ and ZrO ₂ calculated with LDA-DFPT with the GBRV library as well as experimental values of common piezo materials for comparison	54
5.6	Elastic main tensor elements (in Voigt notation) K_{ijkl} in GPa for HfO ₂ and ZrO ₂ calculated with LDA-DFPT with the GBRV library	54
5.7	Ferroelectric vector \mathbf{P}_r in $\mu\text{C}/\text{cm}^2$ for HfO ₂ , Hf _{0.5} Zr _{0.5} O ₂ , and ZrO ₂ calculated with Berry-Phase with the SM-PP	55

Abbreviations

Abbreviation	Explanation
1T	one transistor
1T-1C	one transistor one capacitor
ALD	atomic layer deposition
ani	anion
at	atom
BST	barium strontium titanate ($\text{Ba}_x\text{Sr}_{1-x}\text{TiO}_3$)
BTO	barium titanate (BaTiO_3)
c-phase	cubic phase
cat	cation
CMOS	complementary metal-oxide-semiconductor
CSD	chemical solution deposition
DFPT	density functional perturbation theory
DFT	density functional theory
DRAM	dynamic random access memory
Exp	experimental
f-phase	ferroelectric phase
f.u.	formula unit
FeFET	ferroelectric field effect transistor
FeRAM	ferroelectric random access memory
FET	field effect transistor
FTC	ferroelectric tunnel junctions
GGA	generalized gradient approximation
HAADF-STEM	high-angle annular dark-field scanning transmission electron microscopy
hcp	hexagonal close-packed
HZO	hafnium zirconium oxide
LAPW	linearized augmented plane wave
LDA	local density approximation
LOBPCG	locally optimal block preconditioned conjugate gradient
m-phase	monoclinic phase
o-phase	orthorhombic phase
f'-phase	polar phase
PAW	projector augmented wave
PBE	Perdew-Burke-Ernzerhof
PCM	phase change memory
PLD	pulsed laser deposition
PP	pseudopotential
PVD	physical vapor deposition
PW	Perdew-Wang
PZ	Perdew-Zunger-Ceperley-Alder
PZT	lead zirconate titanate ($\text{PbZr}_x\text{Ti}_{1-x}\text{O}_3$)
RAM	random access memory
ReRAM	restive random access memory
SCF	self-consistent-field
SEM	scanning electron microscopy
SM-PP	self made pseudopotential
STO	strontium titanate (SrTiO_3)
t-phase	tetragonal phase
XRD	X-ray diffraction

6.1 Curriculum Vitae



Personal Data

Name: Robin Materlik
Date of birth: 31.10.1987
Place of birth: Augsburg
Nationality: German
E-mail address: robin:Materlik@gmx.de

Academic Career

Dissertation

June 2013 - present

TU Dresden

Investigation of ferroelectric binary oxides of hafnium and zirconium by first principles

Master studies

March 2011 - May 2013

Munich University of Applied Sciences

Micro- and Nanotechnology (M.Sc.)

Bachelor studies

October 2006 - May 2011

Munich University of Applied Sciences

Engineering Physics (B.Sc.)

List of Scientific Publications

Journal Articles as First Author

1. R. Materlik, C. Künneth, and A. Kersch, "The origin of ferroelectricity in $\text{Hf}_{1-x}\text{Zr}_x\text{O}_2$: A computational investigation and a surface energy model," *Journal of Applied Physics* 117, 134109 (2015).
2. R. Materlik, C. Künneth, T. Mikolajick, and A. Kersch, "The impact of charge compensated and uncompensated strontium defects on the stabilization of the ferroelectric phase in HfO_2 ," *APL*, (2017).
3. R. Materlik, C. Künneth, M. Falkowski, T. Mikolajick, and A. Kersch. Al-, Y-, and La-doping effects favoring intrinsic and field induced ferroelectricity in HfO_2 : A first principles study. *Journal of Applied Physics*, 123(16):164101, 2018.

Journal Articles as Co-Author

1. M. Hoffmann, U. Schröder, T. Schenk, T. Shimizu, H. Funakubo, O. Sakata, D. Pohl, M. Drescher, C. Adelman, R. Materlik, A. Kersch, and T. Mikolajick, "Stabilizing the ferroelectric phase in doped hafnium oxide," *Journal of Applied Physics* 118, 072006 (2015).
2. C. Künneth, R. Materlik, and A. Kersch, "Modeling ferroelectric film properties and size effects from tetragonal interlayer in $\text{Hf}_{1-x}\text{Zr}_x\text{O}_2$ grains," *Journal of Applied Physics* 121, 205304 (2017).
3. C. Künneth, R. Materlik, M. Falkowski, and A. Kersch. Impact of Four-Valent Doping on the Crystallographic Phase Formation for Ferroelectric HfO_2 from First-Principles: Implications for Ferroelectric Memory and Energy-Related Applications. *ACS Applied Nano Materials*, 1(1):254–264, 2018.
4. M. Falkowski, C. Künneth, R. Materlik, and A. Kersch. Unexpectedly large energy variations from dopant interactions in ferroelectric HfO_2 from high-throughput ab initio calculations. *npj Computational Materials*, (1):2057–3960, 2018.

Articles in Conference Proceedings as Co-Author

1. T. Schenk, S. Müller, U. Schröder, R. Materlik, A. Kersch, M. Popovici, C. Adelman, S. V. Elshocht, and T. Mikolajick, “Strontium doped hafnium oxide thin films: Wide process window for ferroelectric memories,” in 2013 Proceedings of the European Solid-State Device Research Conference (ESSDERC)(2013) pp. 260–263.

Conference Talks

1. R. Materlik, C. Künneth, T. Schenk, C. Richter, S. Starschich, U. Böttger, U. Schröder, T. Mikolajick and A. Kersch, Grain Size Effect in Ferroelectric Hafnium Oxide, Joint IEEE International Symposium on the Applications of Ferroelectrics, European Conference on Applications of Polar Dielectrics & Workshop on Piezoresponse Force Microscopy (ISAF/ECAPD/PFM), Darmstadt, 2016.